Asymmetric Supercapacitors Based on Transition Metal Oxides Induced Pseudocapacitance

Mak Wai Fatt

School of Materials Science & Engineering

A Thesis Submitted to Nanyang Technological University
in partial Fulfillment of the Requirement for the Degree of
Doctor of Philosophy

2012

Acknowledgement

I wish to express my sincere gratitude and heartfelt thanks to my supervisor, A/P Madhavi Srinivasan for her esteemed guidance, continual support and encouragement. Without her constructive comments, great patience and motivation, this dissertation would not be possible. She has certainly been an excellent mentor, providing me with much needed ideas and directions for my work. I am very grateful to have such a fulfilling and enriching experience working under her.

I also sincerely express my gratitude to co-supervisor, Professor Subodh Gautam Mhaisalkar for his support, patience, motivation, and allowing me the room to venture in my own way. He has widened my research experience through supporting me for overseas attachments during my course of study. Without his continual support and motivation, this work would not be possible.

During the course of this work, I have been granted opportunity to work with an excellent research team under Prof. George Gruner in UCLA. Working with them was a memorable experience, and I am grateful for their insightful comments and fruitful discussion which improved the clarity of my research. I would also like to mention my two mentors Dr Martti Kaempgen and Dr Andreas Kiebele. I sincerely thank them for their fruitful suggestions and exchanging of ideas.

I would also like to thank my fellow team mates: Dr Yogesh Sharma, Dr Sudeshna, Grace Wee, Cheah Yan Ling, Teh Pei Fen, Sutanto, Ting Ji, Han Wee, Yah

Wen, Dr Nutan, and Dr Prasanth. I am thankful for their assistance advices provided in this work.

Finally I wish to thank my beloved parents, especially my mother for her loving support, understanding and forbearance. For this, I am truly blessed and most grateful.

Abstract

Pseudocapacitor exhibiting higher capacitance and energy density than electrochemical double layer capacitor (EDLC) and delivering greater power density than batteries represent unique charge storage devices that bridge the gap of EDLC and rechargeable battery. In particular, RuO_2 based material has received much attention in past decades. However, they are expensive due to their scarce resources. This study reports on alternative pseudocapacitive material such as iron oxide as an electrode material for supercapacitor (SCs) applications. Also, an asymmetrical device configuration was conceptualized to extend the working voltage so as to achieve higher energy density.

The role of nanofibers in electrical double layer formation, pseudocapacitive properties, charge retention and cycling performance has been investigated for various materials. Physical characterization techniques such as Field Emission Scanning Electron Microscopy, X-ray Diffraction, Nitrogen Adsorption Isotherm, and Fourier Transform Infra Red Spectroscopy were used to study the physical properties of various materials. Electrochemical characterization such as cyclic voltammetry, galvanostatic charge-discharge, and electrochemical impedance spectroscopy were employed to investigate the electrochemical performance of different materials. These studies provide insight into the effect of morphology, surface area, electrode-electrolyte interaction on charge storage and transport mechanisms in SCs. In addition, the effect of material

porosity l on capacitance contribution was investigated. Higher content of micropores is found to increase the capacitance as more ions can be accommodated in these micropores.

Systematic study on the effect of electrolytes on supercapacitor performance was carried out, including correlation with the size of cations and comparison between aqueous and organic electrolytes and the morphological effect of the electrode material. The size of the ions also plays a substantial part in electrical double layer contribution. With smaller size, higher quantity of charges can be stored and subsequently utilized.

Reversible chemical reactions are also found to have overwhelming contribution to the charge storage via pseudocapacitance. Solvated sodium ions have additional pseudocapacitance which greatly contributes to the charge storage capability. Choice of electrode/electrolyte pair is therefore critical to for obtaining higher charge storage/ capacitance in supercapacitors.

An asymmetrical device configuration was conceptualized to extend the working voltage so as to achieve higher energy density. Tto realize asymmetrical supercapacitor, different electrodes of nanofibers have been judiciously coupled. The effect of asymmetrical supercapacitor architecture on the voltage window has been investigated. The performance of the devices was then evaluated using Ragone plot. Our studies has shown that such asymmetrical supercapacitors proposed increases the energy density of supercapacitors and would better bridge the gap of EDLC and rechargeable batteries.

Table of Contents

Table of Contents

List of Tables

List of Figures

Chapter 1 Introduction

1.1 Energy Storage Systems

Escalating oil prices has generated a growing global concern over the state of world energy consumption and supply. There is increased interest in further developing technology utilizing electrical devices as sources of energy supply, especially in the area of transportation. Alternative renewable energy sources is being heavily researched, especially the field of photovoltaic and fuel cell technology. Hybrid Electric Vehicles (HEV) and Fuel Cell Vehicles (FCV) are available for consumer from various manufacturers, albeit at a significant higher cost than the conventional Internal Combustion Engine (ICE). These HEVs and FCVs use a combination of technologies to cater to the energy requirement. The hybridization is attained with the integration of fuel cells, rechargeable batteries, and supercapacitors. The system design needs to ensure maximum energy output with minimal fuel consumption.

People still expect to drive around at times when the sun does not shine (rainy days and nights). Thus energy storage systems (ESS) play a crucial pole in practical implementation of renewable clean energy in our daily lives. Batteries and electrochemical capacitors are at the forefront among electric ESS. However, the performance of present ESS needs to be improved to meet higher energy and power demand of future applications ranging from portable electronic to HEVs, FCVs and large industrial equipments.

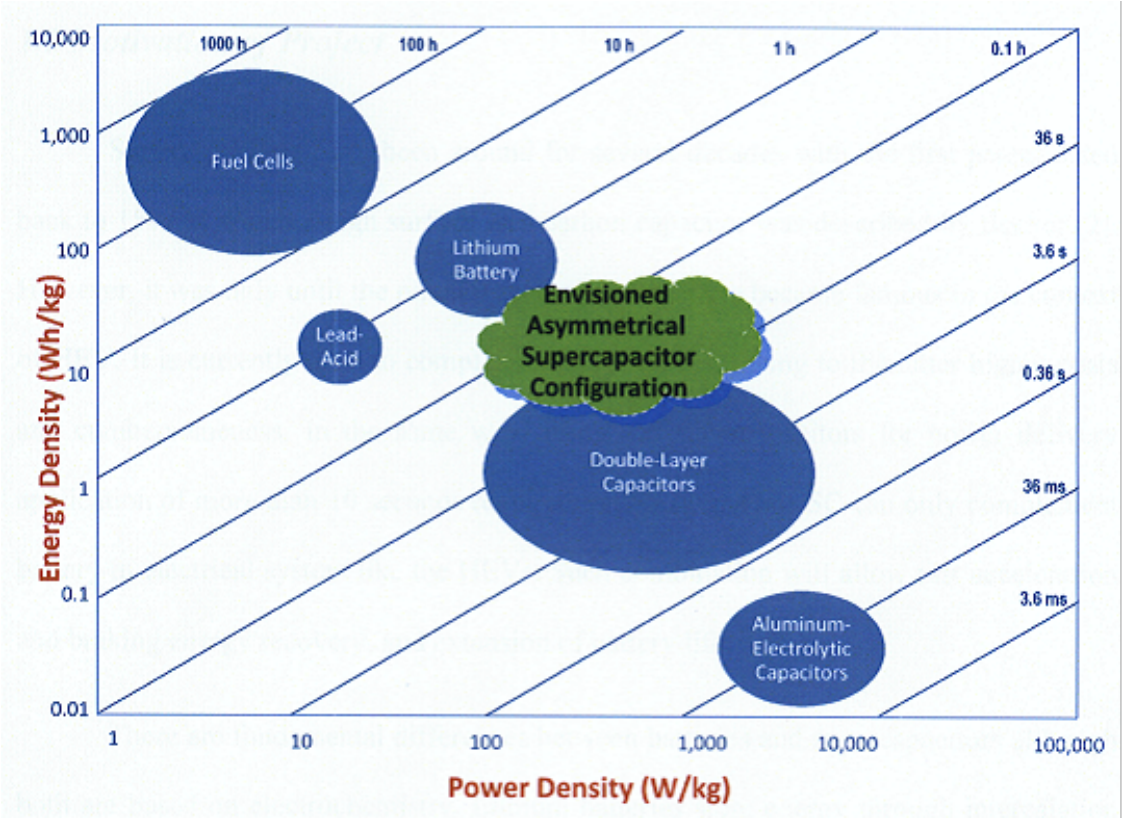

Figure 1.1: Ragone plot of various electrical storage systems depicting the power and energy densities. For comparison sake, the envisioned asymmetric supercapacitor performance studied in this work is also inserted.

Pseudocapacitor, being a sub-class of supercapacitor represents a rising class of energy storage device capable of bridging the gap between rechargeable batteries and capacitors. Besides, pseudocapacitor possesses higher energy density and thus can be used to complement or replace batteries in some energy storage applications, such as for load leveling and uninterruptible power supplies.

1.2 Motivation of Project

Supercapacitors have been around for several decades with the first patent dated back to 1597 in which a high surface area carbon capacitor was described by Becker [2]. However, it was only until the nineties that supercapacitors became famous in the context of HEV. It is currently used to complement the batteries, owing to the latter higher costs and cumbersomeness. In the same way, using the supercapacitors for power delivery application of more than 10 seconds required over-sizing. Thus SC can only complement battery in electrical system like the HEVs. Such combination will allow fast acceleration and braking energy recovery, and extension of battery life.

There are fundamental differences between batteries and supercapacitors although both are based on electrochemistry. Lithium batteries store energy through intercalation of Li ion, whereas SC store energy in the form of electrical field. Others include cycle life, power density, energy density etc as discussed in literature [3, 4].

Supercapacitors plays important role in complementing batteries in Energy and Storage System ESS such as Uninterruptible Power Supply (UPS), load leveling and emergency doors (16 per plane) on Airbus 380. The 2007 report of US department of Energy assigns equal importance to SC and batteries for future ESS [5]. The capability of important ESS can be depicted in Ragone plot shown in Figure 1.1. These devices must be used in their respective time constant domains. Using Li ion battery for high power application will degrade cycle life drastically.

The key to high power supercapacitors lies in using a high specific surface area (SSA) blocking and electronically conducting electrode. High SSA carbon satisfies the requirement for this application. Templated, activated carbon and carbide derived carbons [6], fiber, nanotubes [7] have been investigated for EDLC applications. However, their low energy density often limits their wide application.

Another type of supercapacitors called pseudo capacitor having a higher capacitance utilizes fast, reversible redox reactions at the surface of active materials to achieve greater energy storage. Transitional metal oxides such as RuO_2, MnO_2, NiO, Co_3O_4 [8] as well as conducting polymer [9] have been extensively researched as a potential electrode candidate in last decade. These pseudocapacitors have exhibited higher capacitance than that of carbon based EDLC.

Currently, two different approaches are being explored to increase the energy density of supercapacitors. One is the combination of pseudo capacitive metal oxide with a capacitive carbon electrode. The other is the combination of Li-ion intercalation electrodes with a capacitive carbon electrode. Although both can attain greater energy storage, they suffer from low cycle life due to the degradation of the faradic and lithium intercalating electrode. Thus the selection of electrode pair (balance positive and negative electrodes' capacities) is crucial so as to avoid transforming a high performance supercapacitors into a mediocre battery.

Transition metal oxide (TMO) capacitor has shown high capacitance, however, they also suffer from low electronic conductivity. Often, TMO are co-precipitated or

electrodeposited onto a metal substrate. However, the complexity and time involved undermine the possibility of up-scaling the fabrication process, thus limit their real life applications. Currently, effort is lacking in addressing this issue. In order to fill this technology gap, this research will focus on the incorporating TMO nanostructure with electrically conducting material.

In addition, fundamental gaps are still present in understanding atomic and molecular level process that governs pseudocapacitor operation, limitation and failure. Fundamental research is required to uncover the underlying principles that govern the complex process. With a better understanding of the interrelated process, new devices can then be fabricated to address current ESS technology gap and fulfilling future energy storage requirements.

1.3 Research Objectives and Scope

1. Development of electrically conducting pseudo capacitive composites:
   - Integrating binder, conductivity enhancer and active material in a single component.
2. Study of parameters that affect device performance
   - Varying the content of active nanomaterial.
   - Studying the effect of electrolytes.
   - Investigating the viability of asymmetrical configuration.
3. Investigations of nanomaterial contribution towards device performance
   - Research on charge storing mechanism of device through cyclicvoltametry and galvanostatic charge-discharge curve.
   - Investigate internal resistance of device through electrochemical impedance spectroscopy.
   - Correlate charging/discharging mechanism with morphology, electrode materials.

Chapter 2 Literature Review

2.1 Overview of Electrochemical Capacitor

Electrochemical capacitors also known as supercapacitor, are generally classified into electrochemical double layer capacitors (EDLCs) and pseudocapacitors based on their charge storage mechanism. The first invention was reported in 1957 when Becker [2] filed a patent describing a concept of an electrochemical capacitor utilizing high surface area carbon coated on current collector immersed in sulphuric acid. In 1969, researchers at Standard Oil of Ohio (SOHIO) accidentally rediscovered it while working on experimental fuel cell designs, created a prototype of modern version of electrochemical capacitor. Their cell design which is basically made up of two layers of activated carbon separated by a thin porous insulator still remains as the basis of today's EDLCs. However, SOHIO did not commercialized their invention, only licensed it to Nippon Electrical Company (NEC), which subsequently initiated the commercialization of the first electrochemical capacitor in 1978. Nevertheless, its energy density still remained low for commercial applications until mid 1990s with the up rise of nanomaterial. Various advances in material science together with refinement of existing systems have drastically improved the performance of EDLC with an equally rapid reduction in cost. Subsequently, EDLC was integrated into commercial plane (Airbus 380) to power emergency evacuation slides in 2005. Nonetheless, the energy density still remains low for application in most electronic gadgets.

In this chapter, the working principle and architecture of capacitor are reviewed. Current theoretical models are briefly reviewed. The various classes of electrode materials including carbon, electrically conducting polymers and transitional metal oxides based are discussed. Their application as electrode material for supercapacitor is reported. Their advantages and limitation are also examined.

2.2 Fundamentals and Applications of Electrochemical Capacitor

2.2.1 Types of Electrochemical Capacitor

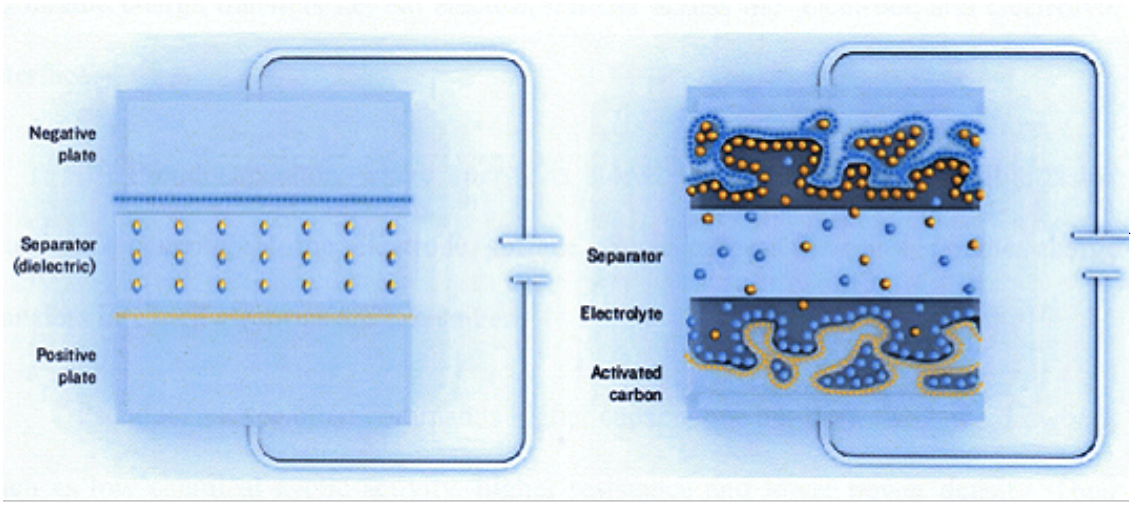

Figure 2.1: (Left) conventional capacitor, (right) electrical double layer capacitor (a type of supercapacitor) [1]

As aforementioned, supercapacitor is a charge storage device which can be classified into two categories depending on the charge storage mechanism. As shown in Figure 2.1, a supercapacitor consists of two electrodes, a separator that electrically insulates the two electrodes, and an electrolyte. It differs from the conventional capacitor as charges are electrically stored on the electrode/electrolyte interface. This greatly reduced the distance between the charges, and hence tremendously enhances the capacitance of the electrode according to equation 2.1 which will be discussed in following section.

In general, supercapacitor can store their charges via two types of mechanisms:

(a) Electrical double layer capacitor, where energy is stored in the double layer formed under external potential source. The process is purely electrostatic which involves no faradic charge transfers i.e. No electron transfer across the electrode and electrolyte interface.

(b) Pseudocapacitor, where energy is stored through the fast reversible redox reactions occurring at the electrode surface. Such process involves faradic charge transfers in which electrons are exchanged.

Pseudocapacitor often commands higher capacitance but they also have drawback such as low chemical cyclic activity, higher resistance and lower power density. Their capacitance can be viewed as the superposition of non-faradic double layer capacitance (C_{dl}) and faradic pseudocapacitance (C_{pc}). The first element (C_{dl}) is determined by the total accessible surface area while the latter (C_{pc}) is regulated by facile reversible redox reactions.

2.2.1.1 Electrical Double Layer Capacitor (EDLC)

When an electronically conducting electrode is placed in an ionic conducting electrolyte, layer of charges are accumulated on both sides of the solid/electrolyte interface. This parallel layer of charges is termed as double layer. There is no charge transfer occurring across the double layer, and such electrodes are generally referred to as ideally polarizable electrode (non-faradic)[10].

The fundamental concept of EDLCs revolves around 2 ideally polarizable electrodes immersed in an electrolyte. It utilizes double layer capacitance that arises at the electrodes and electrolyte interfaces. A schematic of the electric double layer is shown in Fig 2.1. Charging up the electrode results in double layer formation and the energy is stored in the electrical field instituted by these double layers on both electrodes. Since no electrochemical reaction is involved, the reversibility and cycle life of EDLC is much better than in rechargeable batteries.

2.2.1.1.1 Theoretical Models of Double Layer

2.2.1.1.1.1 Helmholtz Double Layer

Double layer was first coined by Helmholtz in 1887.[11] He proposed a model with two layers of charges; one resides on the metal surface, and the counter charge in solution at the solid/electrolyte interface. These two sheets of charges of opposite polarity are separated by a distance of molecular order. Figure 2.1 illustrates the Helmholtz model. The capacitance of electrical double layer is given by equation 2.1.

$$C = \frac{\varepsilon_0 \varepsilon A}{d} \qquad (2.1)$$

Where ε_0 is the permittivity of free space having a constant value (8.854×10^{-12} J^{-1} m^{-1}), ε_r is the dielectric constant of electrolyte, A the surface area of electrode, and d distance between the parallel plates of charges.

This model predicts that the capacitance is independence of applied voltage and concentration of electrolyte. Thus, it fails to explain the variation of capacitance with potential and concentration of electrolyte at low electrolyte concentration (<0.1 mol dm^{-3}). Nonetheless, the Helmholtz model seems to be appropriate for polarizable electrodes in sufficiently high concentration of electrolyte (>1 mol dm^{-3}).

2.2.1.1.1.2 Gouy-Chapman Model

Between 1910-1913, Gouy and Chapman proposed a diffuse double layer model which take into account the dependency of capacitance on both potential and electrolyte concentration.[11] They suggested that the random thermal motion will prevent the counter ions from accumulating on the surface of electrode. In this model, the ions are viewed as point charges contained within the diffuse layer. Taking into account both Poisson and Boltzmann equations, the capacitance can be given by equation 2.2 [11]:

$$C = \left(\frac{2\varepsilon\varepsilon_0 z^2 e^2 c_0}{kT} \right)^{\frac{1}{2}} \cosh \frac{ze\varphi_m}{2kT} \qquad (2.2)$$

Where z is the magnitude of ionic charge, c_0 is the concentration of ions in bulk solution, k is the Boltzmann constant, T is the absolute temperature, and φ_m is the potential at the metal surface.

The Gouy-Chapman model has addressed the drawback of Helmholtz model, recognizing the dependence of capacitance on both the potential and concentration. However, this model is only valid for very dilute solutions (<0.001 mol dm^{-3}) and at potential close to point of zero charge.[11] Nevertheless, the model has contributed to a better understanding of the double layer, and find it uses in understanding the stability of colloids.

2.2.1.1.1.3 Stern Model

Stern subsequently combined these two aforementioned models (Helmholtz and Gouy-Chapman) in 1924, and proposed that some ions are adhered to the electrode, while some are scattered in the diffuse layer due to thermal disarray.[11] This model take into account the fact that ions have a finite size, and consequently do not come closer to the electrode than the order of ionic radius. It also assumed two region of charge separation. One part of solution charges is immobilized in the compact layer, and the rest is dispersed in the diffuse layer as shown in Figure 2.2.

In this model, the double layer is effectively made up of two capacitances in series, C_H due to the Helmholtz layer and C_G due to the diffuse layer. The total capacitance is therefore given by equation 2.3,

$$\frac{1}{C_{dl}} = \frac{1}{C_H} + \frac{1}{C_G} \qquad (2.3)$$

In very dilute solution and close to the point of zero charge, C_G becomes very small according to equation 2.3; with C_H remains constant, overall capacitance can be approximated to C_G. Correspondingly, overall capacitance can be approximated to C_H in concentrated solutions. However, Stern model inapplicable in certain solutions where ions (e.g. Cl^-, I^-, Br^-) come close or being adsorbed onto the electrode.

2.2.1.1.1.4 Grahame Model

In 1947, Grahame proposed that some ionic or neutral species can be adsorbed onto the electrode although the closest approach to the electrode is occupied by solvent molecules.[11] This could come from de-solvated ions or ions which do not possess salvation shell. Such ions which adsorbed to the electrode are termed specifically adsorbed ions.[11] Grahame suggested the existence of three regions, namely, inner Helmholtz plane (IHP), outer Helmholtz plane (OHP) and diffuse layer as shown in Figure 2.3.

2.2.1.1.1.5 Bockris, Devananthan and Muller Model

In 1963, Bockris, Devananthan and Muller proposed a model that considered the interaction of polar solvent molecules with electrode.[11] They suggested that there would be interaction between electrode and dipole of water molecules in dipole solvent, such as water. Since solvent molecules exist in overwhelming quantity, there would be a layer of solvent molecules adhered to the surface of electrode. The dipole of these solvent

molecules would have a fixed orientation due to charge interaction with electrode. Occasionally, some solvent molecules would be displaced by specifically adsorbed ions. There will also be subsequent layers with orientation intermediate of the first layer and that in the bulk solution as shown in Figure 2.3.

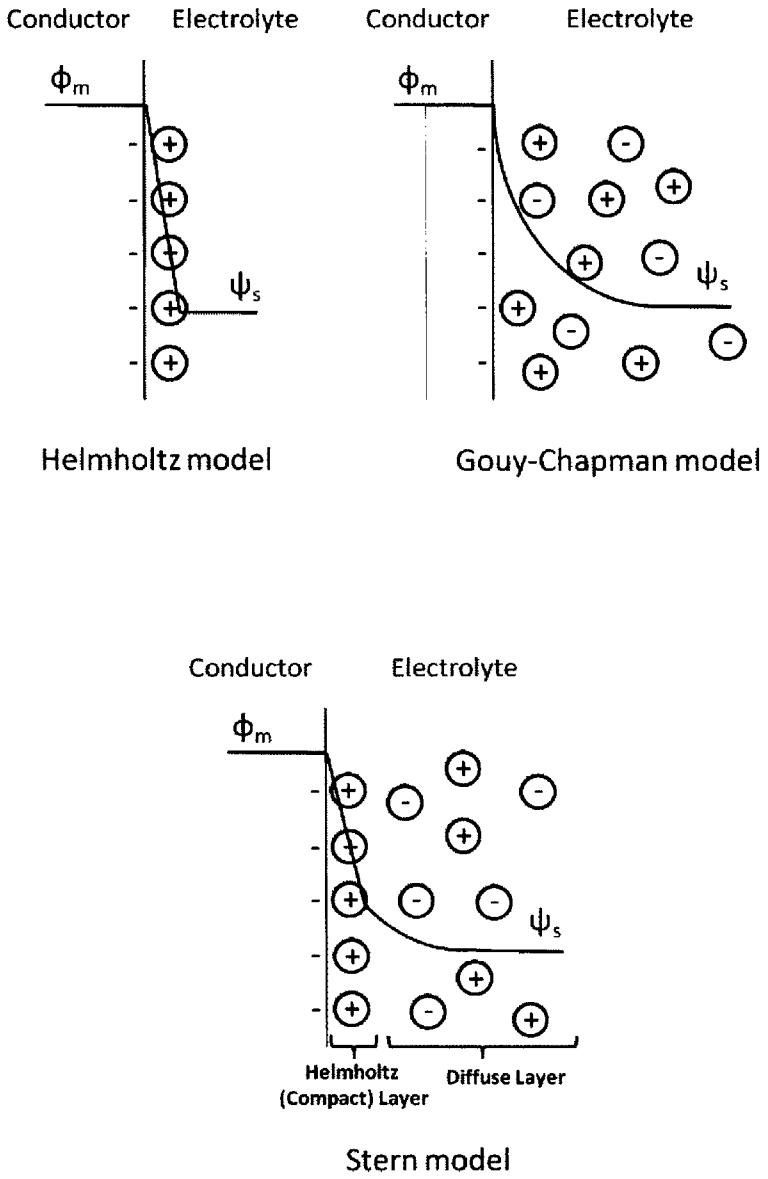

Figure 2.2: Schematic depicting the Helmholtz model, Guoy-Chapman model and Stern model.

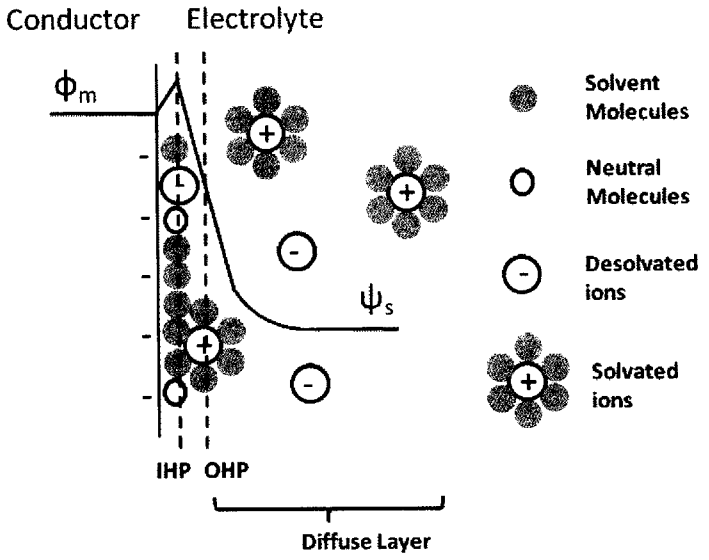

Grahame model

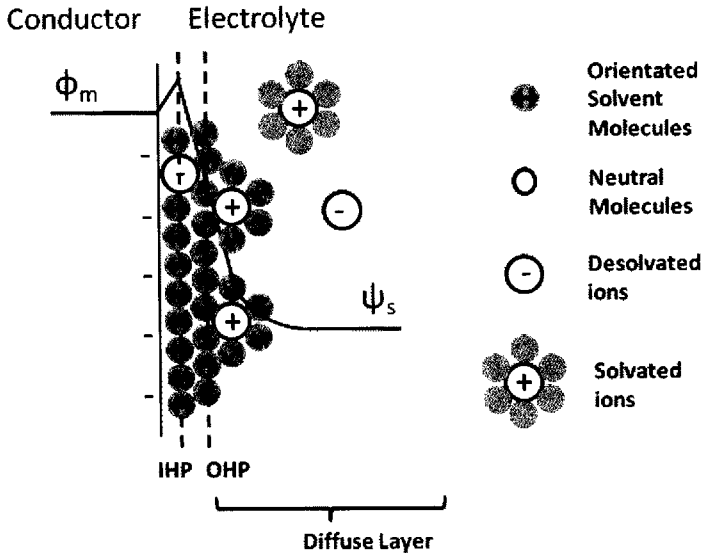

Bockris, Devanathan & Muller model

Figure 2.3: Schematic depicting the Grahame model and Bockris, Devanathan and Muller models

2.2.2 Pseudocapacitor

A different kind of capacitance called pseudocapacitance arises on electrodes when application of external potential induces faradic current. This is fundamentally different from the EDLC due to the way the charge is stored. In principal, pseudocapacitance can increase the effective capacitance of electrochemical capacitor by as much as two orders over that of EDLC. [12] Such pseudocapacitance is derived from reactions such as electro-sorption of atoms, electrochemical doping-dedoping, electrochemical redox charge transfers, and intercalation. [13, 14] Electrosorption occurs when ions such as H^+ are reversibly adhered to the surface of electrode such as platinum. Doping-dedoping process takes place in electronically conducting polymers like polyaniline, poly(3,4-ethylenedioxythiophene), polypyrrole, polythiophene etc. Redox charge transfers take places when electro-active species donates (or receives) electrons and gets oxidized (or reduced). Materials undergoing such redox reactions generally include transitional metal oxides such as RuO_2, MnO_2, V_2O_5, SnO_2, Fe_3O_4, Co_3O_4 and etc. Formally, lithium intercalation exhibits a pseudocapacitance though lithium ion systems are generally referred as battery devices also known as lithium ion battery. [13]

2.2.2.1 Pseudocapacitor Mechanism

2.2.2.1.1 Electronically Conducting Polymers

Electronically conducting polymer such as polyaniline, polypyrrole and polythiophene derivatives also exhibit pseudocapacitance. They are rendered conductive through the conjugated π bond system along polymer backbone. Such polymers are attractive as they have good electrical conductivity from a few S cm^{-1} to 500 S cm^{-1} in the doped state, [15] coupled with their relatively fast charge-discharge kinetics and rapid doping-dedoping process. [16] Energy can be stored and retrieved as the delocalized π electrons are accepted and released through electrochemical doping-dedoping process. Conducting polymers can be p-doped with anions when oxidized and n-doped when reduced. The general representations for the charging-discharging process are as follows:

$$C_p \leftrightarrows C_p^{n+} (A^-)_n + ne^- \quad \text{(forward, p-doping)}$$

$$C_p + ne^- \leftrightarrows C_p^{n-} (C^+)_n \quad \text{(forward, n-doping)}$$

Where C_p represents the electronically conducting polymer, A is the anions, and C is the cations. The forward reaction represents the charging process, and vice versa.

Supercapacitor based solely on electronically conducting polymers can be subdivided into three categories, [17-21] namely, Type I, II and III as follow:

Type I: Having the same p-dopable or n-dopable polymer for both electrodes. (Symmetrical)

Type II: Having two different of either p-dopable or n-dopable polymer with different range of electro-activity. (Asymmetrical)

Type III: Having the same polymer for both electrodes with the p-doped form working as the positive electrode, and the n-doped form working as the negative electrode. (Symmetrical)

Thus far, Type III supercapacitor has been the most attractive. In this configuration, the charge is released at higher potential (up to 3V) as compared with both type I and II. [9] This higher operating voltage translates into both higher power and energy density. Supercapacitor based on electronically conducting polymers generally exhibit high capacitance value ranging from 90 to 530 F g^{-1}. [22] However, their performances are often undermined by difficulty of the n-doping process and their poor stability during cycling due to volumetric changes during doping-dedoping process. In addition, the electrochemical activity of conducting polymer is often restricted by its working potential range and low polymer degradation potential. [23]

2.2.2.1.2 Transitional Metal Oxides

Transition metal oxides are generally considered an attractive alternative as electrode material for as they exhibit high specific capacitance. They process a variety of oxidation states readily available for redox charge transfer, thus add on to the existing double layer storage.

2.2.3 Materials for Electrochemical Capacitor

2.2.3.1 Materials for EDLC

2.2.3.1.1 Activated Carbon

Amorphous carbon is the most widely researched electrode material, with activated carbon being the most common. Their reported specific capacitance is in the range of 30 to 100 Fg^{-1}.[24] Other carbonaceous material such as graphite powder, carbon black, carbon aerogel and carbon fibers have capacitance of 35, 10, 23 and 6.9 μF cm^{-2}, respectively.[25] High electrical conductivity and specific surface area are the crucial factors determining the specific capacitance of EDLC.

2.2.3.1.2 Carbon Nanotubes

CNT being another form of carbon is also being invested intensively due to its high surface area to volume ratio, suitable mesoporous pore size, good chemical stability and excellent electronic conductivity.[26-28] The entanglement of nanotubes has enabled better ions diffusion to the active surface sites, and percolation of active electrolytes is also made more efficient.[29] CNT also have great cycling performance as nanotubular architecture generally has a high resilience to volumetric changes during charge and discharge.

Untreated SWNTs generally have specific capacitance ranging from 50-100 F g^{-1}.[30] Substantial works have also been done to increase the volumetric capacitance by using aligned CNTS as electrodes for EDLCs.[31, 32] The aligned nanotubes known as

nanotubes "forest" has a finer dimension and more uniform distribution exhibited greater energy storage. However, the high cost and complexity of the fabrication process limits their commercial utilization presently.

2.2.3.1.3 Graphene

Graphene, a two dimensional single layer material comprises of an atom thick hexagonal carbon lattice with delocalized electron, is emerging as a promising candidate for supercapacitor. Its high theoretical surface area of 2630 m^2 g^{-1} coupled with good electronic conductivity, excellent thermal conductivity, outstanding strength and reasonable chemical stability have rendered itself useful for charge transport and storage application.[33-36]

Although high specific capacitance of 200 F g^{-1} has been reported for graphene in aqueous electrolyte, commonly cited values are much lower. The performance is strongly dependant on the synthesis routes, porosity and the surface functional groups.

2.2.3.2 Electrically conducting polymers

Electrically conducting polymers make good pseudocapacitive material for electrode of supercapacitors. They possess good electronic conductivity, have low cost, and adjustable redox activity through chemical modification.[37, 38] They are capable of pseudocapacitive storage through the redox process. Ions are transferred to the polymer

backbone when oxidation occurs and vice versa. The processes have good reversibility as the redox reactions do not alter the structures.[39]

ECPs can be either positively or negatively charged. The injected charges can be balanced by the insertion of ions in the polymer matrix. Electronic conductivity can thus be induced via such oxidation and reduction reactions which generate delocalized electrons. Such oxidation and reduction processes are termed as doping. Oxidation induced positively charged polymer are termed as p-doped, while reduction induced negatively charged polymer are termed as n-doped.

Table 2-1 depicts a comparison of capacitance and voltage windows of various electrically conducting polymers and composites in different electrolytes for supercapacitors.

Table 2-1: A comparison of capacitance and voltage windows of various electrically conducting polymers and composites in different electrolytes for supercapacitor.

Material	Electrolyte	Working Voltage (V)	Specific Capacitance (F/g)	Scan Rate (mV s^{-1}) or Current Rate (A g^{-1})	Reference Electrode	System	Cycles	Reference
PANI-20wt% MWNT	1M H_2SO_4	-0.8-0.4	670	2 mV s^{-1}	Hg/Hg_2SO_4	3E	-	[40]
Ppy20wt% MWNT	1M H_2SO_4	-0.6-0.2	506	5 mV s^{-1}	Hg/Hg_2SO_4	3E	-	[40]
PEDOT/Ppy (5:1)	1M KCl	-0.4-0.6	290	2 mV s^{-1}	SCE	3E	1000	[41]
Ppy10%-Carbon	6M KOH	-1-0	235	1 mV s^{-1}	Hg/HgO	3E	2000	[42]
Ppy21%-Carbon	6M KOH	-1-0	322	1 mV s^{-1}	Hg/HgO	3E	2000	[42]
Ppy63%-Carbon	6M KOH	-1-0	390	1 mV s^{-1}	Hg/HgO	3E	2000	[42]
Ppy35%-Carbon	6M KOH	-1-0	433	1 mV s^{-1}	Hg/HgO	3E	2000	[42]
Ppy-MWNT	1M H_2SO_4	-0.4-0.6	427	5 mV s^{-1}	Ag/AgCl	3E	-	[43]
Ppy-RuO_2	1M H_2SO_4	-0.2-0.7	302	0.5 mA/cm^2	Hg/HgO	3E	-	[44]
Ppy	0.5M H_2SO_4	-0.5-0.5	250	50 mV s^{-1}	Ag/AgCl	3E	5000	[45]
Ppy-MnO_2	0.5M H_2SO_4	-0.5-0.5	602	50 mV s^{-1}	Ag/AgCl	3E	5000	[45]

PANI-F	2M H_2SO_4	-0.2-0.8	280	0.1 A g^{-1}	Ag/AgCl	3E	5	[46]
PANI80wt%-graphene	2M H_2SO_4	-0.2-0.8	410	0.1 A g^{-1}	Ag/AgCl	3E	5	[46]
PANI50wt%-graphene	2M H_2SO_4	-0.2-0.8	155	0.1 A g^{-1}	Ag/AgCl	3E	5	[46]
PANI10wt%-graphene	2M H_2SO_4	-0.2-0.8	212	0.1 A g^{-1}	Ag/AgCl	3E	5	[46]
PANI-CNT	1M H_2SO_4	-0.2-0.7	1030	5.9 A g^{-1}	SCE	3E	5000	[47]
PEDOT:PSS-RuO_2	0.5M H_2SO_4	0-0.9	1409	50 mV s^{-1}	Ag/AgCl	3E	-	[48]
PEDOT-MWNT (70:30wt %)	1M H_2SO_4	0-0.8	120	2 mV s^{-1}	-	2E Symmetrical Type I	3000	[49]
PEDOT-MWNT (70:30wt %)	1M $TEABF_4$in AN	0-0.8	60	2 mV s^{-1}	-	2E Symmetrical Type I	3000	[49]
Ppy-Graphene	1M NaCl	0-1.0	165	1 A g^{-1}	-	2E Symmetrical Type I	1000	[50]

Abbreviations: AC: activated carbon, PANI: polyaniline, PEDOT: poly(4-styrenesulfonate), PSS: poly(styrenesulfonate), Ppy: polypyrrole, PMeT: poly(3-methylthiophene), CNT: carbon nanotubes, MWNT: multi-walled nanotubes, AN: acetonitrile.

2.2.3.3 Transitional Metal Oxides

Ruthenium Oxides

Among the transition metal oxides, RuO_2 is the most widely researched due to its high specific capacitance and good electrical conductivity.[51] Its hydrous form, $RuO_2.H_2O$ has shown a high specific capacitance of up to 768 Fg^{-1}.[52] Higher capacitance is ascribed to the additional proton (H^+) intercalation into the hydrated amorphous lattice whereas crystalline RuO_2 involve only surface and near surface redox reaction. The author also reported that water is essential for proton (H^+) diffusion into the amorphous lattice. Such structure also process excellent chemical stability and good electrical conductivity of the order of 10 S cm^{-1} necessary for good capacitor performance.[53] Accordingly, the reaction for the redox reaction is given by [54],

$$H_\alpha RuO_2.xH_2O + \delta H^+ + \delta e^- \leftrightarrows H_\alpha + \delta RuO_2.xH_2O$$

Recent studies have revealed that nanostructures enhance the capacitance of RuO_2. RuO_2 in various forms, nanorods [55], exfoliated nanosheets [56], nanoparticles [57], and nanotubes array [58] have shown improved specific capacitance. However, their scarcity and high cost severely hindered its application in commercial supercapacitor. Although making ruthenium containing composite might reduce the cost, such approach often undermines the capacitance.[44, 59, 60] Hence, considerable effort was spent researching alternative cost effective transitional metal oxides system capable of redox reaction.

Manganese Oxides

Manganese oxide such as MnO_2 has shown attractive capacitance besides having a lower toxicity and cheaper cost. Composites based on MnO_2 have been extensively investigated for supercapacitor application. Goodenough et al.[61] initially reported amorphous MnO_2 composite electrode exhibiting a pseudocapacitive response in mild aqueous electrolyte with a decent specific capacitance of 200 F g^{-1}. There are several oxidation states available for manganese oxides, including Mn(0), Mn(I), Mn(II), Mn(III), Mn(IV), Mn(V), Mn(VI), Mn(VII).[62] It has been postulated that charge storage processes in MnO_2 is accompanied by the intercalation and de-intercalation of both proton (H^+) and surface adsorption of alkali cations (M^+). [63, 64] The respective electrode reactions are shown as follow.[65, 66]

$$MnO_2 + \delta H^+ + \delta e^- \leftrightarrows H_\alpha + \delta MnOOH_\delta \ (0 < \delta < 1)$$

$$(MnO_2)_{surface} + M^+ + e^- \leftrightarrows H_\alpha + (MnOO^-M^+)_{surface}$$

Since only the outer surface of electrode is used for charge storage, a decrease in particles size will result in better utilization of material. Also, the diffusion of cations will be eased along with better proton (H^+) intercalation and de-intercalation. Toupin et al.[63] has demonstrated that nano-metric amorphous MnO_2 thin film exhibits an ultrahigh specific capacitance of 1380 Fg^{-1}. However, due to the low diffusivity of protons and alkali cations in conventionally prepared MnO_2 particles in presence of binder, the specific capacitance is often below 200 Fg^{-1}. One shortcoming of MnO_2 symmetrical device is lack of oxidation states in manganese at negative potential.[8, 67] Thus,

research effort was spent on utilizing MnO_2 as a positive electrode in asymmetrical device. [8, 68]

Tin Oxides

Tin oxide based (SnO_2 and SnO_x) materials being applied in supercapacitor application have also been reported.[69] Alkali metal cations play a critical role charge-discharge mechanism in SnO_x.[70] It is proposed that surface adsorption (desorption) of cations (M^+) along with proton (H^+) and cations (M^+) intercalation (de-intercalation) occur simultaneously as follow,

$$(SnO_x)_{surface} + M^+ + e^- \leftrightarrows H_\alpha + (SnO_x^- M^+)_{surface}$$

$$SnO_x + H^+ + \delta e^- \leftrightarrows SnO_xH$$

$$SnO_x + M^+ + \delta e^- \leftrightarrows SnO_xM$$

Vanadium Oxides

Amorphous vanadium oxides (V_2O_5) have also received considerable attention as candidate for supercapacitor material. Initially, Lee et al. has reported its supercapacitive behavior in aqueous KCl electrolyte. [71] They proposed that the K^+ cations in the KCl electrolyte actually contribute to supercapacitive redox reaction. Similar to MnO_2, charges reside mainly on the surface, with limited ions diffusion distance of ca 30 to 50 nm. [72] Often, conducting matrices such as carbon and CNT are incorporated into V_2O_5 to enhance pseudocapacitive yield. Indeed, nano-metric thick amorphous hydrated

vanadium oxide ($V_2O_5.xH_2O$) thin film electrodeposited on CNT has shown improved specific capacitance.[73, 74] Sofiane et al. have shown that specific capacitance actually falls off with increasing thickness of V_2O_5. [74]

Iron Oxides

Iron oxide (α-Fe_2O_3) is an attractive candidate for supercapacitor due to its low cost, abundance and environmentally benign. The specific capacitances of iron based materials are dependent on the surface morphology and generally reported to be 5-210 Fg^{-1}.[75-78] Electrochemical capacitive behavior is reported to be enhanced by switching to nano-sized materials. Large capacitances have also been reported in sulfites solution with capacitive current deriving entirely from the EDL alone.[79] However, their poor electronic conductivity has restricted their applications in high power devices. CNTs have been added to improve the conductivity with moderate success. Zhao et al. [80] have reported a hybrid supercapacitor made of MWNTs and α-Fe_2O_3/MWNTs thin film having a high energy density of 50 Wh kg^{-1} at a specific power density of 1 kW kg^{-1} over a potential range of 0-2.8V. However, the specific capacitance was reduced by 92% when the scan rate was increase from 2 to 200 mV s^{-1} due to sluggish kinetics and poor electron transport within the α-Fe_2O_3 film.

Another form of iron oxide (Fe_3O_4) has also been investigated for supercapacitor application. Yet, the low specific capacitance limits its practical application.[81, 82] Chen et al. [77] has reported a moderately low specific capacitance of 118.2 F g^{-1}, which

is among the highest reported value so far. Fe_3O_4 also suffers low capacitance retention of 88.8% after 500 cycles.

Table 2-2: A comparison of capacitance and voltage windows of various Transitional metal oxides and composites in different electrolytes for supercapacitor.

Material	Electrolyte	Working Voltage (V)	Specific Capacitance (F/g)	Scan Rate (mV s^{-1}) or Current Rate (A g^{-1})	Reference Electrode	System	Cycles	Reference
$RuO_2.xH_2O$	0.5M H_2SO_4	0-1.0	720	2 mV/sec	SCE	3E	-	[52]
Fe_2O_3	1M NaOH	-0.6-0.1	178	5 mV/sec	SCE	3E	-	[83]
MnO_2	0.5M H_2SO_4	-0.5-0.5	225	50 mV/sec	Ag/AgCl	3E	5000	[45]
SnO_2/C	1M H_2SO_4	0-1	37.8	5 mV/sec	Ag/AgCl	3E	-	[84]
Co_3O_4	6M KOH	-0.1-0.5	456	1 A/g	Ag/AgCl	3E	500	[85]
V_2O_5/C	2M KCl	-0.2-0.7	295	5 mV/sec	SCE	3E	-	[86]
MoO_2/C	1M Na_2SO_4	0-1.2	93	0.1A/g	SCE	3E	1500	[87]
Fe_3O_4	1M Na_2SO_3	-1-0.1	118	6mA	SCE	3E	500	[77]
NiO/CNT	1M KOH	0-0.65	260	20A/g	Hg/HgO	3E	1000	[88]
IrO_2/MWNT	0.1M KOH	-0.5-0.5	74	10 mV/sec	Ag/AgCl	3E	200	[89]
MWNT	1M H_2SO_4	0-1	69	10mA	-	2E	-	[90]
SnO_2/MWNT	1M H_2SO_4	0-1	91	10mA	-	2E	-	[90]
RuO_2/MWNT	1M H_2SO_4	0-1	133	10mA	-	2E	-	[90]
TiO_2/MWNT	1M H_2SO_4	0-1	148	10mA	-	2E	-	[90]
MnO_2	1M KNO_3	0-0.6	160	-	-	2E	-	[91]
MnO_2	0.1M K_2SO_4	0-1.0	36	-	-	2E	-	[8]
V_2O_5	2M KCl	0-0.9	190	2mV/sec	-	2E	-	[92]

2.2.4 Asymmetrical Supercapacitor

An aqueous based supercapacitor has particular advantages over its organic counterpart in terms of higher ionic conductivity, lower cost, lower hazards and better power capability. Such devices have lower sensitivity to oxygen and moisture, hence, require less complicated production processes. Convention supercapacitors are made up of two symmetrical electrodes, and have a narrow stable voltage window of 1V resulting in a low energy density.

Recently, asymmetrical supercapacitors which couple electrodes operating reversibly in different potential ranges have been proposed as a promising way to increase voltage in aqueous electrolytes. This asymmetric supercapacitor can reliably operate above 1.23V (the breakdown voltage of water) without gas evolution in aqueous electrolyte. Operation is made possible because the reaction kinetics for gas evolution is slow although thermodynamically feasible. This results in higher energy density according to equation 2.5. Such asymmetrical supercapacitor allows an operating voltage that may approach twice that of EDLC and thus greatly improves the energy density.

Table 2-3: A comparison of capacitance and voltage windows of various asymmetrical supercapacitors in different electrolytes for supercapacitor.

Positive Electrode (Cathode)	Negative Electrode (Anode)	Electrolyte	Working Voltage (V)	Specific Capacitance (F/g)	Energy (Wh/kg)	Power (kW/kg)	Cycles	Reference
MnO_2	AC	1M LiOH	0-1.5	62.4	19.5	-	1500	[93]
MnO_2	AC	0.5M K_2SO_4	0-1.5	-	7	10	23000	[94]
MnO_2	AC	0.5M K_2SO_4	0-1.8	31	17	2	23000	[95]
MnO_2	AC	1M KNO_3	0-2.0	140	21	123	1000	[91]
MnO_2	AC	0.1M K_2SO_4	0-2.0	21	11.7	16	195000	[68]
MnO_2	AC	1M KCl	0-2.0	52	28.8	8	100	[96]
MnO_2	AC	0.1M K_2SO_4	0-2.2	31	17.3	19	10000	[8]
MnO_2	PANI	1M KNO_3	0-1.2	-	5.86	42.1	500	[97]
MnO_2	Ppy	1M H_2SO_4	0-1.4	-	7.37	62.8	500	[97]
MnO_2	PEDOT	1M KNO_3	0-1.8	-	13.5	120.1	500	[97]
MnO_2/C	V_2O_5 NW/MWNT	1M Na_2SO_4	0-1.6	45	16	3.75	100	[98]
MnO_2/MWNT	SnO_2/MWNT	2M KCl	0-1.7	38	20.3	143.7	1000	[99]
MnO_2	Fe_3O_4	0.1M K_2SO_4	0-1.8	21.5	8.1	10.2	5000	[8]
Fe_3O_4	AC	6M KOH	0-1.2	37.9	7.6	0.07	500	[82]
$LiMn_2O_4$	AC	1M Li_2SO_4	0-1.8	56	10	2	20000	[100]
Hydrous V_2O_5	AC	0.5M K_2SO_4	0-1.8	64.4	29	2	10	[101]
NiO	C	6M KOH	0-1.3	38	10	10	1000	[102]
$Ni(OH)_2$/MWNT	AC	6M KOH	0-1.5	96	32	1.5	2000	[103]

MWNT	Fe_2O_3-MWNT	1M $LiPF_6$ in EC:DMC	0-2.8	80	50	1	500	[80]
MWNT	TiO_2 NW	1M $LiPF_6$ in EC:DEC:DMC	0-2.8	11.5	12.5	1.2	600	[104]
AC	TiO_2	1M $LiClO_4$ in EC:DMC	1.2-3.5	44	80	0.35	600	[105]
RuO_2/TiO_2	AC	1M KOH	0-1.4	46	12.5	0.15	1000	[106]
PEDOT-C	AC	1M $TEABF_4$in AN	0-1.5	160	-	-	20000	[49]

Abbreviations: AC: activated carbon, PANI: polyaniline, PEDOT: poly(4-styrenesulfonate),), Ppy: polypyrrole, NW: nanowires, MWNT: multi-walled nanotubes, EC: ethylene carbonate, DEC: diethylene carbonate, DMC: dimethyl carbonate AN: acetonitrile.

2.2.5 Performance of Supercapacitor

The performance of supercapacitor depends on various attributes. Figure 2.4 shows that a supercapacitor can be treated as two capacitors in series.

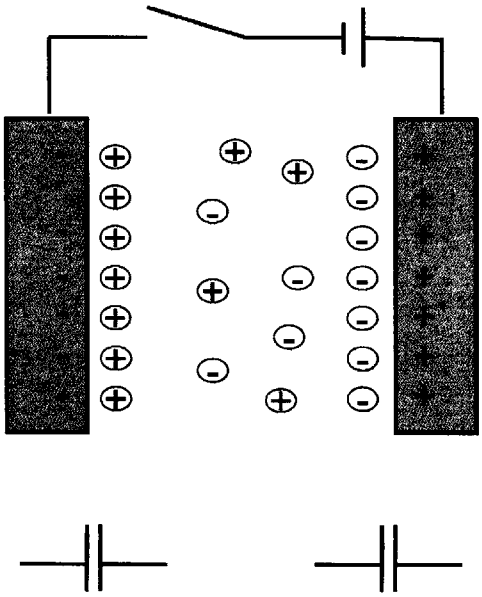

Figure 2.1: Schematic of an electrical double layer capacitor and its circuit equivalent.

The overall capacitance (C_T) can be expressed in terms of capacitance of positive electrode (C_p) and negative electrode (C_n) as:

$$\frac{1}{C_T} = \frac{1}{C_p} + \frac{1}{C_n} \tag{2.4}$$

If the two electrodes are the same, that is capacitance of positive and negative electrode is identical, the overall capacitance (C_T) would be half of the capacitance of one electrode. Such is the case in symmetrical supercapacitor. In the case of asymmetrical supercapacitor, where the electrodes are made of different materials, C_T is mainly dominated by the one with smaller capacitance.

The energy density (E) and theoretical maximum power density (P_M) can be expressed as:

$$E = \frac{1}{2} C_T V^2 \tag{2.5}$$

$$P_M = \frac{V^2}{4R_{ESR}} \tag{2.6}$$

Where C_T is the overall capacitance or device capacitance, V is the operating voltage of the supercapacitor, R_{ESR} is the equivalent series resistance of the supercapacitor.

The operating voltage is determined by the material used for electrode and stability window of the electrolyte involved.

Chapter 3 Experimental Setup

3.1 Fabrication of Electrode Materials

3.1.1 Filtration of CNT Buckypaper

SWNT was prepared by dispersing 30 mg of commercial SWCNT (P3-CNT, Carbon Solution Inc.) 200 ml deionized water, and sonicated for 30 minutes using a bath sonicator. Figure 3.1 illustrates the procedures taken to obtain a bucky paper. The SnO_2 mixed P3-CNT composite was prepared by adding 6 weight percentage of SnO_2 hollow sphere particles to the CNT suspension and stirred for 12 hours to obtain homogenous solution. The suspension was then filtered through a filter membrane (Whatman, 20 nm pore size, 47 mm diameter) using a filter flask and vacuum pump. This mesh was subsequently air dry at room temperature for 24 hours off to peel off as a freestanding thin film with a thickness of approximately 20 μm. The film is then sized appropriately to be used for characterization. An interconnected network of SWNT (pristine or mixed with SnO_2 nanomaterials) is depicted at bottom of Figure 3.1.

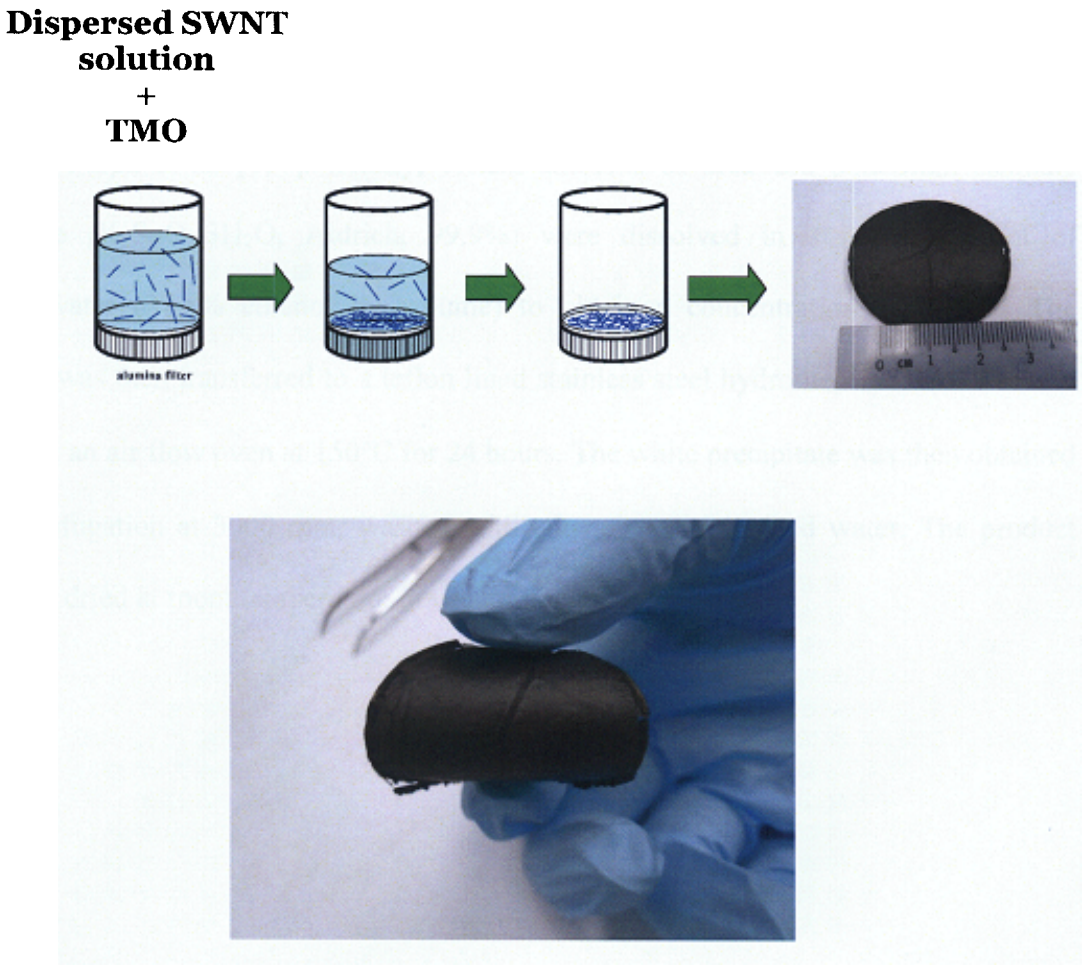

Figure 3.1: (Top) Obtaining CNT bucky paper via vacuum filtration. (Bottom) Photograph of a flexible CNT bucky paper.

3.1.2 SnO_2 and P3-CNT mixture

SnO_2 hollow nanospheres was synthesized in accordance to a method described by X. W. Lou et al. [107]. Briefly, certain amounts of urea and potassium stannate trihydrate ($K_2SnO_3.3H_2O$, Aldrich, 99.9%) were dissolved in a mixed solvent of ethanol/water (37.5% ethanol by volume) to obtain a concentration of 0.1M. The solution was then transferred to a teflon lined stainless steel hydrothermal autoclave and heated in an air flow oven at 150°C for 24 hours. The white precipitate was then obtained by centrifugation at 3000 rpm, washed with ethanol and deionized water. The product was then dried at room temperature in vacuum oven.

3.1.3 Electrospinning of Nanofibers

Electrospinning is a simple facile and economical way to fabricate interwoven nanofibers. Figure 3.2 illustrates the general electrospinning setup. The setup is highly versatile equipped with various parameters such as flow rate, voltage, size of needle and distance between plate and needle to better control the electrospinning process and aspect ratio of the electrospun fibers.

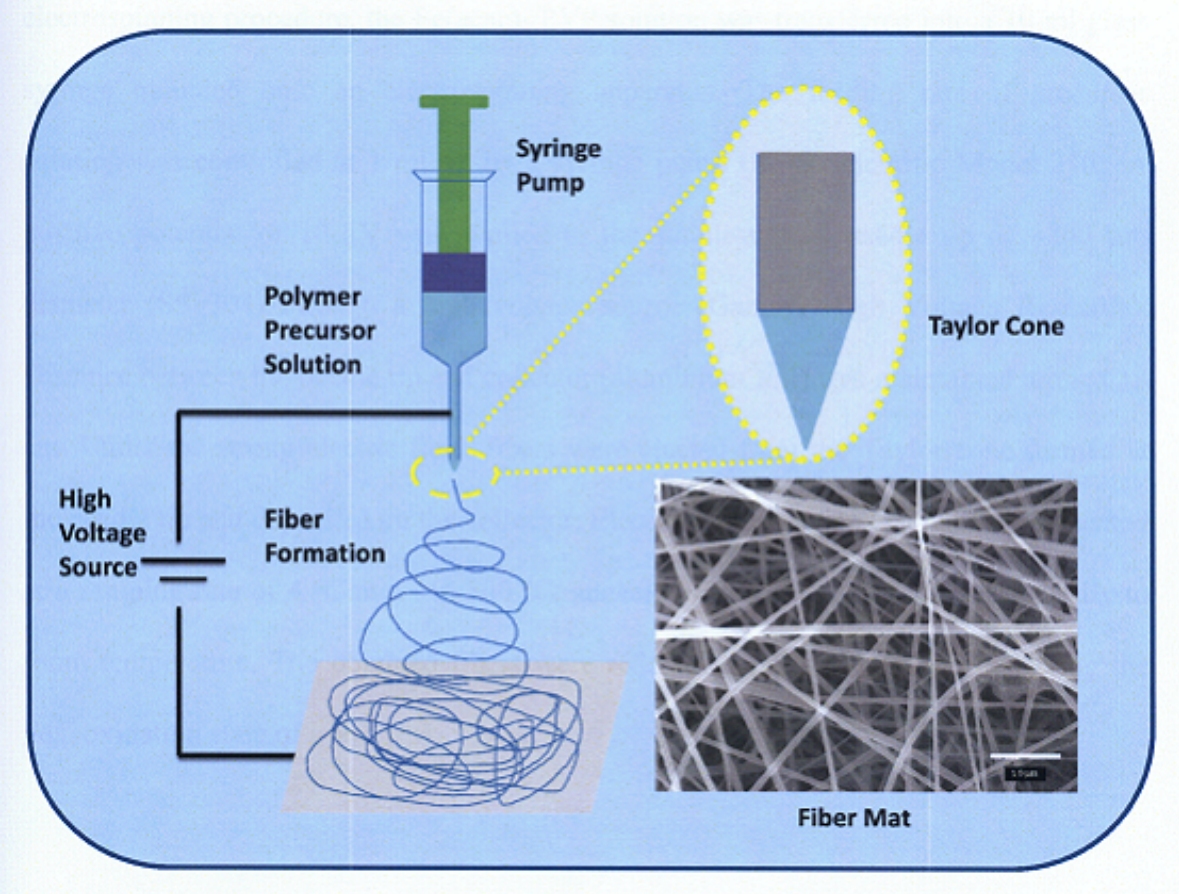

Figure 3.2: Schematic illustration of the Electrospinning Process

3.1.3.1 α-Fe_2O_3 Nanofibers

For synthesis of $Fe(acac)_2$/PVP composite nanofibers, 1 g of Polyvinylpyrrolidone (PVP) (Mw 3,600,000 Fluka) was dissolved in mixture of absolute ethanol (Sigma-Aldrich) and glacial acetic acid (Tedia Company Inc.). Then 0.6 g of iron (II) acetylacetonate ($Fe(acac)_2$, 98% , Sigma-Aldrich) was added, and stirred for 24 h to obtain a homogenous solution. All chemical reagents were used as received. In the electrospinning procedure, the $Fe(acac)_2$/PVP solution was transferred into a 10 ml glass syringe mounted onto an electrospinning apparatus. The feeding rate of precursor solution was controlled at 1 ml h^{-1} by a syringe pump (KDS Scientific Model 210). A positive potential of 10 kV was applied to the stainless steel needle tip of ~200 μm diameter (SS 304) through a high voltage source (Gamma High Voltage Research). Distance between the needle tip and collector (aluminium foil) was maintained around 10 cm. Under the strong electric field, fibers were ejected from the Taylor cone formed at the needle tip and deposited on the collector. Electrospun fibers were subsequently heated at a ramping rate of 4 °C min^{-1} to 500 °C, annealed for 5 hours, and cooled naturally to room temperature. The obtained fibers were reddish mats in appearance indicating the Fe^{3+} oxidation state of iron.

3.1.3.2 V_2O_5 Nanofibers

In making $VO(acac)_3$/PVP composite nanofibers, 1 g of Polyvinylpyrrolidone (PVP) (Mw 3,600,000 Fluka) was dissolved in mixture of absolute ethanol (Sigma-Aldrich) and glacial acetic acid (Tedia Company Inc.). Then 0.6 g of vanadyl acetylacetonate ($VO(acac)_3$, 98% , Sigma-Aldrich) was added, and stirred for 24 h to obtain a homogenous solution. All chemical reagents were used as received. In the electrospinning procedure, the $VO(acac)_3$/PVP solution was transferred into a 10 ml glass syringe mounted onto an electrospinning apparatus. The feeding rate of precursor solution was controlled at 1 ml h^{-1} by a syringe pump (KDS Scientific Model 210). A positive potential of 10 kV was applied to the stainless steel needle tip of ~200 μm diameter (SS 304) through a high voltage source (Gamma High Voltage Research). Distance between the needle tip and collector (aluminium foil) was maintained around 10 cm. Under the strong electric field, fibers were ejected from the Taylor cone formed at the needle tip and deposited on the collector. Electrospun fibers were subsequently heated at a ramping rate of 2 °C min^{-1} to 500 °C, annealed for 30 minutes, and cooled at 2 °C min^{-1} to room temperature. The obtained fibers were yellowish in colour indicating the V^{5+} oxidation state of vanadium.

3.1.4 Rapid Polymerization of Polyaniline Nanofibers

PANF was synthesized by rapid mixing polymerization [108]. The oxidant dopant solution was prepared by dissolving 25 mmol of ammonium persulfate (98% Sigma-Aldrich) in 50 ml deionized water, and stirred for 30 min. Aniline dopant solution was made by adding 20 mmol of aniline (Sigma-Aldrich) into 50 ml deionized water, and stirred for 30 min. The oxidant solution is then quickly added to the aniline solution and stirred vigorously for a minute, and left to polymerized for an hour. After the polymerization, the dark green residue was washed with 300 ml of 0.2 M HCl solution followed by 300 ml of acetone to remove residual ammonium persulfate and aniline monomers respectively. The dark green residue was then dried at 50 °C in vacuum for 12 hours.

3.2 Fabrication of Composite Electrode

The test electrodes were prepared by dispersing VNFs or PANFs, super P (99%, Alfa Aesar) and poly-vinylidenefluoride (PVdF) (Sigma-Aldrich) in *N*-methylpyrrolidone (NMP) (Sigma-Aldrich) with a weight ratio of 75:15:10, respectively to form slurry. Resultant slurry was then coated onto a 1 cm^2 area of graphite paper and subsequently dried at 60°C for an hour. The mass loading of electrode material is ca. 2 mg.

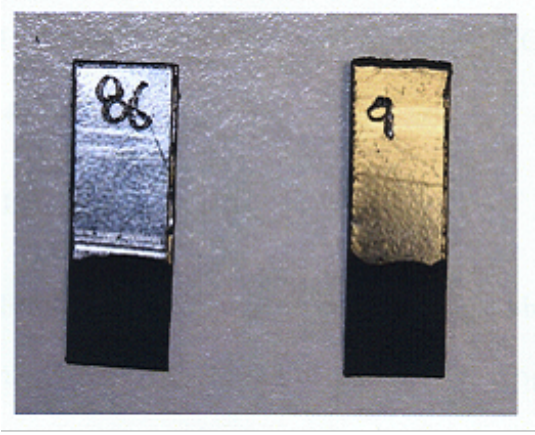

Figure 3.3: Photograph of electrodes coated with composites

3.3 Physical Characterizations

3.3.1 Field-Emission Scanning Electron Microscopy (FESEM)

The surface morphologies of the nanostructured electrode materials were investigated using a field-emission scanning electron microscope (JSM 6340 F) operating with accelerating voltages of 5 kV to 10 kV. Samples were prepared by pasting the subject onto the stainless steel holder using carbon tapes. All samples were coated with ca. 15-25 nm of using a platinum sputter (JEOL JFC-1600) prior to microscopy to avoid charging effect.

3.3.2 Powder X-ray Diffraction (XRD)

Powder X-ray diffraction (XRD) was performed using a Shimadzu diffractometer (Cu-k_α) with step scanning (0.01°, 0.5 s dwell time) over a 2θ range of 10° to 140°. The patterns were analyzed by applying the Rietveld method using fundamental parameters approach contained within the software TOPAS V3 (Bruker-AXS).

3.3.3 High Resolution Field Emission Transmission Electron Microscopy

The high resolution TEM (HRTEM) images were performed at 200kV by using a JEOL JEM-2100F transmission electron microscope equipped with high contrast objective aperture (20μm in diameter) equivalent to a point to point resolution of 1.7Å.

3.3.4 Nitrogen adsorption-desorption isotherm

The nitrogen adsorption-desorption isotherms were obtained at 77 K using a NOVA 3200e system. The BET surface area of the samples was determined by investigating the nitrogen desorption isotherms using a NOVA 3200e system at 77 K. The samples were degassed at 373 K under nitrogen flow for 24 hours prior to measurement. Pores size distributions were investigated by applying Barrett-Joyner-Halenda (BJH) analysis on the nitrogen desorption isotherm obtained.

3.3.5 Thermo gravimetric Analysis (TGA)

The experiment was carried out with a heating rate of 2 °C min^{-1} or 10 °C min^{-1} from room temperature to 800°C using the TGA Q500 Series from TA. Gas flow consisting of a mixture of synthetic air and nitrogen gas in the percentage ratio of 40:60 was maintained.

3.3.6 Fourier Transform Infrared Spectroscopy (FT-IR)

In a typical experiment, potassium bromide and a small amount of the nanofibers are mixed homogenously using a mortar and pestle. The mixture was then transferred to a mould and subjected to a pressure of 10 kPa for 5 minutes. A highly transparent disc containing less than 2% weight ratio of the testing subject (nanofibers) was obtained. Infrared spectroscopy was then performed on the disc, scanned sixteen times over the range of 4000-400 cm^{-1} using Perkin-Elmer Spectrum GX FTIR.

3.3.7 X-ray Photoelectron Spectroscopy (XPS)

X-ray photoelectron spectroscopy (XPS) spectra were recorded using a Kratos AXIS Ultra spectrometer with the monochromatic Al Kα X-ray radiation. Deconvolution and peak fitting were performed with computer assisted surface analysis XPS software (CASA) using a Voigt function with 30% Lorentzian character and a Shirley background.

3.4. Electrochemical Characterization

3.4.1 Cyclic Voltammetry (CV)

The electrochemical behaviors of the electrode material were investigated using cyclic voltammetry measurements carried out in various configurations, including three electrode configuration, two electrode symmetrical and asymmetrical device configurations. A standard three electrode cell configuration is consisted of a working electrode (electrode material under evaluation), platinum foil (5 cm x 5 cm) as counter electrode, and saturated calomel electrode (SCE) or silver chloride electrode (Ag/AgCl in 3M KCl) as reference electrode. All the experiments were conducted using a computer controlled potentiostat (Solartron 1470E).

3.4.2 Galvanostatic Charge-Discharge (GCD)

Galvanostatic charge-discharge performances were conducted in a two electrode configuration. The measurements were taken using a computer controlled potentiostat (Solartron,1470E). Different current densities were employed to investigate the rate capability of the various materials. Effect of organic electrolyte such as $LiClO_4$ was also studied.

3.4.3 Electrochemical Impedance Spectroscopy (EIS)

Electrochemical impedance for all the devices was measured using a frequency response analyzer from Solartron (SI 1255B impedance/gain-phase analyzer with Zview software) in potentiostatic mode with AC amplitude of 10 mV, from 10 kHz to 10 mHz.

Chapter 4 Results and Discussions

This chapter details the results of various experiments undertaken in this thesis. Firstly, P3-CNTs being commercially available are first explored as a working prototype, underpinning subsequence research work. It was subsequently mixed with materials such as SnO_2 in attempt to increase the capacitance via pseudocapacitance.

Electrospinning was employed to synthesize nanofibers to investigate the effect of morphology in capacitive performance. TMO nanomaterial such as Fe_2O_3 and V_2O_5 were electrospun and their performances investigated. The effect of conducting additive such as carbon black is also studied. Also, the performance of Fe_2O_3 in various electrolytes is looked into. Their superior electrochemical behaviors brought about by the nanostructure were also investigated. In addition, V_2O_5 nanofibers and other class of materials like electronically conducting polymer (ECP) such as polyaniline were also studied.

To increase the energy density, asymmetrical configuration was employed to increase the working potential. A common electrolyte was judiciously selected in which both the electrode material can function as supercapacitor electrode. Their electrochemical behaviors and performances were being investigated and compared. A correlation of the charge storage mechanism of the supercapacitor with the conducting additive, morphology, surface area and interfacial properties had been investigated through various electrochemical characterization techniques.

4.1 Investigation of Electrode Materials for Symmetrical Supercapacitor Application

4.1.1 CNT based Supercapacitors

Firstly, the use of CNTs as both active electrode material and the current collector was explored. CNTs have high surface area, conductivity and aspect ratio which make them a good candidate for electrode material in supercapacitor application. As P3-CNTs are commercially available, attempts to fabricate supercapacitors were made using P3-CNTs.

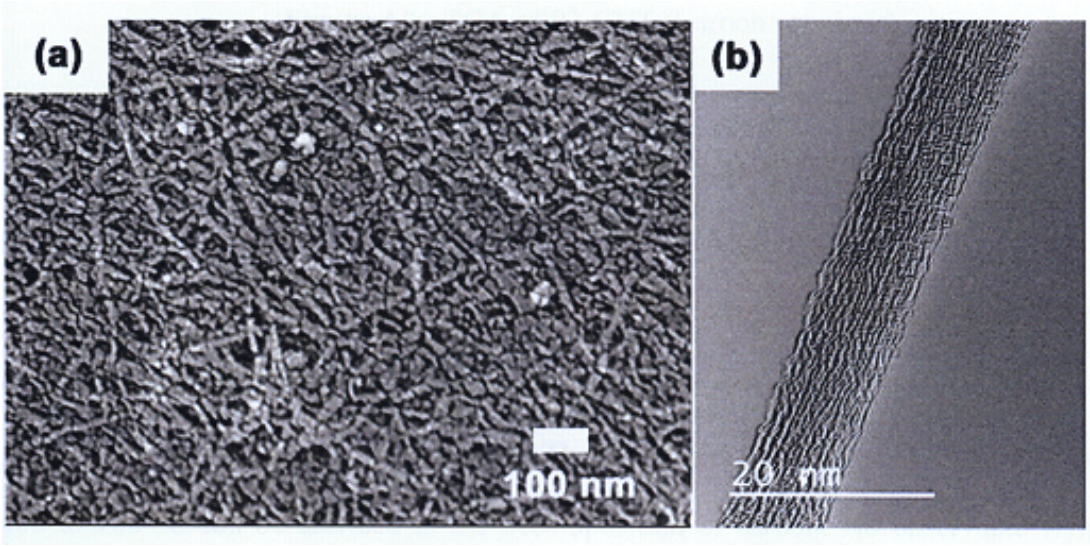

Figure 4.1 : (a) FESEM image of P3-CNT (Carbon solutions) bucky paper. (b) HR-TEM image of a bundle of P3 CNT.

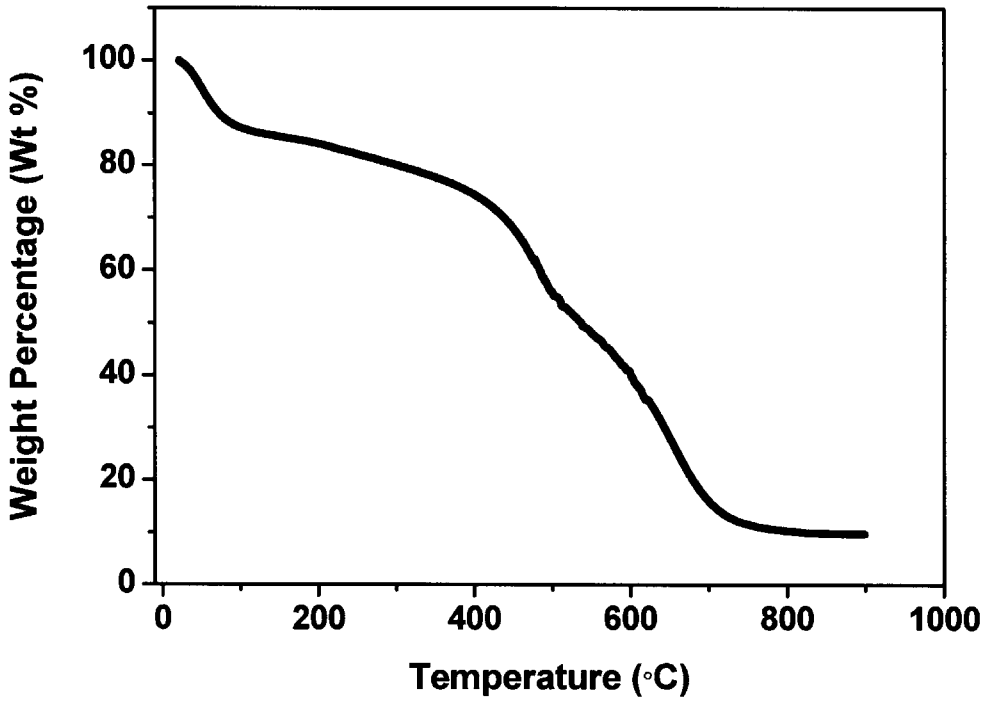

Figure 4.2 : TGA of P3-CNT (Carbon solutions).

Figure 4.2 illustrates the thermal gravimetric analyses of P3 CNTs. There is a gradual weight loss observed for P3 CNT at lower temperature (ca. 100 °C) due to moisture left behind by the filtration process. There is some weight loss of ca. 10 wt% over the range of 200 to 400 °C, probably due to the decomposition of the functional groups such as carboxylic, and hydroxyl. The significant drop in wt % occurring from 400 to 700 °C can be ascribed to the decomposition of carbon. No observable weight change is noted beyond 750 °C, indicating the completion of carbon combustion. The incombustible residual can be ascribed to the metal catalysts impurities used during the

growth process of the CNTs. The final residual weight of 9.8 wt% was obtained for P3-CNT suggesting a purity of more than 90%.

Bucky papers of P3-CNT were tested in various electrolytes of 1M H_2SO_4, 1M Na_2SO_4 and 3M KCl in three electrode configuration with SCE as reference.

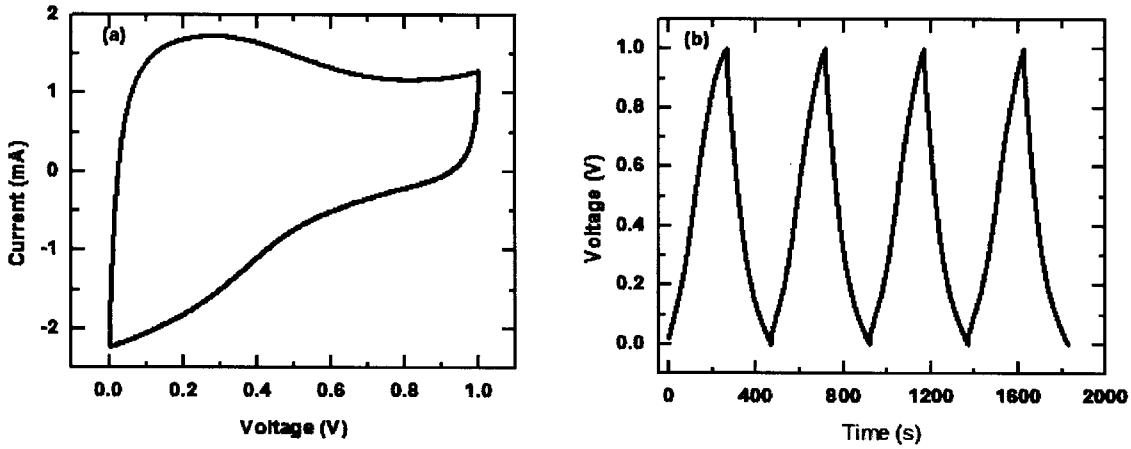

Figure 4.3 : (a) 2-electrode Cyclic Voltammogram (b) 2-electrode Galvanostatic charge-discharge of P3-CNT bucky paper in 1M H_2SO_4 electrolyte.

Figure 4.3 illustrates the electrochemical CV and GCD curves of P3-CNT bucky paper tested in 1 M H_2SO_4 electrolyte. The peak observed in the CV curve at ca. 0.25 V can be attributed to faradic contribution from the oxygenated functional groups. In general, the deviation from an ideal box-shape CV curve of a supercapacitor without internal resistance (dotted line) can be explained by the presence of functional groups, impurities, and a decreased conductivity due to the absence of a dedicated current collector.

The specific capacitance of the device from the GCD test is calculated to be 87 F g^{-1}. Besides CV measurements, GCD test is another device characterization that can be employed to evaluate the specific capacitance and internal resistance of a SC device. Figure. 4.3 (b) shows GCD curve of the same device measured at a constant current of 1 mA. Each branch of the entire curve starts with a voltage drop (IR drop). As P3-CNT exhibits electrical double layer capacitive property, ways to improve the capacitance will be investigated.

4.1.2 SnO_2-CNT mixture based Supercapacitors

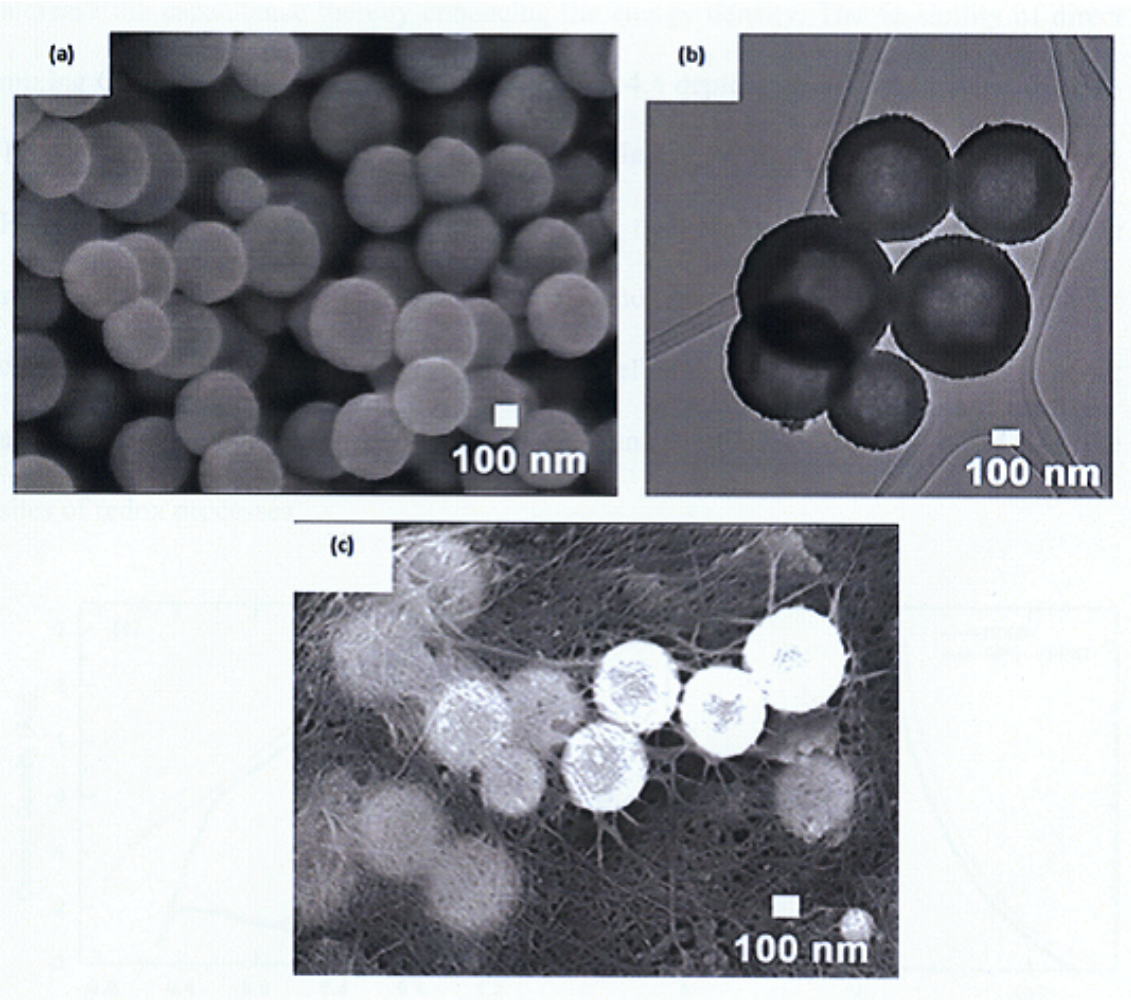

Figure 4.4: (a) FESEM image of SnO_2 hollow spheres (b) HR-TEM image of SnO_2 hollow spheres (c) FESEM image of P3-CNTs mixed SnO_2 hollow spheres.

Pseudocapacitive materials such as transition metal oxides were introduced to increase the capacitance thereby enhancing the energy density. The feasibility of direct mixing CNT with SnO_2 was investigated. Figure 4.4 depicts (a) FESEM image, (b) HR-TEM image of SnO_2 spheres and (c) FESEM image of SnO_2 mixed P3-CNT. From Figure 4.4 (b) image, it can be observed that that SnO_2 spheres are hollow which significantly reduce the mass of SnO_2 required and may enable a higher surface area for charge transfer process. The SnO_2 spheres are well embedded into the P3-CNT network as seen in Figure 4.4 (c). This will allow better transportation of electrons to and from the sites of redox processes.

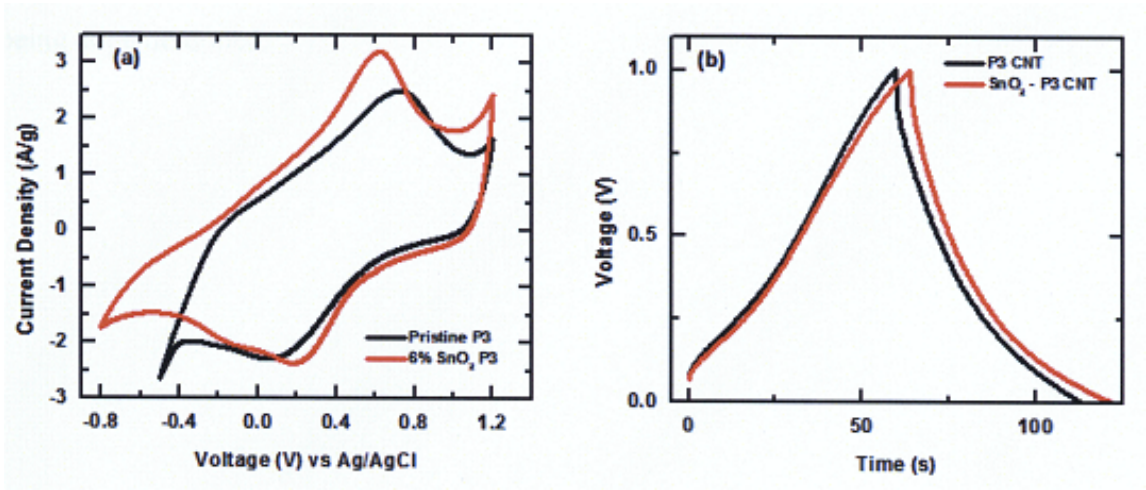

Figure 4.5: (a) 3-electrode Cyclic Voltammogram (b) 2-electrode Galvanostatic charge-discharge of P3-CNT bucky paper and SnO_2 mixed P3-CNT bucky paper in 1M H_2SO_4 electrolyte.

Figure 4.5 depicts the electrochemical performance of both the P3-CNT and physical mixture of SnO_2 P3-CNT electrode in 1 M H_2SO_4 electrolyte. Apparently, addition of SnO_2 does not significantly contribute to the electrochemical performance. The minute increment in pseudocapacitive contribution observed in SnO_2-CNT devices had led to the out-phasing of direct mixing of pseudocapacitive material nanomaterials with CNTs in subsequent investigation.

To continue the effort of improving the energy density of capacitance of materials, other TMO as well as electrically conducting polymers (ECP) were investigated. Candidate materials need to either possesses multiple oxidation states or be capable of being dope/de-doped.

4.1.3 Fe_2O_3 Nanofibers Supercapacitors

Bulk chemical materials have already been intensively researched in many applications. However, the chemistry and performance of many nanomaterials have not yet been widely explored and understood. Nanostructures with high surface area will certainly leads to better capacitance. Currently, there are many routes to synthesize nanomaterials, including hydrothermal [109] and electrospinning [110]. Electrospinning is an economical, easy and reliable method to fabricate high surface area nanofibers with diameters ranging from tens of nanometers to several micrometers with good mechanical strength. It also offers advantages like control over morphology, composition and porosity with simple equipment. Additionally, these nanofibers can often become porous after calcination at suitable temperatures and heating rate [111]. Hence, electrospinning was employed to fabricate nanostructured material in this work.

4.1.3.1 Physical Characterization of Fe_2O_3 Nanofibers

Fe_2O_3 are reported to exhibit pseudocapacitive behavior. Their electrochemical performance is strongly influenced by the surface morphology of the materials, which depends on the methods of preparation. They are also chemically stable, cheap and environmentally benign. As previously mentioned, electrospinning technique was employed to fabricate Fe_2O_3 fibers. $Fe(acac)_2$ was selected as metal acetylacetonate can be decomposed at moderate temperature (< 800 °C) to become metal oxide. The electrospun $Fe(acac)_2$ fibers were subsequently peel off and analyzed using TGA to find the optimum calcination temperature to obtain Fe_2O_3 nanofibers.

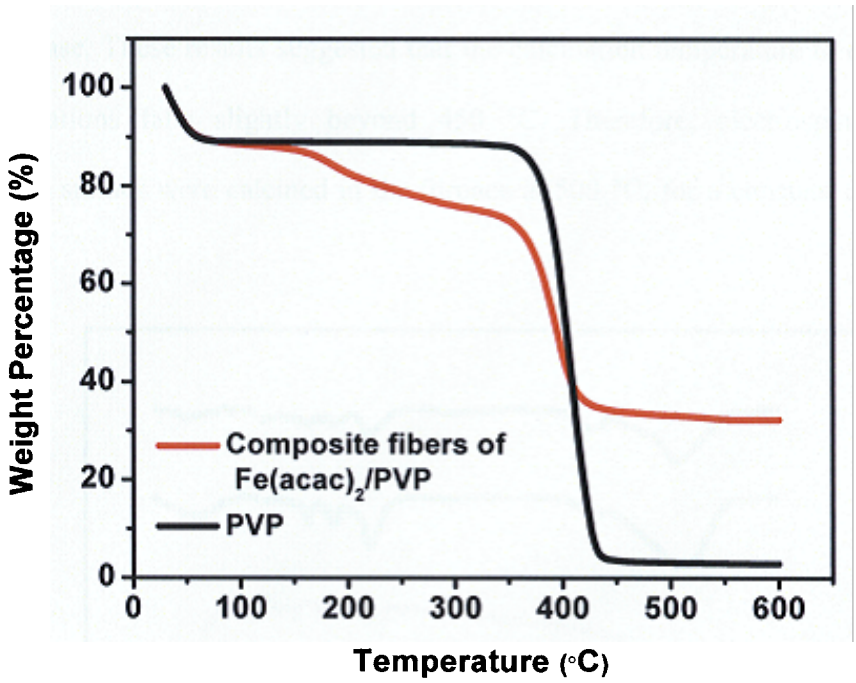

Figure 4.6: TGA of pure PVP and $Fe(acac)_2$/PVP composite fibers.

Figure 4.6 shows the thermal gravimetric analysis (TGA) of as spun $Fe(acac)_2$ nanofibers and PVP respectively. The optimized calcination temperature range of electrospun fibers was studied. The TGA helps to illustrate the thermal behavior of the as spun fibers. Both samples exhibit thermal weight loss below 100°C which can be attributed to the evaporation of moistures present in the PVP. The weight percentage of the FNF continues to decrease gradually in the temperature range of ~100-350 °C, and dropped rapidly at ca. 400 °C. The weight loss from 180°C to 350 °C might be due to the decomposition of $Fe(acac)_2$ and its transformation into α-Fe_2O_3. The subsequent drop in weight at 360 to 400°C is due to the decomposition of PVP into carbon dioxide and water vapor, as evident from the decomposition curve of pristine PVP. The weight stabilization after 450 °C signifies the end of PVP decomposition and complete formation

of Fe_2O_3 phase. These results suggested that the calcination temperature to obtain Fe_2O_3 after calcinations falls slightly beyond 450 °C. Therefore, electrospun fibers for subsequence studies were calcined in the furnace at 500 °C, for a constant duration of 5 hours.

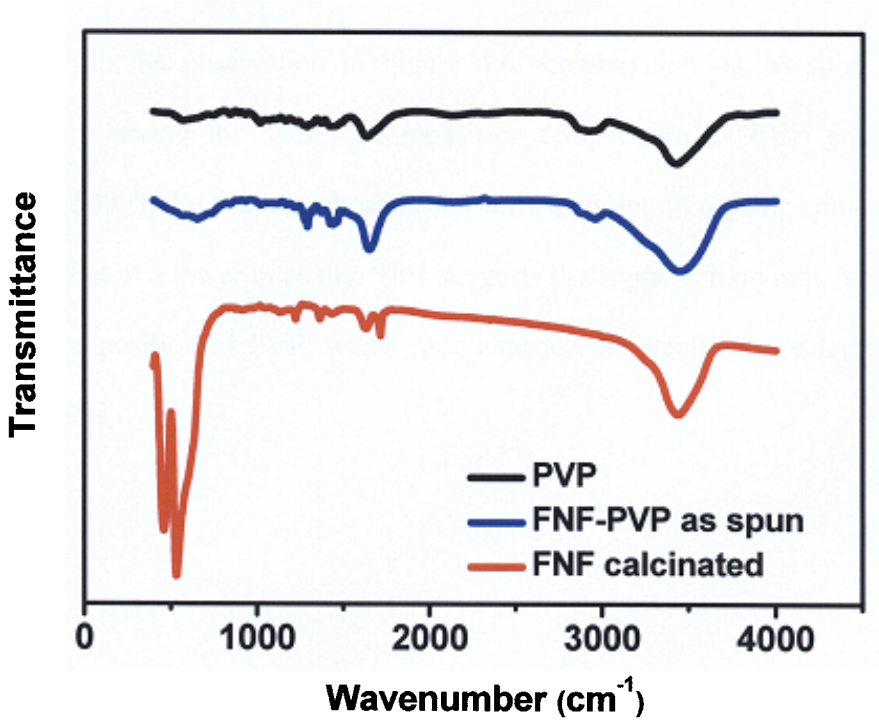

Figure 4.7: FTIR of PVP, as spun FNF-PVP, and calcined FNF respectively.

FT-IR was employed to investigate the bonds present in calcined Fe_2O_3. Figure 4.7 compares the FT-IR spectra of PVP, as spun composite fibers and Fe_2O_3 nanofibers calcined at 500 °C. The broad peak in the general range of 3600–3100 cm^{-1} may be assigned to anti-symmetrical and symmetrical O–H bonding stretching vibrational modes for O-H.[112] Bonding in the region of 1730–1600 cm^{-1} also relates to O–H bonding

bending vibrational modes. [112] The bands at 460 and 532 cm^{-1} observed in Fe_2O_3 calcined at 500 °C can be attributed to stretching vibrational modes of Fe-O. [112]

The absence of observable change of FT-IR spectra of PVP and as spun composite nanofibers suggests that Fe^{2+} may have weak or no interactions with PVP. This agrees with the observation in Figure 4.6 showing that the as spun composite nanofibers was having the same decomposition temperature as PVP powder. After calcination at 500 °C for 5 hours, those bands corresponding to organic components was still observed but at a lower intensity. This suggests that some carbon may be left behind from the decomposition of PVP, which may enhance the electrical conductivity of the Fe_2O_3 nanofibers.

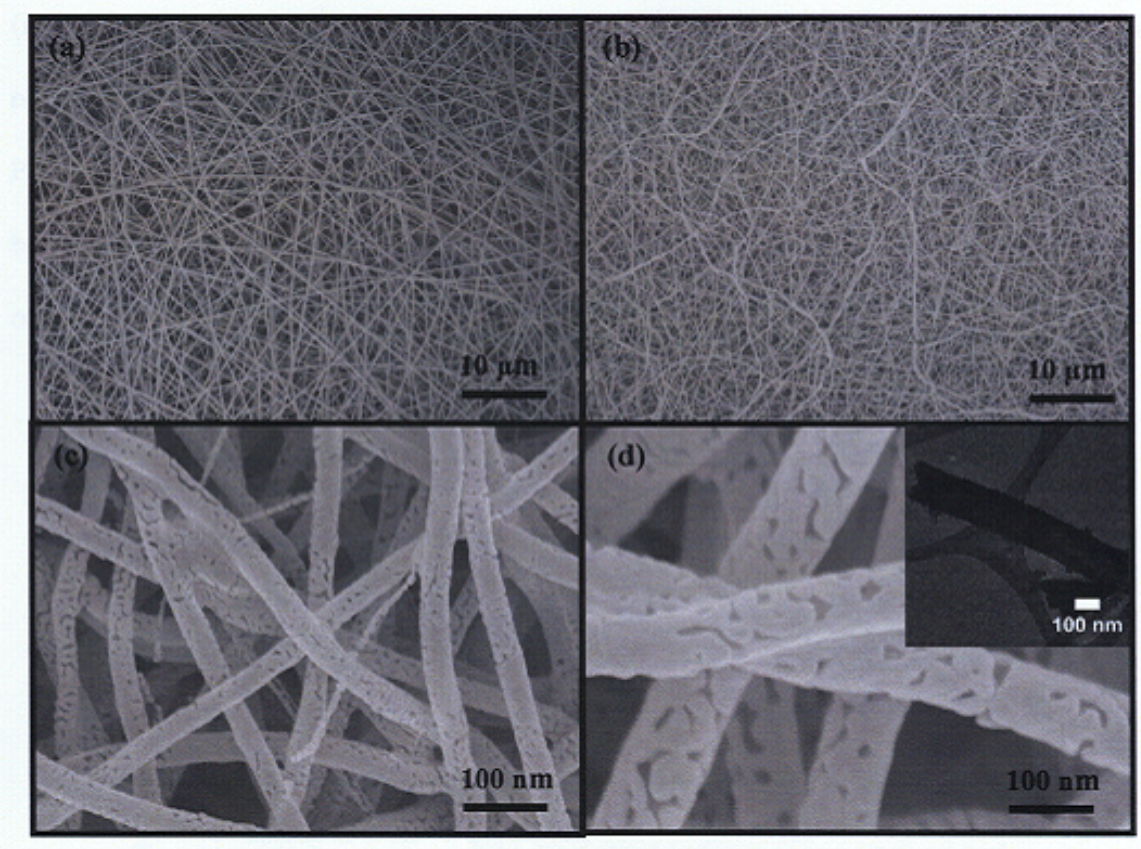

Figure 4.8 : FESEM images of as-spun $Fe(acac)_2$/PVP composite fibers at (a) lower magnification, (b), (c) and (d) nano-porous α-Fe_2O_3 fibers after calcination at 500 °C.

Morphology of the as spun $Fe(acac)_2$/PVP composite fibers and Fe_2O_3 nanofibers calcined at 500°C was investigated by FESEM. Figure 4.8 shows FESEM images of $Fe(acac)_2$/PVP composite fibers and Fe_2O_3 nanofibers. It was observed that the as spun nanofibers were randomly oriented with diameter of 200 – 400 nm and length up to hundreds of micrometers. After undergoing calcination, the nanofibers shrunk to about 4 to 6 times in diameter while maintaining the same fiberous morphology. The annealed Fe_2O_3 nanofibers have diminished overall diameters (40 to 100 nm). The TEM image

(inset of Figure 4.8 (d)) further confirms the shrinkage of the fibers, which also exhibits partial crystallinity. This change in fiber aspect ratio was derived from the elimination of PVP during sintering. This removal of the PVP renders more porous surfaces which are beneficial to the diffusion of ions which is crucial to both the power and energy density of supercapacitors.

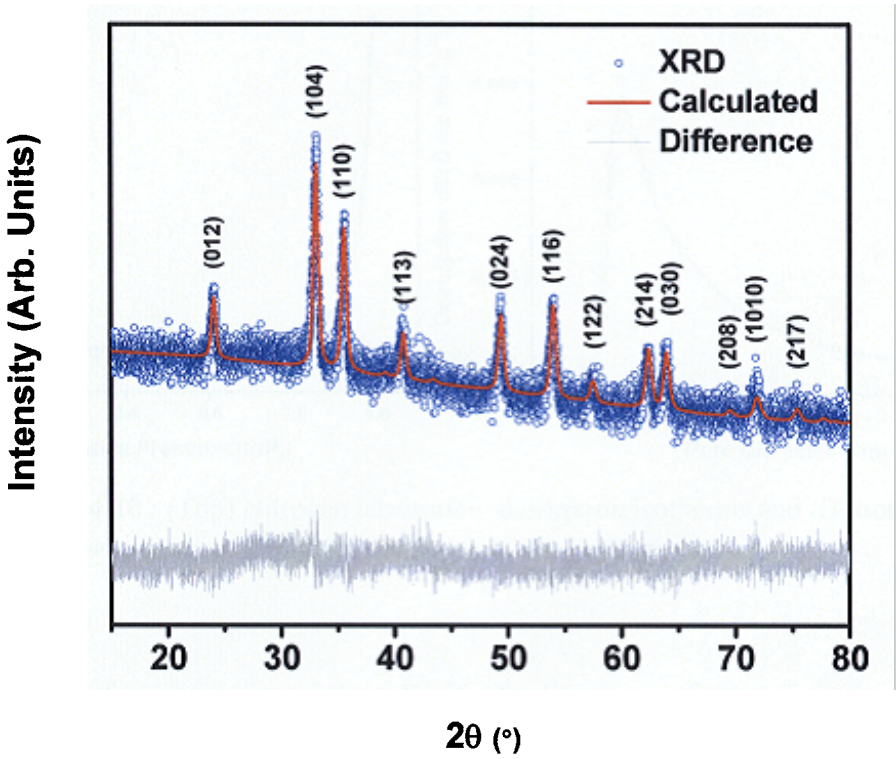

Figure 4.9 : XRD pattern of α-Fe_2O_3 nano-porous fibers.

Identification of the sintered $Fe(acac)_2$ was investigated with XRD. Figure 4.9 shows the X-ray diffraction patterns of electrospun α-Fe_2O_3 nanofibers after annealing at 500°C for 5 hrs. The XRD reveals reflections belonging to space group R-3CH (JCPDS

card no. 33-0664). Rietveld refinement was carried out using TOPAS. Lattice parameters of Fe_2O_3 were calculated as a = 5.036(3) Å, c = 13.76(3) Å, fitted with R-Bragg value of 0.664. This XRD indicates that a single phase of hematite α-Fe_2O_3 has been obtained [113, 114].

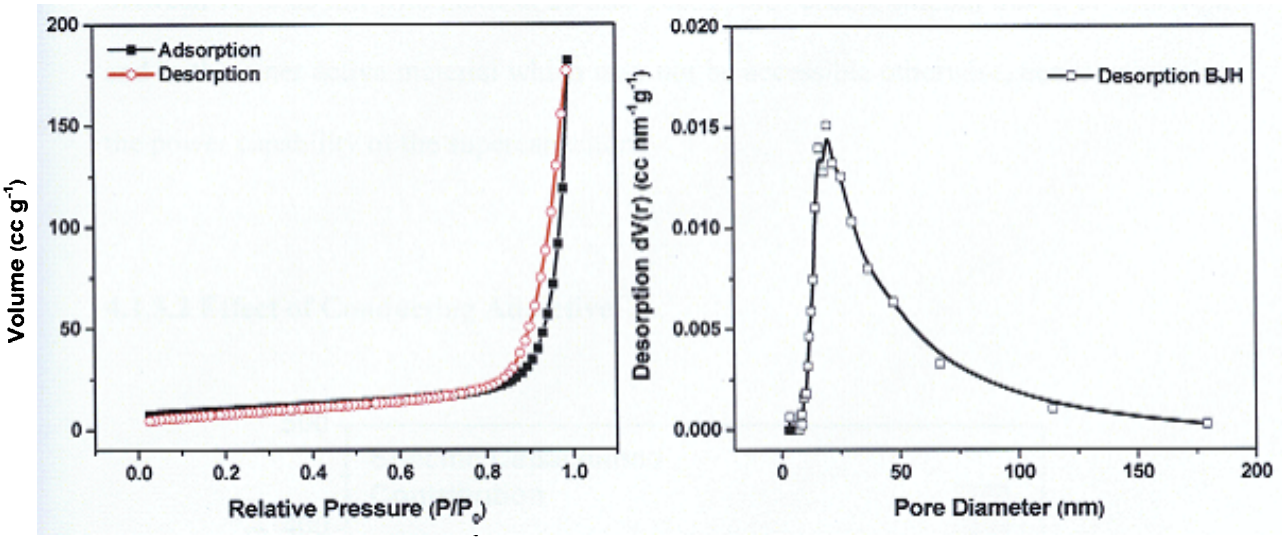

Figure 4.10 : (Top) Nitrogen adsorption–desorption isotherms and (Bottom) BJH desorption isotherm of the nano-porous α-Fe_2O_3 fibers.

The surface properties of the α-Fe_2O_3 nanofibers were further investigated using the nitrogen isotherm. Figure 4.10 (top) presents nitrogen adsorption/desorption isotherms of α-Fe_2O_3 nanofibers at 77 K. Multipoint Brunauer-Emmett-Teller (BET) analysis performed on α-Fe_2O_3 nanofibers gives a specific surface area of 33.95 $m^2 g^{-1}$. The adsorption isotherm exhibited type IV isotherm with type H3 hysteresis between adsorption and desorption isotherms and a steep slope at higher relative pressure,

suggesting mesoporosity. Mesoporous structure is reported to be beneficial to capacitive performance by allowing fast ion diffusion for both double layer formation and surface redox reaction, thus enhancing rate performance. Barrett, Joyner and Halenda (BJH) method was employed to investigate the pore size distribution in α-Fe_2O_3 and depicted in Figure 4.10 (bottom). It is observed that α-Fe_2O_3 nanofibers have pore distribution between 10 to 60 nm with mode at 20 nm. These pores enable smooth traffic of ions from and to the inner active material which may not be accessible otherwise, hence enhancing the power capability of the supercapacitor.

4.1.3.2 Effect of Conducting Addictive

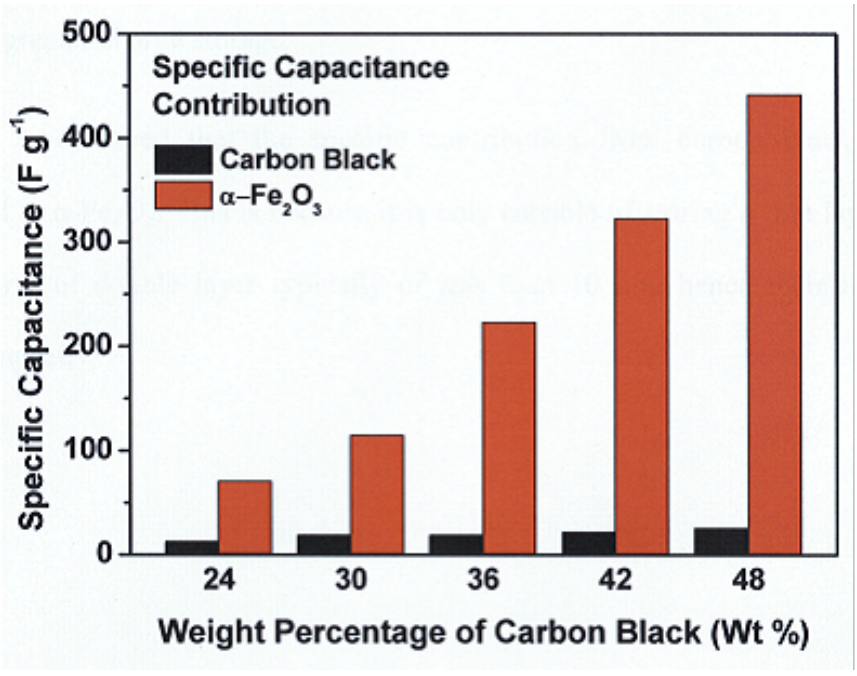

Figure 4.11: Plot of specific capacity contribution from the composite with different carbon black added taken at a current density of 0.1 A g^{-1} in 1 M Na_2SO_4 electrolyte.

The effect of carbon black on the pseudocapacitive behavior of α-Fe_2O_3 is also studied. Figure 4.11 depicts the relationship of specific capacitance with current density taken with different weight percentage of α-Fe_2O_3 and carbon black. It is observed that the pseudocapacitance contributed by α-Fe_2O_3 nanofibers is significantly enhanced with addition of carbon black. Although α-Fe_2O_3 is electrochemically active, it suffers a low electrical conductivity of 10^{-14} S cm^{-1} [76]. Such low conductivity inevitably hinders the utilization of the pseudocapacitive storage of α-Fe_2O_3. Herein, the carbon black functions as an electrical conductor facilitating electrons transfer to and from the sites of redox reactions, thereby improving the utilization of pseudocapacitive sites of α-Fe_2O_3. Also, having more carbon black content ensures better distribution of α-Fe_2O_3 nanofibers. This allows greater amount α-Fe_2O_3 being able to be used for charge transfer and hence realizing greater charge storage.

It is observed that the specific contribution from carbon black is trivial as compared to α-Fe_2O_3. This is because it is only capable of storing a thin layer of charges in the form of double layer typically of less than 10 nm, hence their limited charge storage capacity.

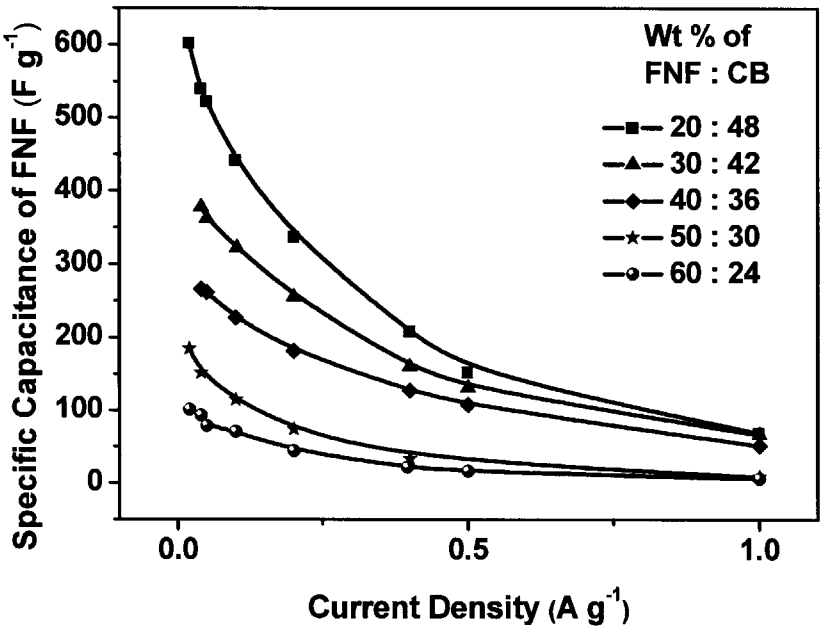

Figure 4.12 : Plot of specific capacitance of α-Fe_2O_3 nanofibers with different weight percentage of carbon black added against current density in 1 M Na_2SO_4 electrolyte.

The effect of current density on the specific capacitance of α-Fe_2O_3 was also studied. Figure 4.12 shows the relationship of specific capacitance of α-Fe_2O_3 nanofibers of different weight percentage with current density. Generally, specific capacitance is observed to reduce with increasing current density regardless of the amount of carbon black added. As with higher current density, fewer ions are able to diffuse to the redox active sites resulting in less charge transfers and storage. Greater proportion of the total charges is then stored on the surface (non faradic double layer storage). On the other hand, at low current density, more charge transfer is able to proceed given the longer

charge/discharge duration. This translates into greater pseudocapacitance which is progressively absent in higher current rate.

4.1.3.3 Investigation of Electrolytes Effect

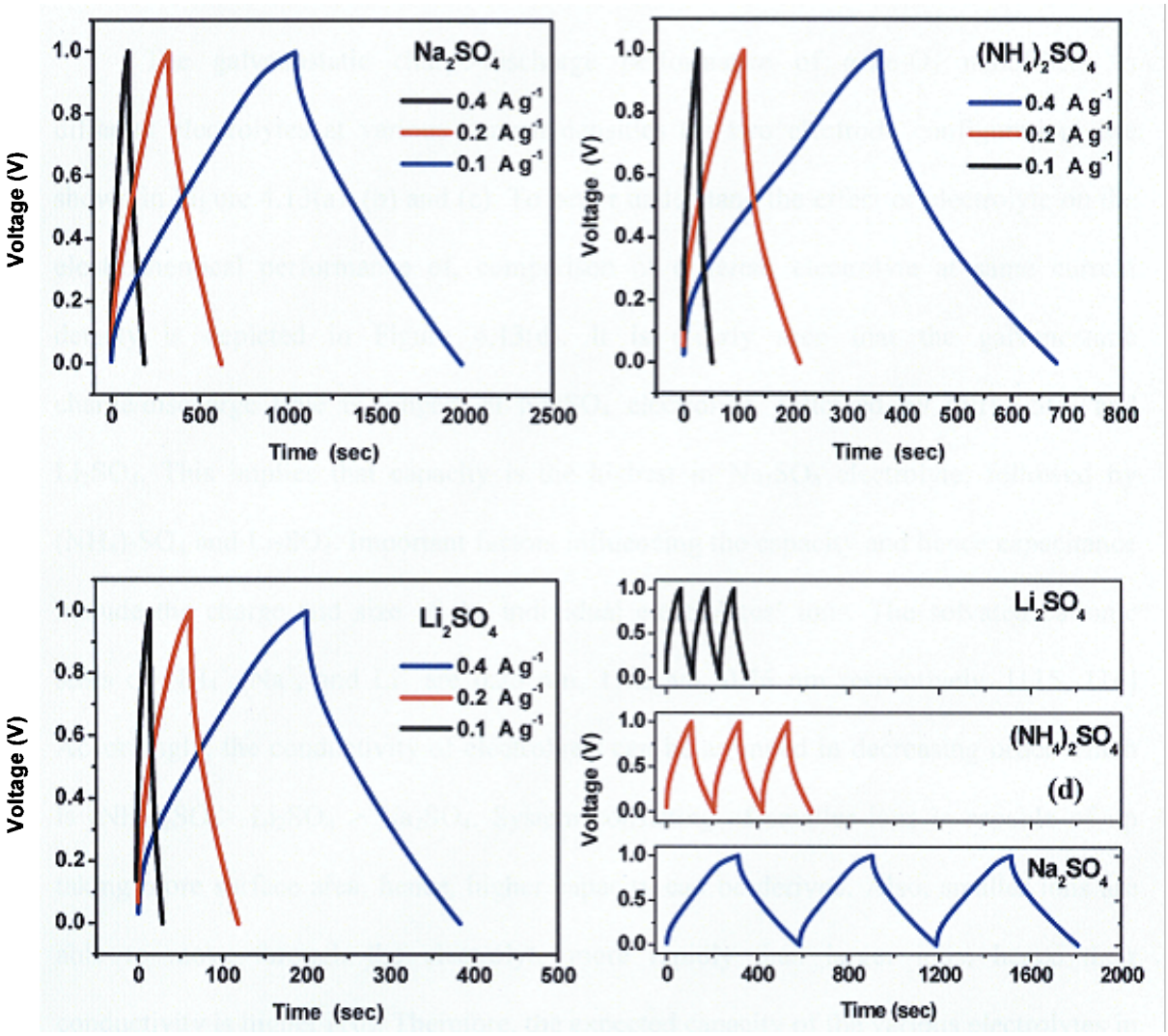

Figure 4.13 : Galvanostatic charge-discharge cycles of the nano-porous α-Fe_2O_3 fibers electrode at different current densities in (a) 1 M Na_2SO_4, (b) 1M $(NH_4)_2SO_4$ and (c) 1 M Li_2SO_4 electrolytes. (d) Galvanostatic charge-discharge cycles of the nano-porous α-Fe_2O_3 fibers electrode at 0.2 A g^{-1}.

To evaluate the electrochemical characteristics of α-Fe_2O_3 nanofibers as electrode materials for supercapacitors, cyclic voltammetry and galvanostatic charge-discharge measurements were employed. The effect of different electrolytes on the electrochemical performance of α-Fe_2O_3 nanofibers was investigated using aqueous 1 M Na_2SO_4, 1M $(NH_4)_2SO_4$ and 1 M Li_2SO_4 as electrolyte.

The galvanostatic charge-discharge performance of α-Fe_2O_3 nanofibers in different electrolytes at various current densities (in two electrode configuration) are shown in Figure 4.13(a), (b) and (c). To better understand the effect of electrolyte on the electrochemical performance of, comparison of different electrolyte at same current density is depicted in Figure 4.13(d). It is clearly seen that the galvanostatic charge/discharge time is longest in Na_2SO_4 electrolyte, followed by $(NH_4)_2SO_4$ and Li_2SO_4. This implies that capacity is the highest in Na_2SO_4 electrolyte, followed by $(NH_4)_2SO_4$ and Li_2SO_4. Important factors influencing the capacity and hence capacitance include the charge and size of the individual electrolytes' ions. The solvated cationic sizes of NH_4^+, Na^+, and Li^+ are 0.25 nm, 1.02 nm, 0.76 nm respectively. [115, 116] Accordingly, the conductivity of electrolytes can be arranged in decreasing order which is $(NH_4)_2SO_4$> Li_2SO_4 > Na_2SO_4. System consisting of smaller ions is capable of up taking more surface area, hence, higher capacity can be derived. Also, smaller ions are able to move through the electrolyte more rapidly than larger ions, hence their conductivity is higher [10]. Therefore, the expected capacity of the various electrolytes in descending order of is $(NH_4)_2SO_4$> Li_2SO_4 > Na_2SO_4. This contradicts with the result

discussed above. To better understand this phenomenal, a three electrode cyclic voltammetry was conducted.

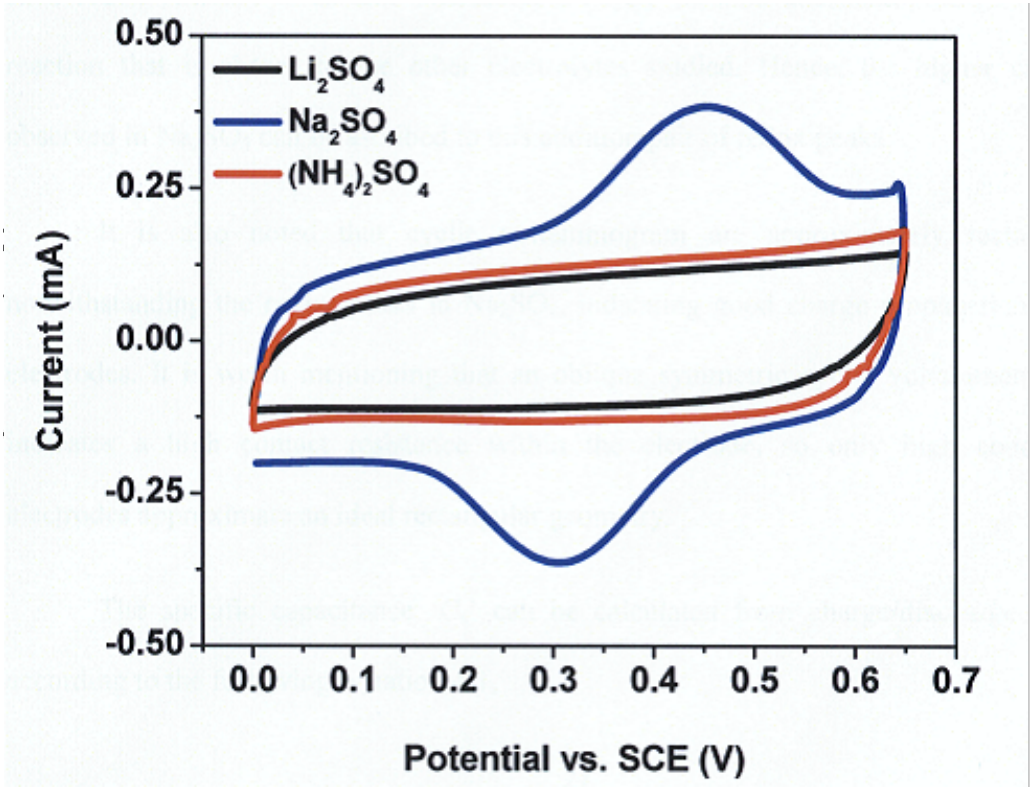

Figure 4.14 : Cyclic voltammogram of the nano-porous α-Fe_2O_3 fibers electrode in 1 M Na_2SO_4, 1M $(NH_4)_2SO_4$ and 1 M Li_2SO_4 electrolyte respectively.

The cyclic voltammogram recorded at the scan rate of 1 mV s^{-1} in three electrode configurations are shown in Figure 4.14. It is clearly seen that an oxidation peak is obtained at +0.45 V vs SCE, coupled with corresponding reduction peak at +0.31V vs SCE in Na_2SO_4 electrolyte. This pair of redox peaks can be assigned to reversible pseudocapacitive behavior originates from the fast faradic reaction at the electrode

surface. In the process, Na^+ cations could have been adsorbed/desorbed to and from the surface of Fe_2O_3. No redox peak is seen in the other two electrolytes which suggest that such redox reaction is absent. Therefore, α-Fe_2O_3 exhibits additional charge transfer reaction that is absent in the other electrolytes studied. Hence, the higher capacity observed in Na_2SO_4 can be ascribed to this addition pair of redox peaks.

It is also noted that cyclic voltammogram are approximately rectangular, notwithstanding the redox peaks in Na_2SO_4, indicating good charge propagation in the electrodes. It is worth mentioning that an oblique symmetric cyclic voltammetry loop indicates a high contact resistance within the electrode, so only high conducting electrodes approximate an ideal rectangular geometry.

The specific capacitance 'C_s' can be calculated from charge/discharge curves according to the following equation 4.1,

$$C_s = \frac{2I}{m\frac{dv}{dt}} \qquad (4.1)$$

Where, C_s is the specific capacitance, I is the applied current, m is the total mass of the active material and dv/dt is the slope of the discharge curve.

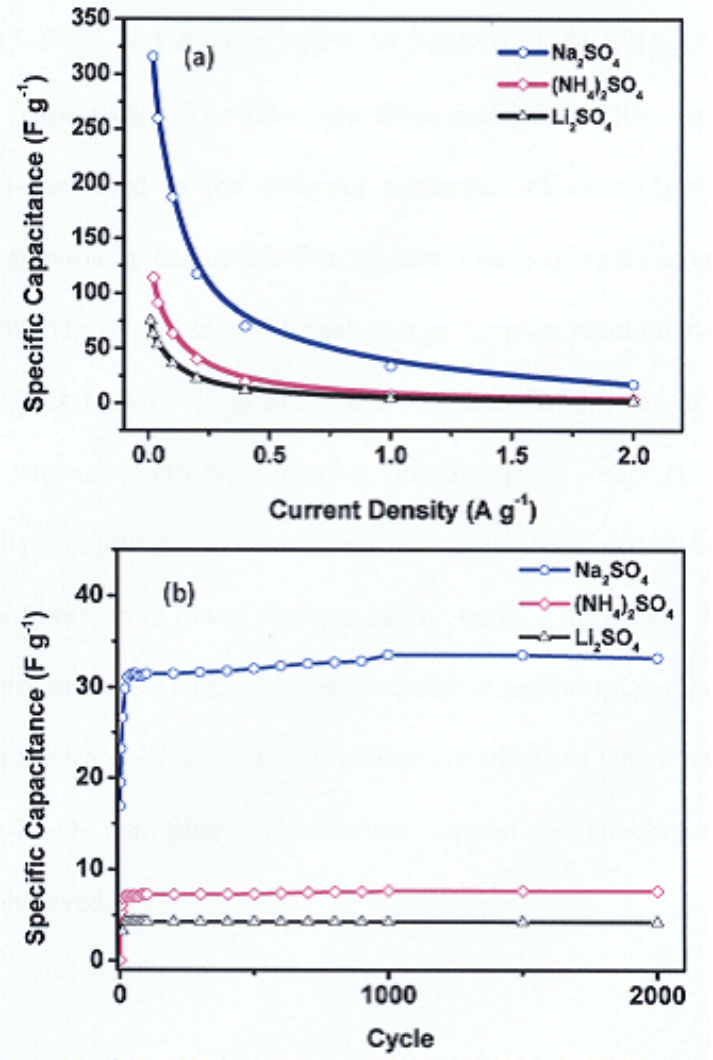

Figure 4.15: (a) Specific capacitance of nano-porous α-Fe_2O_3 fibers at different current density in 1 M Na_2SO_4, 1M $(NH_4)_2SO_4$ and 1 M Li_2SO_4 electrolytes respectively. (b) Cycling behavior of nano-porous α-Fe_2O_3 fibers at different current density in 1 M Na_2SO_4, 1M $(NH_4)_2SO_4$ and 1 M Li_2SO_4 electrolytes respectively.

The values of specific capacitances calculated from galvanostatic discharge curves at different current densities are shown in Figure 4.15. The calculated specific

capacitance values at constant current density of 0.02 A g^{-1} for different electrolytes was 316F g^{-1}, 115 F g^{-1} and 63 F g^{-1} in 1 M Na_2SO_4, 1 M $(NH_4)_2SO_4$ and 1 M Li_2SO_4 electrolytes, respectively. The observed difference of specific capacitance in all three electrolytes is ascribed to the different properties of electrolytes and varying redox mechanisms previously discussed. The highest values of specific capacitance in case of Na_2SO_4 electrolyte is due to additional charge transfer reaction which is absent in the other electrolytes tested. It is also observed that differences in specific capacitance between the various electrolytes in more pronounced at lower current density. At high current density, the ions have lesser time to travel to electroactive sites in the nanoporous α-Fe_2O_3 nanofibers, thus fewer charges can be surface adsorbed. Additionally, the ions are less orderly arranged which further diminish charge storage capacity. Higher density also impedes the transportation of Na^+ cations, resulting in lesser Na^+ adsorption onto the surface of α-Fe_2O_3 nanofibers. This further support the conclusion made on origin of redox peak observed.

4.1.3.4 Effect of Morphology

The surface morphology plays an important role in the characteristics of the pseudocapacitor devices, particularly the ability to store charges. The exposed surface area of the electrode determines the capacity, energy density and power density of the pseudocapacitors. Clearly, materials with higher surface area exhibit greater capacitances and better energy densities consistently.

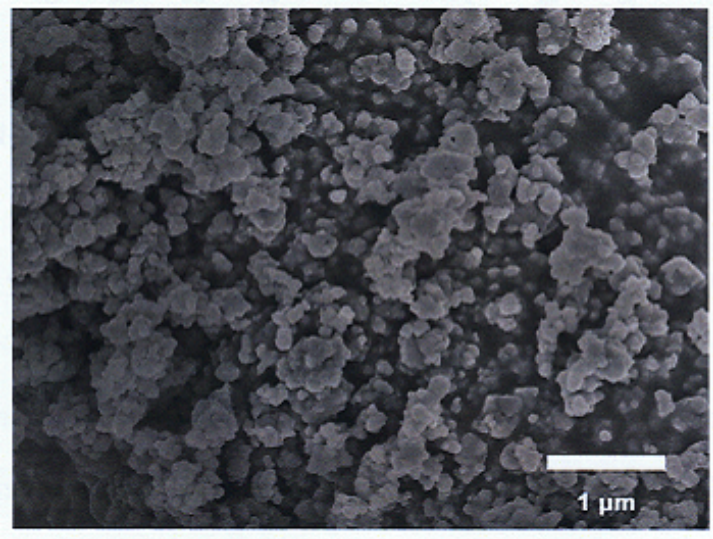

Figure 4.16: FESEM image of Commercial α-Fe_2O_3

Figure 4.16 shows a FESEM image of commercial α-Fe_2O_3 powder. As compared to morphology depicted in Figure 4.8, commercial α-Fe_2O_3 powder contains agglomeration of particles of diverse shapes and sizes. This may results in lower utilization of active sites available for charge transfers.

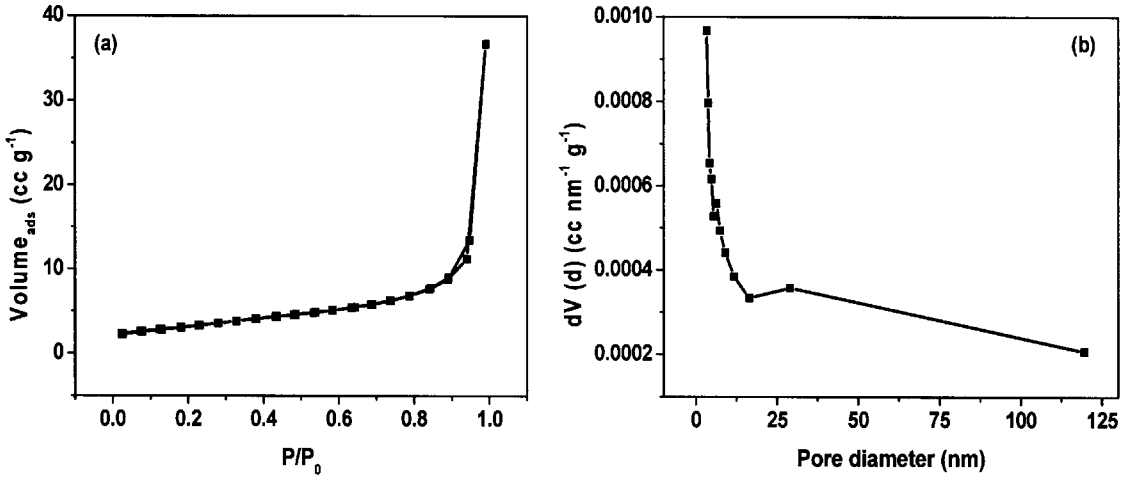

Figure 4.17: (a) Nitrogen adsorption-desorption isotherms of commercial α-Fe_2O_3 at 77 K. (b) Derived BJH plot depicting pores sizes distribution of commercial α-Fe_2O_3.

Figure 4.17 (a) depicts the nitrogen adsorption-desorption isotherms of commercial α-Fe_2O_3 at 77 K and the derived BJH plot. Multipoint Brunauer-Emmett-Teller (BET) analysis performed on α-Fe_2O_3 nanofibers yields a specific surface area of 4.98 $m^2 g^{-1}$. This value is sustainably lower than the BET value obtained for FNF which was 33.95. This may have an impact of the resultant specific capacitance and hence the energy density of the α-Fe_2O_3. Derived BJH from the desorption isotherm is shown in Figure 4.17 (b). It is observed that the BJH analysis did not yield fruitful result on the pore size distribution of the commercial α-Fe_2O_3 powder. The pores size analyzed lies outside the limit of nitrogen adsorption-desorption isotherm. However, it can be concluded that the pore sizes are either less than 3 nm or more than 100 nm or both. Therefore, it is clear that the α-Fe_2O_3 powder is not mesoporous.

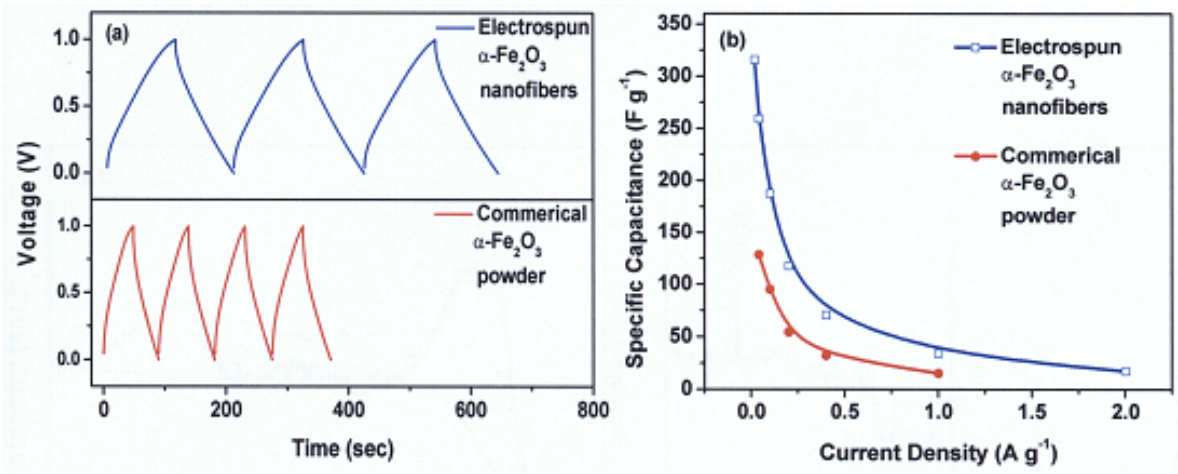

Figure 4.18: (a) Galvanostatic charge-discharge cycles of the α-Fe_2O_3 nanofibers and commercial α-Fe_2O_3 electrode. (b) Plot of specific capacitance with current density.

Figure 4.18(a) depicts the GCD of α-Fe_2O_3 nanofibers and commercial α-Fe_2O_3 powder. Clearly, the electrospun α-Fe_2O_3 nanofibers have exhibited longer charge-discharge time profile at the same current density. The relationship between specific capacitance and current density was also investigated. The specific capacitance 'C_s' can be calculated from charge/discharge curves at various current densities according to equation 4.1. Figure 4.18 (b) shows the relationship of specific capacitance of both α-Fe_2O_3 nanofibers and commercial powder. It is observed that the α-Fe_2O_3 nanofibers have higher specific capacitance than the α-Fe_2O_3 powder which can be ascribed to the smaller particle's size and higher surface area as evident from FESEM images and BET data previously discussed. Also, α-Fe_2O_3 nanofibers being more porous allows better traffic of ions to and from the electrode surface, thereby enabling better utilization of active sites for charge transfer.

4.1.3.5 Charge Storage Mechanism XPS Studies

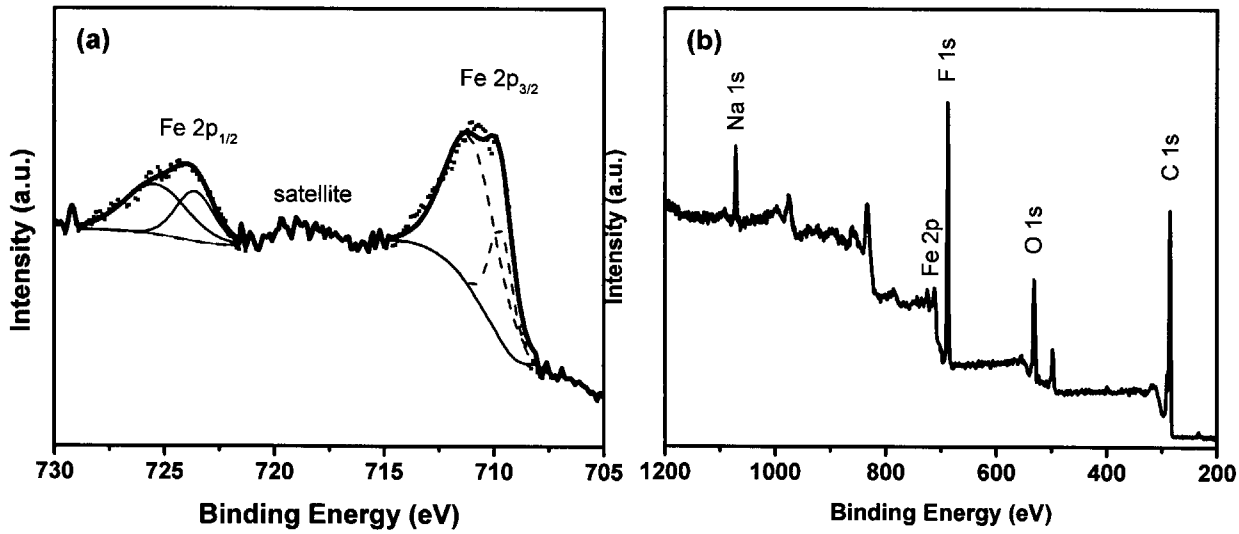

Figure 4.19: (a) high resolution XPS spectra of Fe 2p peaks (b) XPS survey spectra of Fe_2O_3 nanofibers composite.

To better understand the charge storage mechanism, X-ray photoelectron spectroscopy (XPS) was employed. Figure 4.19 shows the XPS spectra of FNF electrodes after charging to 0.6 V and cycling for 1000 cycles. The Fe $2p_{3/2}$ peak is greater than that of Fe $2p_{1/2}$, a result of spin-orbit (j-j) coupling. The main peak of $2p_{3/2}$ is located at 710.7 eV, in agreement with literature [117-119]. An accompanying satellite peak is observed at approximately 8 eV higher than the main Fe $2p_{3/2}$ peak is clearly distinguishable and does not overlap with either the Fe $2p_{1/2}$ or Fe $2p_{3/2}$ peaks [117-119] This indicates the presence of Fe (III) oxidation state. Therefore, the change of oxidation states of FNF during galvanostatic charging and discharging process, an indication of the redox process was not evidenced by XPS analysis. However, additional peaks of Na 1s

were detected in the survey scan of FNF after cycling, as shown in Figure. 4.19 (b), suggesting the intercalation of Na^+ ions into the oxide lattice of Fe_2O_3. This agrees well with the three electrode CV test previously discussed in section 4.1.3.2. It is therefore clear that intercalation of Na^+ ions process rather than redox process contributes significantly to the charge storage mechanism of FNF.

4.1.3.6 Performance of Symmetrical Fe_2O_3 Nanofibers Supercapacitor

To characterize the performance of α-Fe_2O_3 nanofibers as electrode material for energy storage device, energy density and average power density evaluated from galvanostatic charge-discharge curves in a voltage window of 0 to 1 V according to Equation 4.2 and 4.3.

$$E_D = \frac{1}{2} C_D V_D^2 \tag{4.2}$$

$$P_D = \frac{E_D}{t} \tag{4.3}$$

where E_D is the energy density of the device, C_D is the specific capacitance of the device, V is the maximum charging voltage, and t is the time taken to fully discharge.

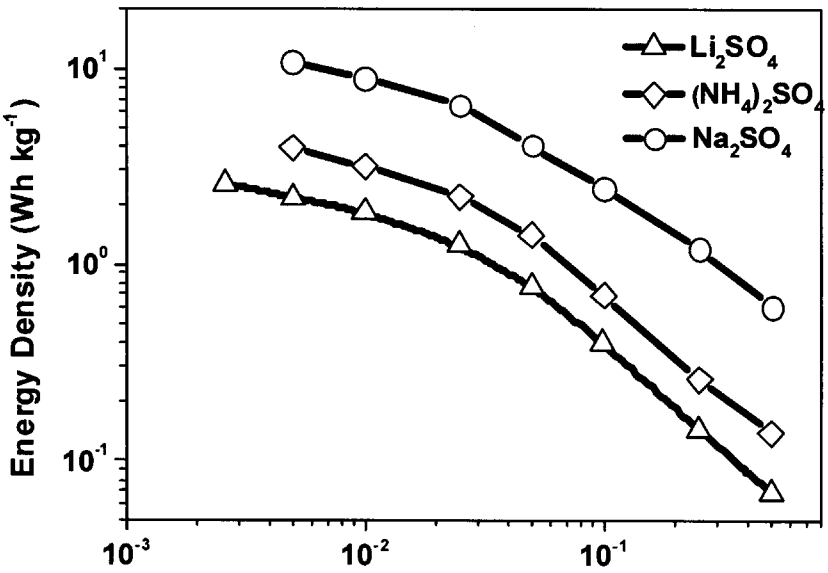

Figure 4.20: Ragone plot for the nano-porous α-Fe_2O_3 fibers electrode in 1 M Na_2SO_4, 1M $(NH_4)_2SO_4$ and 1 M Li_2SO_4 electrolyte respectively.

The energy and power density is summarized as a Ragone plot in Figure 4.20. The α-Fe_2O_3 nanofibers have exhibited both higher power and energy density in Na_2SO_4 electrolyte. This is ascribed to relatively small cationic size of Na^+ and the additional pseudocapacitive behavior of α-Fe_2O_3 in Na_2SO_4 solution previously discussed. The α-Fe_2O_3 nanofibers also have better performance in $(NH_4)_2SO_4$ as compared to Li_2SO_4 solution due to the smaller cationic size of NH_4^+. Highest power density of 0.02 kW/kg and maximum energy density of 9 Wh/kg were achieved in Na_2SO_4 electrolyte.

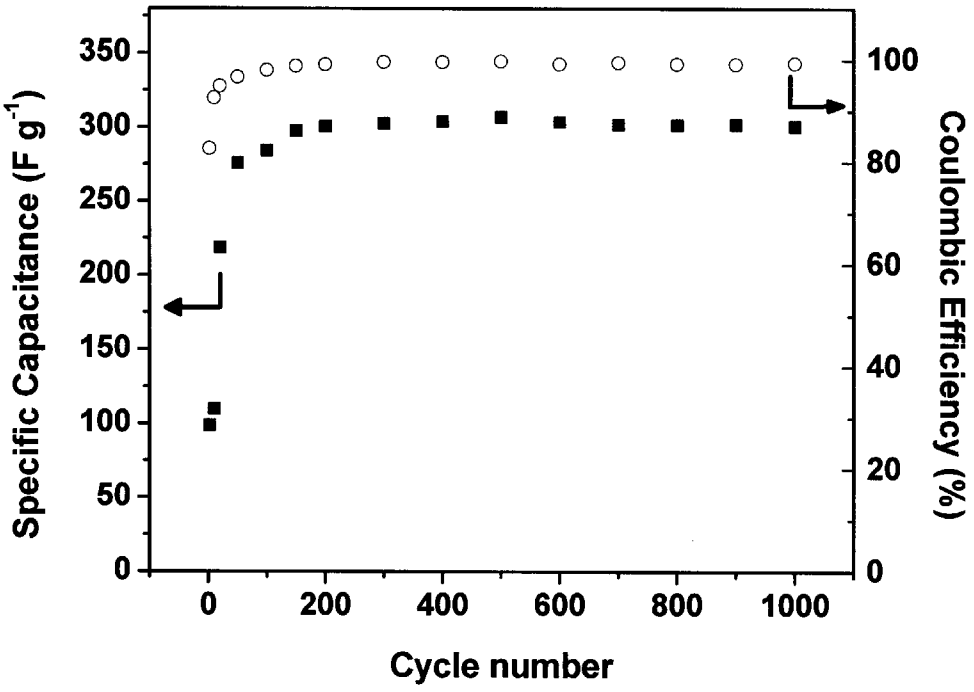

Figure 4.21 : Cyclic performance and coulombic efficiency of the nano-porous α-Fe_2O_3 fibers electrode in 1M Na_2SO_4 at constant current density of 0.02 A g^{-1}.

Long term cycle stability of electrode material is an important factor to consider in for selection of electrode material for in supercapacitor application. The electrochemical stability is examined by galvanostatic charge-discharge cycling at a constant current density of 0.02A g^{-1}. Figure 4.21 shows the cycling performance of Fe_2O_3 nanofibers electrodes in two electrode device configuration. The specific capacitance greatly increases in the first 200 cycles, indicating that the Fe_2O_3 nanofibers were undergoing activation to reach its maximum capacitance. Thereafter, the specific capacitance stabilized around 300 F g^{-1}. The capacitance retention remains as high as 97% at 1000^{th} cycle, indicating that α-Fe_2O_3 nanofibers have good electrochemical stability. The columbic efficiency is also close to 99% during cycling, suggesting that no gas evolution occurred in the voltage region.

4.1.3.7 Electrochemical Impedance Spectroscopy (EIS) Studies

EIS is a useful technique to resolve the charge storage components resulting from different mechanism such as EDL or pseudocapacitance as well as different resistance components such as electrolyte resistance, electrode resistance and interfacial electrode-electrolyte resistance. Hence, EIS is used to investigate the electrochemical behavior. The Nyquist plots for FNF supercapacitor device before and after cycling were recorded and are shown in Figure 4.22.

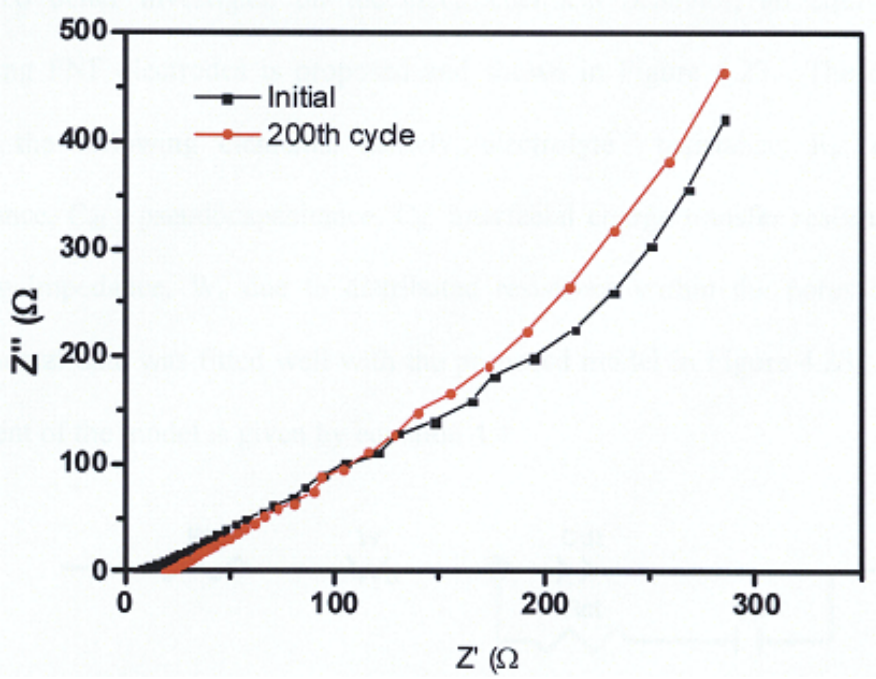

Figure 4.22: Nyquist plot of α-Fe_2O_3 nanofibers symmetrical device setup before and after cycling.

An intersection observed at the real axis in the high frequency region, followed by a non-vertical slope in low frequency region. This can be explained by two reasons: (1) an interface exists between the electrode and the electrolyte, and (2) a double-layer capacitance connects in parallel with a resistance and leads to the formation of a RC loop [120]. The transformation of the plot to a vertical line takes place at low frequency can be mainly ascribed to the capacitive response of porous carbons. The presence of the non-vertical slope at the low frequency region of the Nyquist plot may be associated with low electronic conductivity of the electrode and different pore size distribution of the carbons [120].

To better investigate on the electrochemical behavior, an equivalent circuit simulating FNF electrodes is proposed and shown in Figure 4.23. The circuit would involve the following elements, namely, electrolyte resistance, R_b; double layer capacitance, C_{dl} ; pseudocapacitance, C_p; interfacial charge transfer resistance, R_{ct}; and Warburg impedance, W_o due to distributed resistance within the pores of FNF. The experimental data was fitted well with the proposed model in Figure 4.23. The equation equivalent of the model is given by equation 4.4.

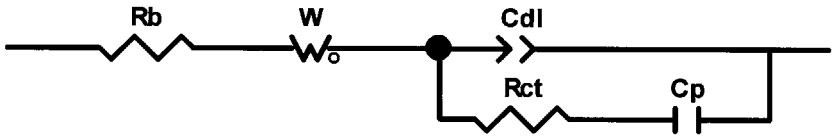

Figure 4.23: Equivalent circuit model for α-Fe_2O_3 nanofibers symmetrical device setup.

$$Z = R_s + \left(\frac{1}{(j\omega)^{\alpha} C_{dl}} + \frac{1}{R_{ct} + (j\omega C_{pc})^{-1}} \right)^{-1} + R_w \frac{\text{ctnh}\ (jW_T\omega)^{W_P}}{(jW_T\omega)^{W_P}} \qquad (4.4)$$

where R_s is the electrode resistance, C_{dl}, ω and α are the capacitance of the distributive system, the angular frequency, an exponent that determines the deviation of the capacitance from ideality due to a distribution of relaxations, R_W, W_T, are the diffusion resistances, related to both the diffusion length and the diffusion coefficient, and W_P, the exponent that measures its deviation from ideality, j is $\sqrt{-1}$.

By fitting equation 4.4 to the respective impedance data depicted in Figure 4.22, the values shown in Table 4-1 have been evaluated.

Table 4-1: Components of the equivalent circuit fitted for the impedance spectra of α-Fe_2O_3 nanofibers symmetrical device setup in Figure 4.22.

Cycle	$R_s(\Omega)$	$C_{dl}(mF\ cm^{-2})$	$R_{ct}(\Omega)$	$C_p(mF\ cm^{-2})$	$R_w(\Omega)$
Initial	3.69	21.86	1.162	12.93	225.2
200th	3.49	10.14	21.97	219.75	1360

Equation 4.4 in the case here can be simply categorized into three frequency regions. The real axis intersection at the sufficiently high frequency provides the electrolyte resistance, while the mid high frequency informs about the charge transfer resistance. And the low frequency region encompasses most or all the electrochemical activities.

The electrolyte resistance of the electrodes is negligible, indicating that the electrochemical properties of bulk electrolytes remain stable. Both greater charge transfer resistance R_{ct} and higher pseudocapacitance C_p are obtained after undergoing galvanostatically charged and discharged for 200 cycles. This indicates a greater amount of faradic current, a result of more charge transfer reactions taking place. This agrees with the explanation discussing that FNF electrodes have undergone an activation process which enables better accessibility of electrolyte ions to its pores.

4.1.4 V_2O_5 Nanofibers Supercapacitors

Vanadium oxides have been investigated for their potential use in energy storage applications, particularly for lithium ion batteries, due to the availability of multiple oxidation states [121]. Herein, V_2O_5 nanofibers are synthesized via electrospinning route and characterized.

4.1.4.1 Physical Characterization of V_2O_5 Nanofibers

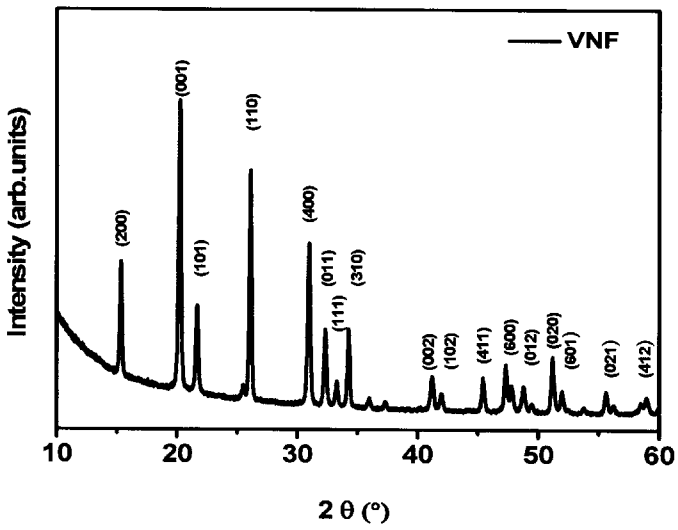

Figure 4.24: XRD patterns of electrospun VNF annealed at 470 °C for 30 min in the range of 2θ from 10 to 60°. Reproduced by permission of ECS - The Electrochemical Society.

Figure 4.24 illustrates typical X-ray diffraction (XRD) patterns of electrospun VNF after annealing at 470 °C for 30 min. The XRD pattern of VNF revealed highly intense reflections that corresponded to orthorhombic Shcherbinaite structure with $Pmn2_1$ space group (JCPDS card no. 41-1426). Lattice parameters of VNF calculated from

Rietveld crystal structure refinement was found to be a = 11.513 (2) Å, b = 3.5656 (2) Å and c = 4.3727 (3) Å.

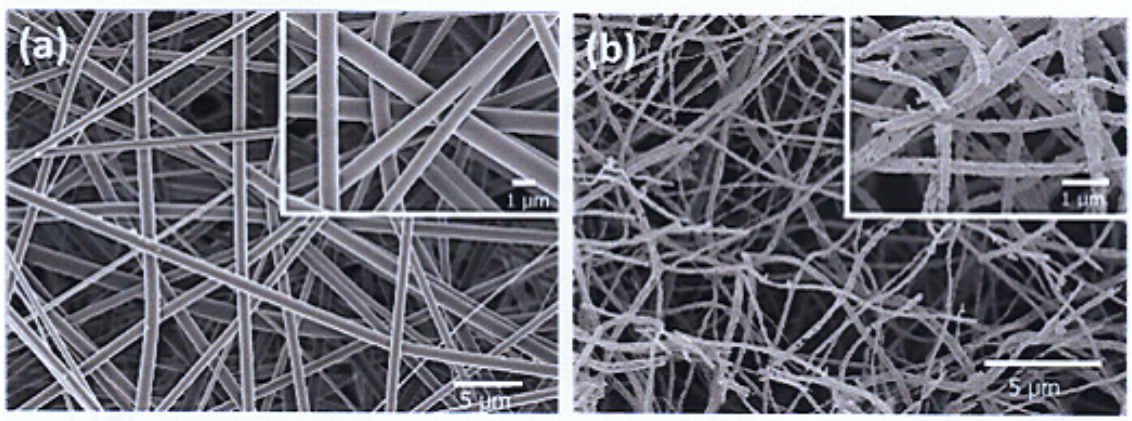

Figure 4.25: : (a) FE-SEM images of electrospun VNF, (b) Electrospun VNF annealed at 470 °C for 30 min.

Field emission scanning electron microscopic (FE-SEM) images of as-spun VNF shown in Figure 4.25(a) (with the inset showing the magnified view of the respective images) revealed smooth surface of the fibers with diameters ranging from 300 to 500 nm and fiber length over 200 µm. As spun VNF were annealed at various temperatures between 300 and 500 °C to remove the polymer and to crystallize V_2O_5 nanocrystals in the VNF. Heating at higher temperature (> 500 °C) leads to destruction of the fibrous structure, while at lower temperature (300-400°C) resulted in incomplete removal of PVP polymer. The fibers heat treated at optimum temperature around 470 °C retained the fibrous morphology with well-defined crystalline structure. Figure 4.23(b) illustrates the VNF after annealing at 470 °C for 30 minutes. The annealed VNF exhibited a more spiral

like structure, with diameter of 300-500 nm, lower than that of as spun VNF. This change in fibrous morphology is mainly attributed to the decomposition of PVP polymer during sintering. Vaporization of the polymer during this process left behind pores and the surface seems to have a spiral like morphology, which allows facile movement of electrolyte during the electrochemical reaction. It is worth noting that, sintering of as spun VNF was conducted at relatively low temperature (~470 °C) to achieve a high performance V_2O_5 electrode.

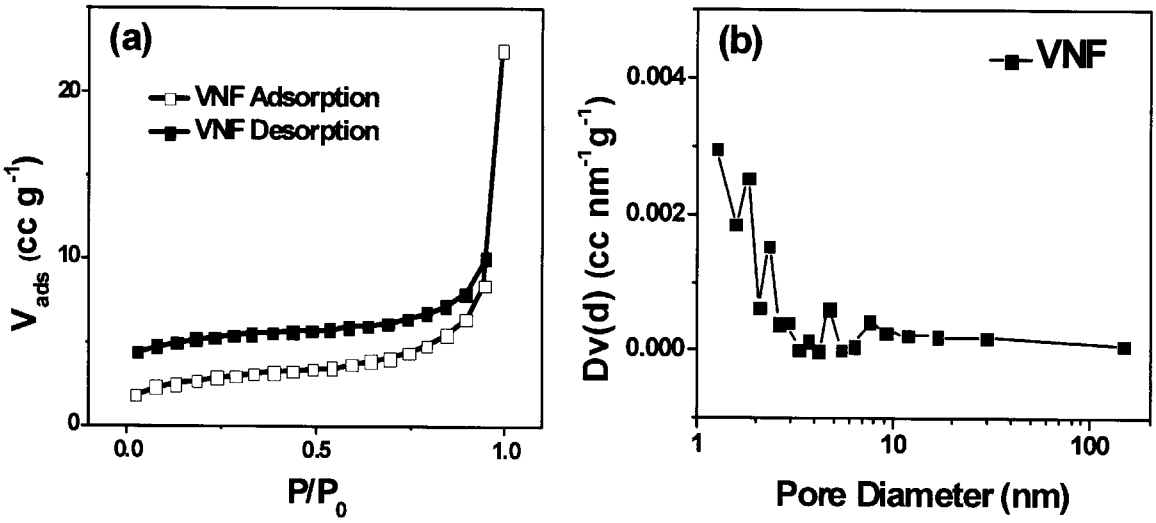

Figure 4.26: (a) Nitrogen adsorption-desorption isotherms of VNF at 77 K. (b) BJH plot depicting pores sizes distribution of VNF.

The nitrogen adsorption/desorption isotherms of both VNF at 77 K presented in Figure 4.26 (a) exhibited type II isotherm (according to IUPACS classification [122]) with type H3 hysteresis showing absence of limiting adsorption at high relative pressure

for both adsorption and desorption isotherm. Hysteresis loop extending down to low pressure region was observed indicating the presence of micropores which is advantageous for double layer charge storage. Desorption isotherm of PANF shows hysteresis loop at the relative pressure of 0.8–0.9, suggesting meso-porosity (high surface area) which is beneficial for the movement of ions throughout the nanofibers. The gradual increase in adsorption curves of both VNF in the middle relative pressure region can be attributed to multi–layer adsorption of nitrogen in the mesopores and macropores. The leap (plunge) close to the saturation pressure in adsorption (desorption) isotherm suggests pores filling of large mesopores and macropores which is favourable as they allow ions to amass in the proximity of electrode permitting high power capability.

Brunauer-Emmett-Teller (BET) analysis [123] of the isotherms yields specific surface area of 9.5 $m^2 g^{-1}$ for VNF. The obtained values are consistent with the previous reports on such material (VNF: 10 $m^2 g^{-1}$) [92, 124]. To investigate the pore size distribution, Barrett-Joyner-Halenda (BJH) analysis was applied on the desorption isotherms [125]. Figure 4.24 (b) depicts the pore volume distribution curves obtained by BJH analysis. Much of the surface area can be attributed to pores from the micropores range (<2 nm, IUPAC classification) [126]. These micropores are readily accessible to the hydrated K^+ (0.3 nm) and Cl^- (0.3 nm) ions and would certainly enhance both the electrical double layer and pseudocapacitive contribution of the nanofibers [115].

4.1.4.2 Chemical Characterization of V_2O_5 Nanofibers

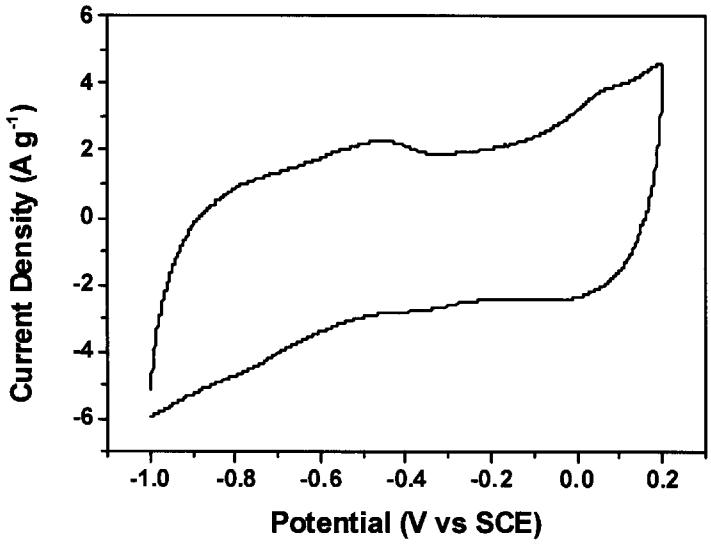

Figure 4.27: Three electrode cyclic voltammograms of VNF at 10 mV s^{-1} *vs.* SCE.

Three electrodes setup was utilized to study the electrochemical stability of VNF electrodes, in which platinum sheet and standard calomel electrode (SCE) were used as counter and reference electrodes, respectively. Figure 4.27 shows the three electrode CV curve of VNF electrode. The CV curve of VNF electrode shows good stability under positive and negative polarization with reversibility from 0.2 –1 V *vs.* SCE. These results illustrate that VNF is a potential candidate for negative electrode.

4.1.4.3 Charge Storage Mechanism XPS Studies

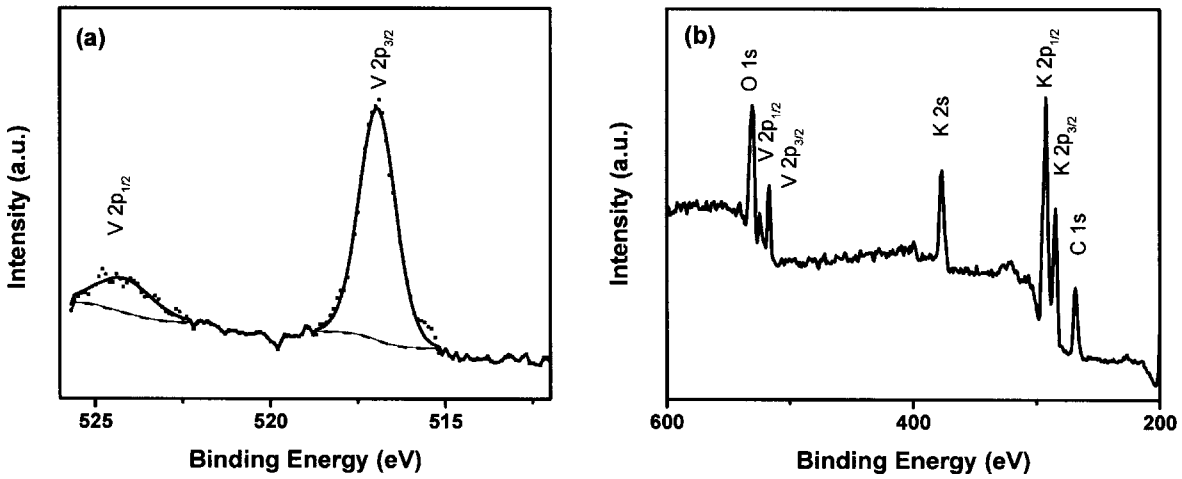

Figure 4.28: (a) high resolution XPS spectra of V 2p peaks (b) XPS survey spectra of V_2O_5 nanofibers composite.

Figure 4.28(a) shows the high resolution XPS spectra of VNF electrodes after charging to 0.9 V and cycling for 1000 cycles. The spin–orbit splitting obtained for V $2p_{3/2}$ and V $2p_{1/2}$ is 7.75 eV, confirming the existence of V (5+) oxidation state and hence, the presence of V_2O_5 [127] This suggests that the change in oxidation states of VNF during galvanostatic charging and discharging process, an indication of the redox process was not evidenced by XPS analysis. However, additional peaks of K 2s, K $2p_{1/2}$ and K $2p_{3/2}$ were detected in the survey scan of VNF after cycling, as shown in Fig. 4.28 (b), which suggest the intercalation of K^+ ions into the oxide lattice of V_2O_5. It is therefore clear that intercalation of K^+ ions process rather than redox process contributes significantly to the charge storage mechanism of VNF.

4.1.4.4 Performance of Symmetrical V_2O_5 Nanofibers Supercapacitor

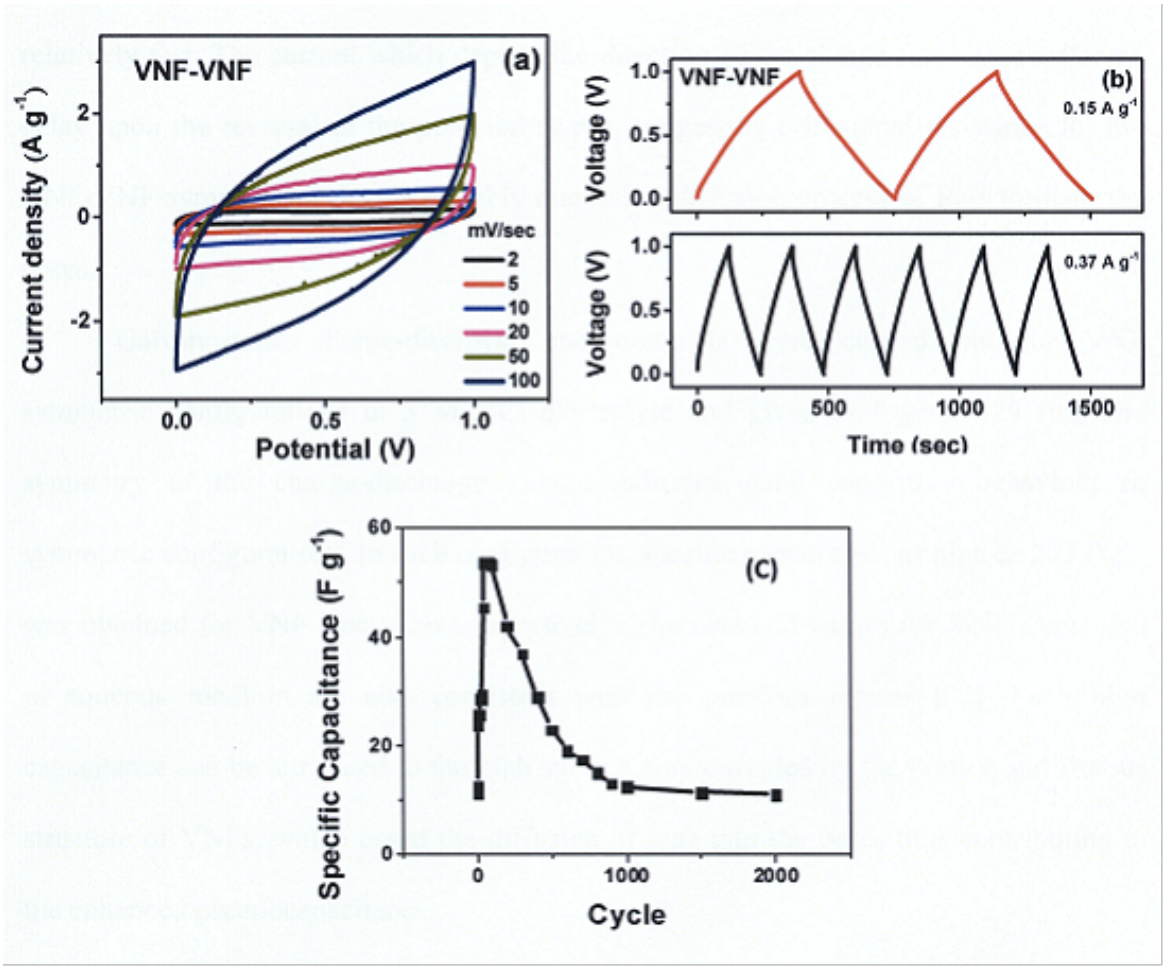

Figure 4.29: (a) CV curves for annealed electrodes measured at various scan rates in 3 M KCl in two-electrode symmetric configurations. (b) Galvanostatic charge-discharge curves for annealed VNF electrodes measured at various current densities under the same conditions. (c) Cycling behavior of VNF-VNF cell. Reproduced by permission of ECS-The Electrochemical Society.

Cyclic voltammetry (CV) and galvanostatic charge-discharge studies have been employed to evaluate the supercapacitive behaviour of electrospun VNF in symmetric device configuration. Figure 4.29 (a) illustrates the CV traces of VNF-VNF symmetric

device as a function of scan rate with respect to its current density in 3 M KCl aqueous solution. It can be observed that charging and discharging processes in VNF electrode are relatively fast. The current which depicts the direction of the charge flow, showed some delay upon the reversal of the potential sweep, suggesting diffusional resistance for the VNF-VNF symmetrical device possibly due to the diffusion process of ions through the pores.

Galvanostatic charge-discharge measurements were carried out for VNF symmetric configurations in 3 M KCl electrolyte and given in Figure 4.29 (b). The symmetry of the charge-discharge curves indicates good capacitive behaviour in symmetric configurations. In such configuration, specific capacitance as high as 213 F g^{-1} was obtained for VNF electrodes, respectively. The obtained values for VNF electrodes in aqueous medium are also consistent with the previous reports [92]. Such high capacitance can be attributed to the high surface area provided by the porous and fibrous structure of VNFs, which eased the diffusion of ions into the pores thus contributing to the enhanced pseudocapacitance.

4.1.5 Polyaniline Nanofibers Supercapacitors

Electrically conducting polymers make good pseudocapacitive material for electrode of supercapacitors. They possess good electronic conductivity, have low cost, and adjustable redox activity through chemical modification.[37, 38] They are capable of pseudocapacitive storage through the redox process. Ions are transferred to the polymer backbone when oxidation occurs and vice versa. The processes have good reversibility as the redox reactions do not alter the structures.[39]

Pseudocapacitors employing electronically conducting polymer such as polyaniline [40, 46, 128, 129] , polypyrrole [38, 40, 43, 45] and poly(3,4-ethylenedioxythiophene) (PEDOT) [49, 130] derivatives have been reported. Different methods used to fabricate polyaniline nanofibers include electrospinning [86], hard templates, soft template, interfacial polymerization [18], and rapid polymerization [131]. In particular, interfacial polymerization and rapid polymerization have achieved more attention due to its easiness, large-scale production-ability and environmentally benign nature. Furthermore, it has a capability to produce high-quality polyaniline nanofibers with control of their morphology, size and diameter [18]. Herein, rapid chemical polymerization route is used to synthesize polyaniline nanofibers. Also, the performance of symmetrical PANF was characterized which will serve as a comparison for asymmetrical device employing PANF electrode in later section.

4.1.5.1 Physical Characterization of Polyaniline Nanofibers

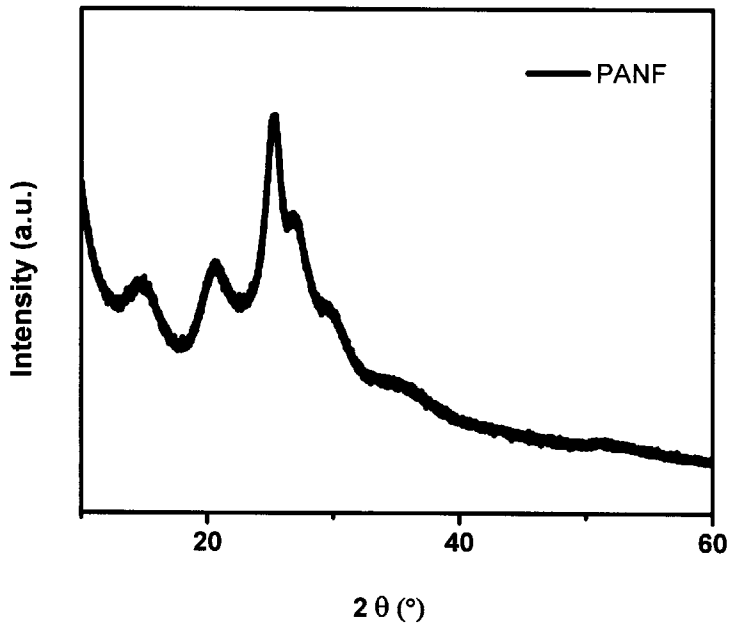

Figure 4.30: XRD patterns of PANF and electrospun VNF annealed at 470 °C for 30 min in the range of 2θ from 10 to 60°. Reproduced by permission of ECS- The Electrochemical Society.

Figure 4.30 illustrates typical X-ray diffraction (XRD) patterns of electrospun VNF after The XRD pattern of PANF revealed several broad reflection peaks (2θ) at 15°, 20.6°, 25.2° and, 26.8° which confirms the formation of polyaniline by rapid polymerization procedure. These reflections indicate the presence of crystalline order in the bulk PANF samples, which is consistent with literature [132].

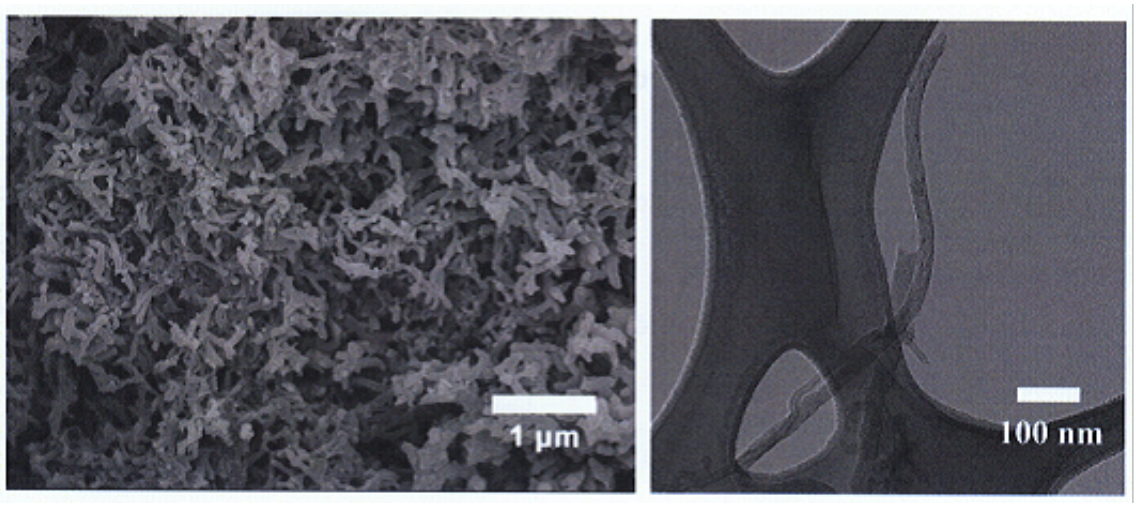

Figure 4.31: (a) FESEM image of PANF by rapid chemical polymerization.(b) TEM image of a single PANF. Reproduced by permission of ECS - The Electrochemical Society.

Figure 4.31 displays the morphological features of the PANF, showing interwoven structure with shorter fibers compared to electrospun VNF. The PANF fiber length and diameter PANF estimated from FE-SEM images with length of *ca.* 100-600 nm and diameter ranging from 30-200 nm. Transmission electron microscopy (TEM) was conducted to study the morphology of PANF (inset Figure 4.31) clearly depicts nanostructured smooth surface of PANI.

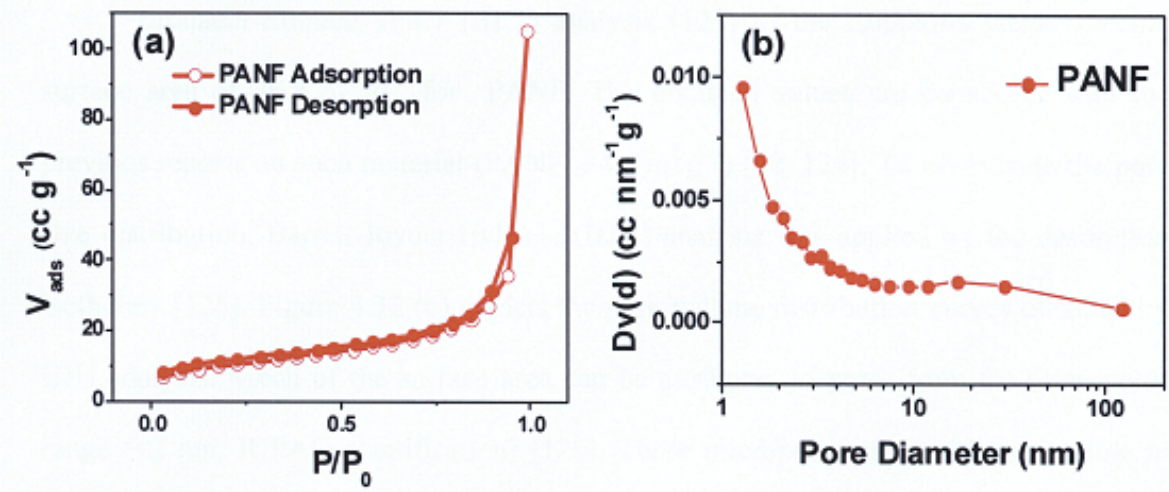

Figure 4.32: (a) Nitrogen adsorption-desorption isotherms of PANF at 77 K. (b) BJH plot depicting pores sizes distribution of PANF. Reproduced by permission of ECS - The Electrochemical Society.

The nitrogen adsorption/desorption isotherms of both PANF at 77 K presented in Figure 4.32 (a) exhibited type II isotherm (according to IUPACS classification [122]) with type H3 hysteresis showing absence of limiting adsorption at high relative pressure for both adsorption and desorption isotherm. Hysteresis loop extending down to low pressure region was observed indicating the presence of micropores which is advantageous for double layer charge storage. Desorption isotherm of PANF shows hysteresis loop at the relative pressure of 0.8–0.9, suggesting micro-porosity (high surface area) which is beneficial for the movement of ions throughout the nanofibers. The gradual increase in adsorption curves of PANF in the middle relative pressure region can be attributed to multi–layer adsorption of nitrogen in the macropores. The leap (plunge) close to the saturation pressure in adsorption (desorption) isotherm suggests pores filling of large macropores which is favourable as they allow ions to amass in the proximity of

electrode permitting high power capability.

Brunauer-Emmett-Teller (BET) analysis [123] of the isotherms yields specific surface area of 36.8 m^2 g^{-1} for PANF. The obtained values are consistent with the previous reports on such material (PANF: 34.4 $m^2 g^{-1}$) [92, 124]. To investigate the pore size distribution, Barrett-Joyner-Halenda (BJH) analysis was applied on the desorption isotherms [125]. Figure 4.32 (b) depicts the pore volume distribution curves obtained by BJH analysis. Much of the surface area can be attributed to pores from the micropores range (<2 nm, IUPAC classification) [126]. These micropores are readily accessible to the hydrated K^+ (0.3 nm) and Cl^- (0.3 nm) ions and would certainly enhance both the electrical double layer and pseudocapacitive contribution of the nanofibers [115].

4.1.5.2 Chemical Characterization of Polyaniline Nanofibers

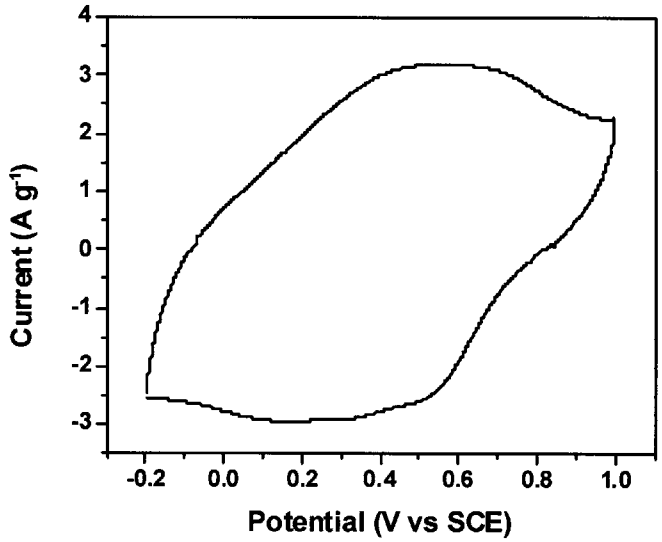

Figure 4.33: Three electrode cyclic voltammograms of PANF at 10 mV s^{-1} *vs.* SCE.

A three electrode electrochemical cell setup was also utilized to study the electrochemical stability of PANF electrodes, in which platinum sheet and standard calomel electrode (SCE) were used as counter and reference electrodes, respectively. To use it as a possible candidate in an asymmetrical supercapacitor, we tested PANF in 3 M KCl. It is worthy to mention that PANF works better in H_2SO_4 [133], however such acid media is not suitable for VNF nor FNF. Figure 4.30 shows the three electrode CV curve of PANF electrode. The CV curve of PANF electrode shows good stability under positive and negative polarization with reversibility from 0.2 –1 V *vs.* SCE. These results illustrate that PANF is a good candidate for positive electrode.

4.1.5.3 Performance of Symmetrical Polyaniline Nanofibers Supercapacitor

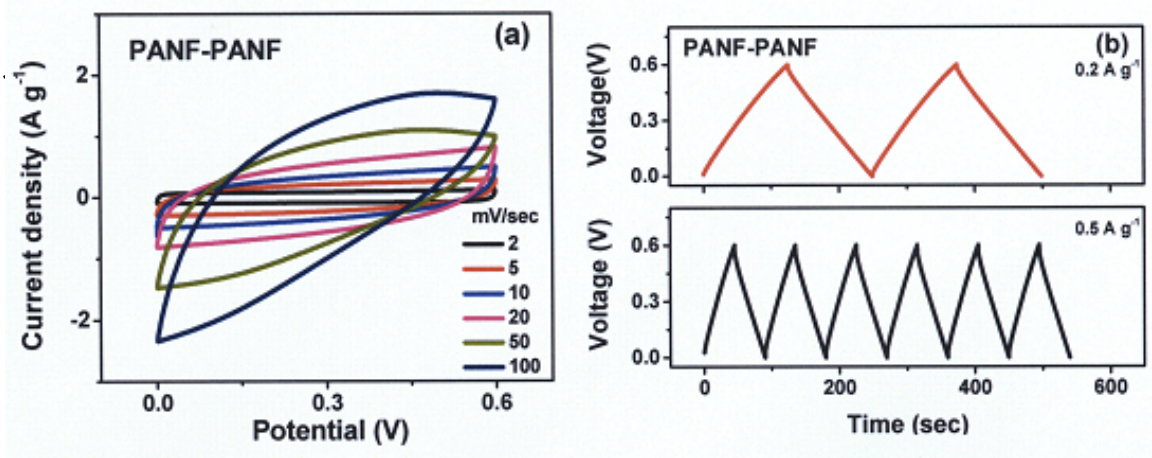

Figure 4.34: (a) CV curves for PANF electrodes measured at various scan rates in 3 M KCl in two-electrode symmetric configurations. (b) Galvanostatic charge-discharge curves for PANF electrodes measured at various current densities. Reproduced by permission of ECS - The Electrochemical Society.

Galvanostatic charge-discharge measurements were carried out for PANF-PANF symmetric configurations in 3 M KCl electrolyte and given in Figure 4.34 (a) and (b). The symmetry of the charge-discharge curves indicates good capacitive behaviour in symmetric configurations. In such configurations the specific capacitance as high as 176 F g^{-1} was obtained for PANF electrodes. The obtained values for PANF electrodes in aqueous medium are also consistent with the previous reports [129, 134]. The high capacitance can be attributed to the high surface area provided by the porous and fibrous structure of PANFs, which eased the diffusion of ions into the pores thus contributing to the enhanced pseudocapacitance. A relatively lower specific capacitance obtained for PANF electrodes as compared to those in acidic media like H_2SO_4 could be attributed to the absence of reversible doping process of PANFs which usually occurred in acidic media [133].

4.2 Asymmetrical Supercapacitors

Pseudocapacitor electrodes based on either electronically conducting polymers (ECP) (polyaniline (PANI) [128, 129], poly(3,4-ethylenedioxythiophene) (PEDOT) [130], and polypyrrole (PPy) [38]) or transition metal oxides (TMO) [135] RuO_2 [58, 136], NiO_x [137], Co_3O_4 [138] and V_2O_5 [92, 139] have been extensively investigated as electrode materials for supercapacitor applications [140]. Pseudocapacitor based electrodes often provide higher specific capacitance as the charge storage redox mechanism involves the entire electrode active mass as compared to EDLC carbon electrodes wherein primarily only the electrode surface contributes to the specific capacitance via double layer charge formation.

Energy density of supercapacitor is proportional to square of voltage ($E=½CV^2$), where C is the specific capacitance (Fg^{-1}) and V is the voltage window (Volts). In aqueous electrolytes, both EDLC and pseudocapacitors have lower working voltages (<1.2 V) which severely discounts their energy density. Although pseudocapacitors exhibit higher specific capacitance and hence greater energy density, such increment is often inadequate and cyclability is also questionable.

One approach to further increase the energy density is to widen the working voltage (~2-3 V) of both EDLC and pseudocapacitor through adoption of organic-based (such as acetonitrile) electrolytes instead of aqueous solutions [3]. However, such aprotic organic solvents not only entail detrimental costs from fabrication processes requiring water free environment, but also possesses safety and toxicity issues. Another approach

to increase the working voltage is to construct an asymmetric supercapacitor (ASC) in an aqueous medium by employing two different kinds of electrodes. Employing electrodes of different nature in ASC for positive and negative polarization allows both electrodes to operate in an optimal voltage range [94, 135, 141-144]. It has been reported that ASC consisted of TMO-AC[68, 82, 135, 145] or ECP-AC[9, 146] pair is capable of relatively higher operating voltage.

Among the transition metal oxides, amorphous hydrous ruthenium oxide ($RuO_2.xH_2O$) exhibits pseudocapacitve behaviour with large specific capacitance, but it is too expensive for the commercialization. V_2O_5 is one of the attractive candidates because of its layered structure, multiple oxidation states of vanadium which allows surface/bulk redox reactions leading to high capacitance in symmetric supercapacitor configuration [92]. Among the conducting polymers, polyaniline (PANI) is considered as a promising electrode materials for supercapacitors owing to its environmental stability, controllable electrical conductivity multiple intrinsic redox states and excellent processability [147].

Nanostructured active materials are capable of providing higher power density than bulk counterparts owing to shorter diffusion pathways, increased accessible surface area leading to facile flow of ions at the electrode/electrolyte interface. Electrospinning is a simple, low cost scalable facile route for making high aspect ratio 1D nanofibers with controllable diameter using electrostatic force [148]. Also, electrospinning often results in highly porous interconnected three dimensional fibrous electrode that provides both a continuous conduction pathway and increased electrode/electrolyte contact surface [149]. Such attributes are crucial to determine the performance of supercapacitors.

As aforementioned, we have successfully synthesized and fabricated symmetrical supercapacitors from CNT, FNF, PANF and VNF. Their three electrode performance was also characterized and discussed.

Herein, we have constructed an ASC based on a combination of nanostructured TMO and ECP to study the capacitive properties and widen the operating voltage in aqueous medium. In the present work, an attempt has been made to construct an ASC comprising of electrospun vanadium pentoxide nanofibers (VNF) as negative electrode and polyaniline nanofibers (PANF) as positive electrodes in aqueous medium [108]. A schematic illustration of the ASC utilizing electrospun VNF and PANF is shown in Figure 4.36. The structure, surface morphology and diameter of the electrospun fibers was controlled by varying the parameters like applied potential, precursor concentration, viscosity and flow rate of the solution. The detailed electrochemical studies of both VNF and PANF electrodes are conducted and analyzed in both symmetric and asymmetric configurations and described in detail.

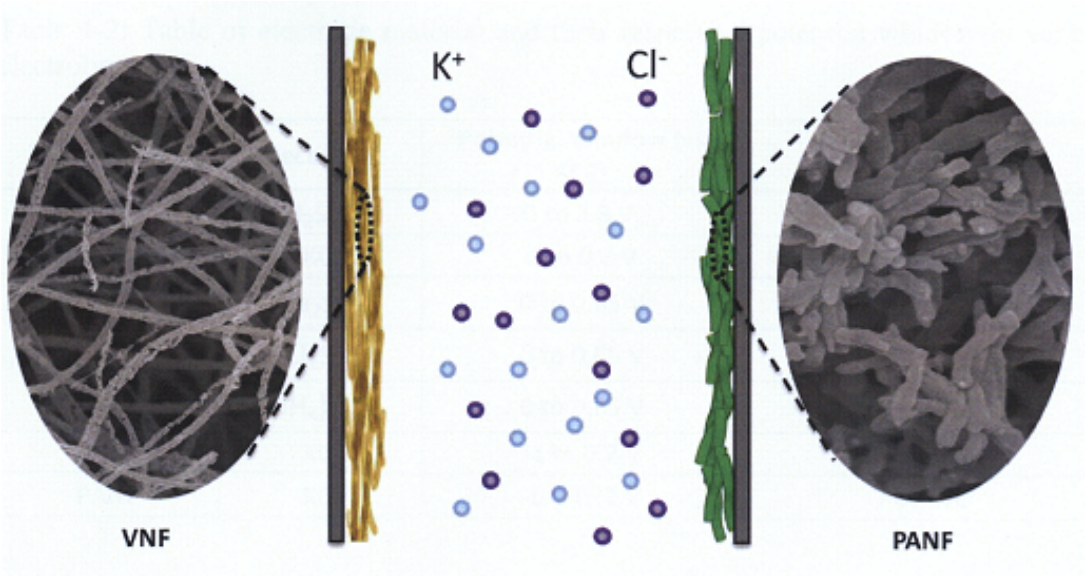

Figure 4.35 : Schematic illustration of an asymmetrical supercapacitor comprising of VNF and PANF as positive and negative electrodes, respectively. Reproduced by permission of ECS - The Electrochemical Society.

In order to fabricate VNF and PANF electrodes in asymmetric configuration (ASC), a common aqueous electrolyte needs to be utilized. Three electrodes setup was utilized to study the electrochemical stability of individual electrodes, in which platinum sheet and standard calomel electrode (SCE) were used as counter and reference electrodes, respectively. A table summarizing the respective electrode materials, electrolytes and their corresponding electrochemical window is depicted in Table 4-2.

Table 4-2: Table of electrode material and their respective potential window in various electrolytes.

Electrode Material	Electrolyte	Potential Window (vs SCE)	Potential Electrode Candidate
P3-CNT	H_2SO_4	0 to 0.8 V	Positive or Negative
	KCl	0 to 0.8 V	Positive or Negative
FNF	Na_2SO_4	0 to 0.65 V	Positive
	Li_2SO_4	0 to 0.65 V	Positive
	$(NH_4)_2SO_4$	0 to 0.65 V	Positive
VNF	KCl	-1 to 0.2 V	Negative
PANF	KCl	-0.2 to 1 V	Positive

From Table 4-2, it would be a good choice to assemble an asymmetrical supercapacitor using VNF and PANF as the negative and positive electrode, respectively. Although PANF results in higher capacitance in aqueous electrolyte like H_2SO_4 [140], VNF readily dissolved in such acidic media. Hence, KCl was chosen as the optimum electrolyte after several failed electrochemical trials of VNF-PANF in various aqueous electrolytes including H_2SO_4 and NaOH.

4.2.1 Electrochemical Characterization of Asymmetrical Supercapacitor

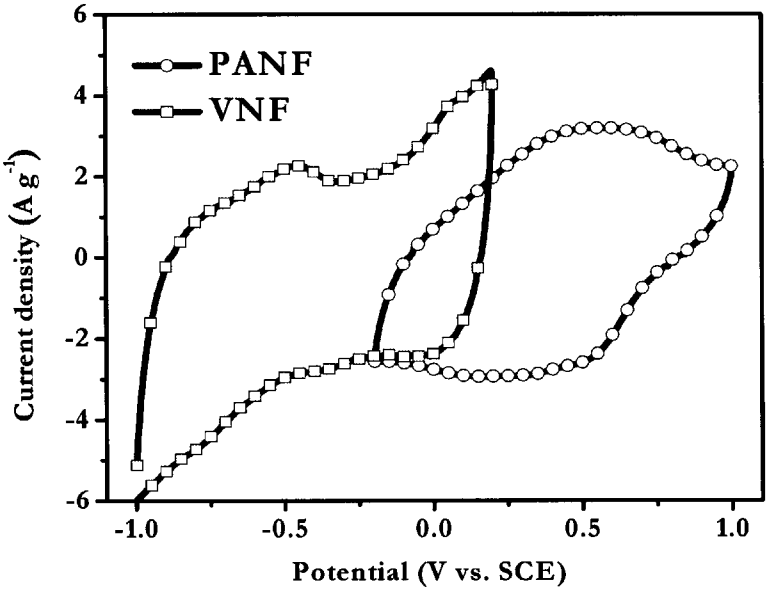

Figure 4.36: Three electrode cyclic voltammograms VNF and PANF at 10 mV s^{-1} *vs.* SCE. Reproduced by permission of ECS - The Electrochemical Society.

Figure 4.36 shows the three-electrode CV of both VNF and PANF extracted from Figures 4.27 and 4.33. These CV curves reveal that PANF electrode exhibited high electrochemical stability under positive polarization, giving a high electrochemical reversibility up to +1 V *vs.* SCE, whereas VNF electrode shows stability under negative polarization with reversibility of –1 V *vs.* SCE. These results illustrate that VNF is more stable being a negative electrode, while PANF is more stable as a positive electrode. Hence, a working voltage window of 2 V (E_{PANF}- E_{VNF} = 1.0 V-[-1.0 V] = 2 V) is viable if the two materials are judiciously paired in an asymmetric system with 3 M KCl as the

common electrolyte. Generally, the aqueous system is stable up to ~1.23 V and said potential electrolysis takes place. However, in the asymmetric combination provides wider operating potential up to 2 V. This extension of the working potential in the aqueous medium is mainly due to the combination of the high hydrogen overpotential offered by VNF under negative polarization together with high oxygen overpotential when PANF is used as positive electrode [145].

Another factor to be considered is the optimization of desired capacity of such asymmetric configuration which is crucial to achieve high energy density. It is important to note that in a symmetric configuration, the applied voltage is split equally between the two electrodes. However, in asymmetric system where the two electrodes are different the voltage will be split depending on the capacitance of individual electrode material. The capacitance of each electrode is related to the respective mass and intrinsic pseudocapacitance. Mass balances between the two electrodes are needed to optimize the cell voltage of the asymmetric capacitor. The capacity balance will enlist the conservation of charges (i.e. $q^+ = q^-$) and can be obtained via the following equation,

$$\frac{m_+}{m_-} = \frac{C_- \times \Delta E_-}{C_+ \times \Delta E_+} \tag{4.7}$$

where m_+, m_-, C_+, C_-, ΔE_+, and ΔE_- are the respective mass, specific capacitance and potential windows of three electrodes configuration of the individual positive and

negative electrode. Optimization of the mass ratio was done based on Equation 4.4 to be 1.2:1 for PANF : VNF.

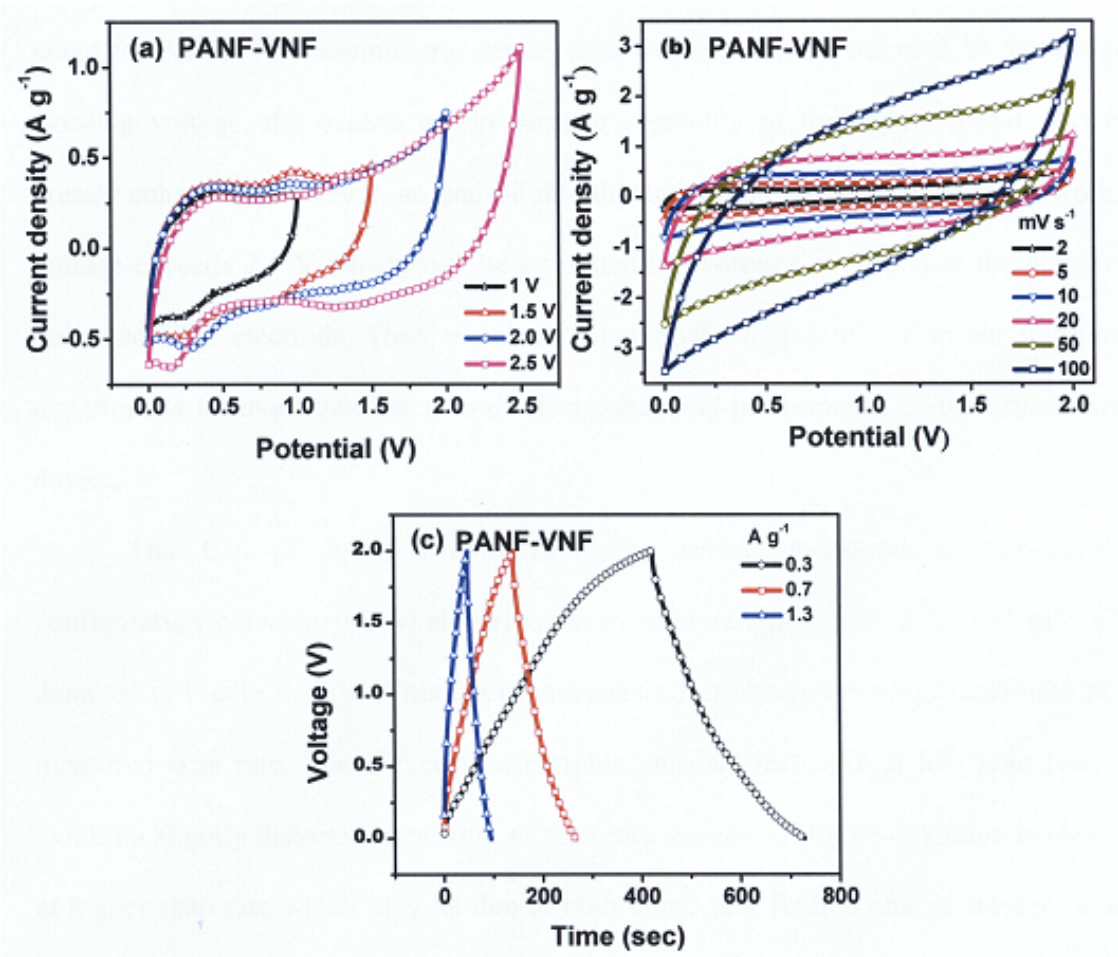

Figure 4.37 : (a) Cyclic voltammograms (CV) of two-electrode cell of VNF and PANF at 10 mV s^{-1} in the presence of 3 M KCl electrolyte solution with different operating potentials (b) CV traces of an asymmetrical PANF-VNF device measured between 0-2 V at various scan rates ranging from 2-100 mV s^{-1}. (c) Galvanostatic charge-discharge curves of an asymmetrical PANF-VNF device measured between 0-2 V at various current densities. Reproduced by permission of ECS - The Electrochemical Society.

Figure 4.37(a) shows the CV curves of VNF-PANF asymmetric device in two electrode configuration measured at different potential windows as shown in the figure at 10 mV s^{-1}. In an aqueous medium, a CV curve of less oblique rectangular geometry is noted for PANF-VNF asymmetric device with working voltage below 2 V. With higher working voltage, the overall energy storage capability of the asymmetrical device is greatly enhanced. However, an undesirable drastic current surge is observed if working voltage exceeds 2.5 V which may be attributed to hydrogen evolution at the negatively polarized VNF electrode. Thus, we chose a potential window of 2 V in our subsequent experiments to investigate the overall electrochemical performance of the asymmetrical device.

The CV of PANF-VNF asymmetric device, measured in two-electrode configuration between 0-2 V at various scan rates ranging from 2 to 100 mV s^{-1} is depicted in Figure 4.37(b). This figure indicates a fast charge/discharge capability at the measured scan rate. The CV curves resemble an ideal rectangle at low scan rate, and exhibit a slightly distorted trapezium as scan rate increases. Higher deviation is observed at higher scan rate which may be due to both kinetically limited charge storage process and the resistivity of the electrode, which will be verified by EIS measurement in later section. It is worth mentioning that the specific capacitance was calculated based on the total mass of active material instead of that of a single electrode. A device capacitance of 41 F g^{-1} is obtained at 5 mV s^{-1} which is slightly lower capacitance than VNF-VNF and PANF-PANF symmetric configurations. However, such asymmetrical configuration enables a working voltage up to 2 V, thereby enhancing energy density according to

Equation 4.2.

Galvanostatic charge-discharge studies were conducted for VNF-PANF asymmetric device with different current densities. Figure 4.37(c) depicts the typical charge-discharge curves of a PANF-VNF asymmetric supercapacitor. The symmetrical charging and discharging characteristics indicates good capacitive behaviour of ASC.

4.2.2 Comparison of Symmetrical and Asymmetrical Configuration on Supercapacitor Performance

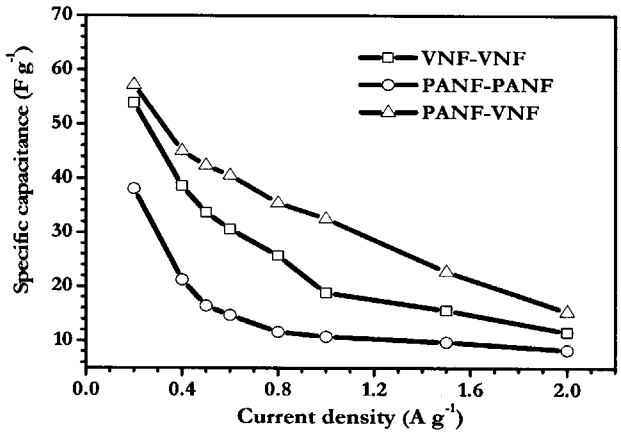

Figure 4.38: Plot of specific capacitance *vs.* current density. Reproduced by permission of ECS - The Electrochemical Society.

Figure 4.38 summaries the specific capacitance calculated from galvanostatic charge-discharge curves for both symmetric (VNF-VNF and PANF-PANF) and asymmetric configuration (VNF-PANF). For symmetrical configuration, galvanostatic values are extracted from Figures 4.29 and 4.34, while for asymmetrical configuration,

values are extracted from Figure 4.37. In general, the specific capacitance gradually decreases with higher current density due to a larger IR drop at high current density. Decrease in specific capacitances values were observed with increasing current density. As charge/discharge rate increases, fewer ions are able to diffuse into the sub-surface resulting in less numbers of redox reactions, which leads to reduced charge storage. Nevertheless, the promising results from both CV and galvanostatic charge-discharge measurements of VNF-PANF asymmetric system indicates a higher working voltage, good pseudocapacitive properties.

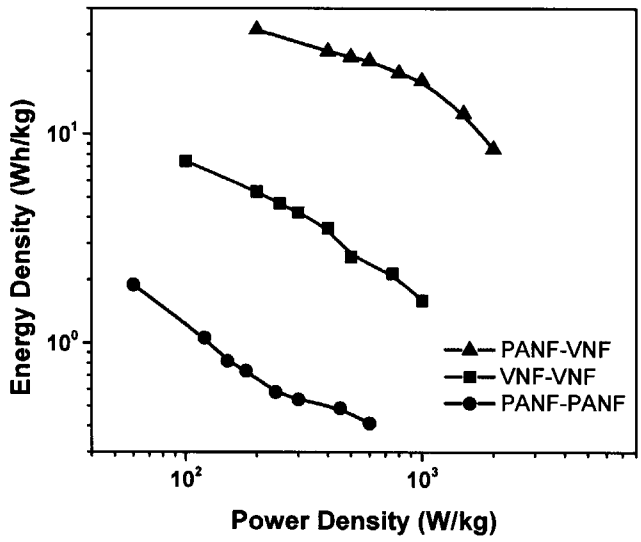

Figure 4.39: A Ragone plot of symmetrical and asymmetrical devices.

Energy and power densities are used to characterize the performance of energy storage devices. To demonstrate the electrochemical performance of our device, energy discharged and average power densities were evaluated from galvanostatic charge-discharge curves according to Equations (4.2) and (4.3).

Figure 4.39 shows the Ragone plot of both symmetrical and asymmetrical devices. VNF-PANF supercapacitor exhibited much higher energy and power density than its symmetrical configuration counterparts. This is ascribed to the synergistic effect endowed by the combination of PANF and VNF namely; (1) the nanostructure of both PANF and VNF that facilitates diffusion of electrolyte ions and enables higher capacitance; (2) the asymmetrical configuration that widens the operating potential window thus enabling redox process from different oxidations states of vanadium.

4.2.3 Effect of Morphology on Asymmetrical Supercapacitor

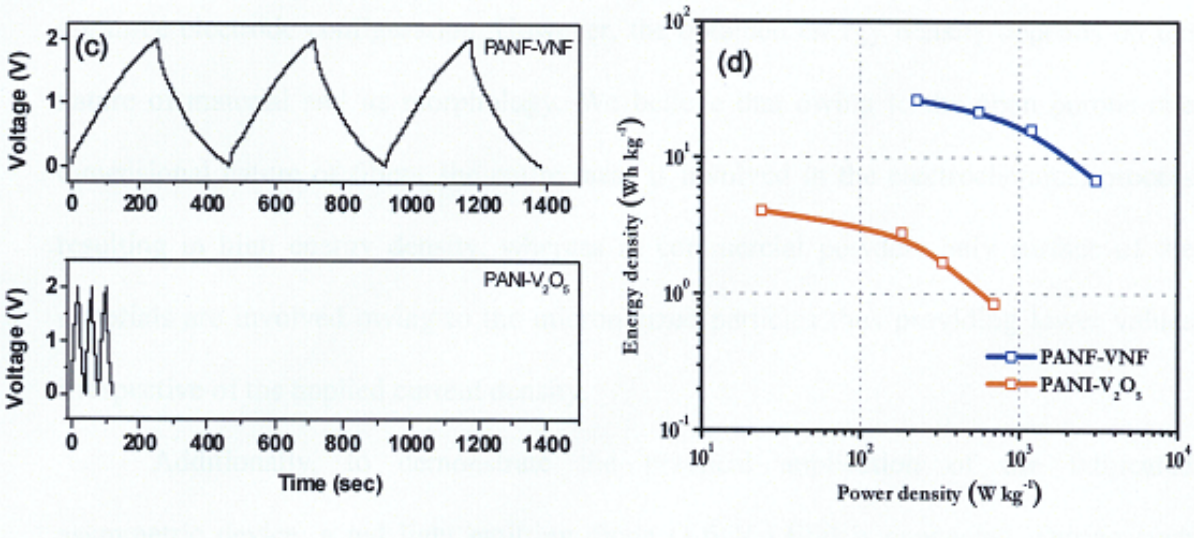

Figure 4.40 : (a) FESEM image of Polyaniline [136], (b) FESEM image Commercial V_2O_5 powder (Sigma-Aldrich), (c) Galvanostatic charge-discharge curves for PANF-VNF and PANI-V_2O_5 electrodes measured at same current density of 0.1 A g^{-1}. (d) Performance comparison of nanostructured fibers ASC with commercial micron sized particles counterpart. Reproduced by permission of ECS - The Electrochemical Society.

Figure 4.40 depicts the FESEM image polyaniline, commercial V_2O_5 (Sigma-Aldrich) and a Ragone plot of ASC constituted of nanofibers with commercial powder of V_2O_5 and PANI [150]. Nanostructured ASC exhibited higher power and energy densities when compared to their conventional commercial counterparts. This is owing to the better utilization of the active material in the nanostructured ASC [133]. Moreover, nanostructure morphology can facilitate the diffusion of electrolyte ions, while the intrinsic high electroactive surface area enables larger electrode/electrolyte interface thus

leading to higher specific capacitance. In addition, the optimization process for the fabrication of electrodes by mass loading based on the specific capacitance obtained in the three electrode configuration. However, the obtained energy density depends on the nature of material and its morphology. We believe that owing to the open porous one dimensional nature of fibers, the entire mass is involved in the electrochemical process resulting in high energy density, whereas in commercial powders only surface of the materials are involved owing to the micron sized particles thus providing lower values irrespective of the applied current density.

Additionally, to demonstrate the practical application of the fabricated asymmetric device, a red light emitting diode (1.6 V LED) is connected. During such testing, the asymmetrical device is galvanostatically charged at low current rate and discharged via LED, the lighting of LED is shown in Figure 4.41. Tandem cells of asymmetrical devices can be employed to increase the working voltage to the required level.

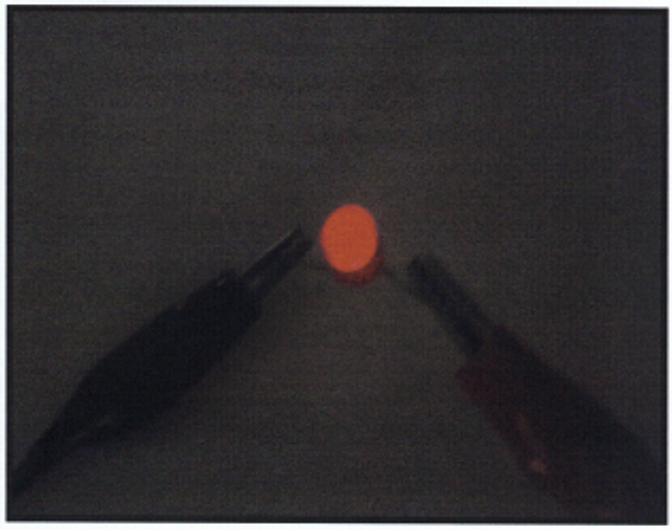

Figure 4.41: Photo image of red LED connected in series with asymmetrical device.

4.2.4 Cycling Performance of Asymmetrical Supercapacitor

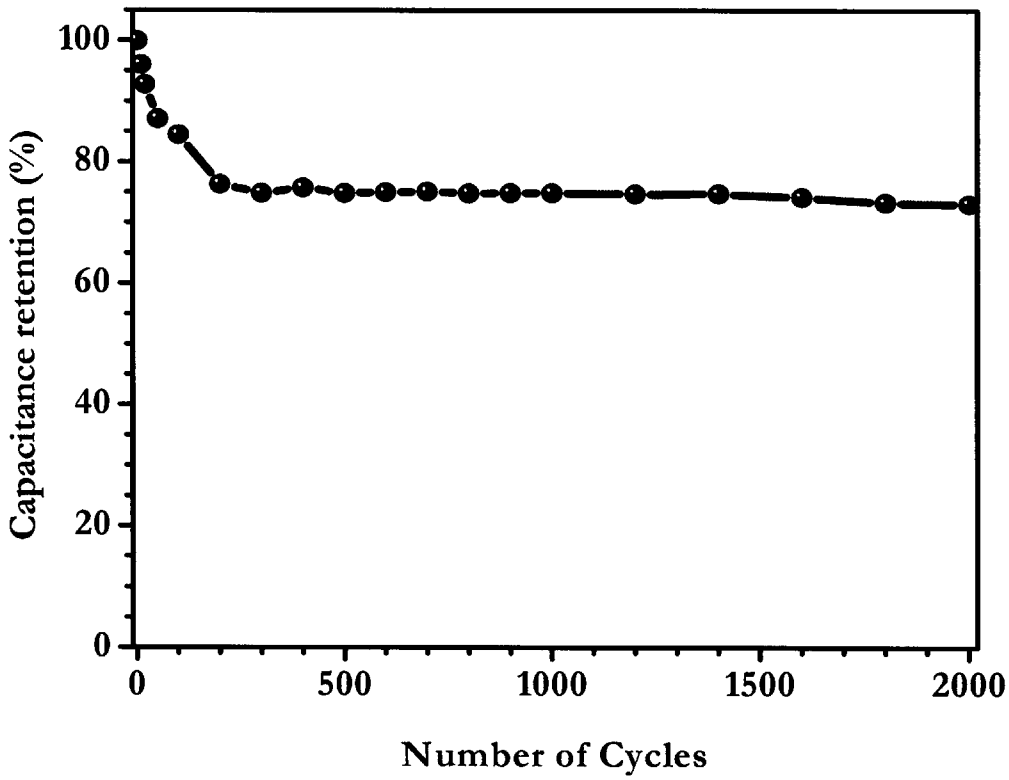

Figure 4.42 : Cycle performance of asymmetrical device with a voltage of 2 V at scan rate of 5 mV s^{-1}. Reproduced by permission of ECS - The Electrochemical Society.

Long cycling life is also another important requirement for supercapacitors especially for pseudocapacitors wherein faradic redox process are involved. Figure 4.42 shows the capacity retention of the asymmetrical capacitor cycled at 5 mV s^{-1} up to 2 V. Capacity of device is normalized with respect to the first discharge capacitance. The asymmetric device displayed an initial specific capacitance of 42.7 F g^{-1} with good cycling stability up to 2000 cycles, with capacity remaining at ~73% at 2000th cycle.

Supercapacitors are fundamentally expected to have long cycle life as energy is stored physically via electrical double layer formation. Whereas in the case of pseudocapacitor, cycle life is often limited by the parasitic chemical reactions and mechanical breakdown of structures due to swelling of electrode materials, both of which will be more pronounced at higher voltage. Here, the initial capacity degradation can be ascribed to the stabilization of the crystal structure. Minor fading was observed once the structure was stabilized (after 150 cycles) during electrochemical cycling. High energy density of 21.7 Wh kg^{-1} is still maintained despite the fade. This finding shed new insights on coupling conducting polymer and nanostructured transition metal oxides to attain high energy density storage devices through careful selection of electrode materials and morphology tuning.

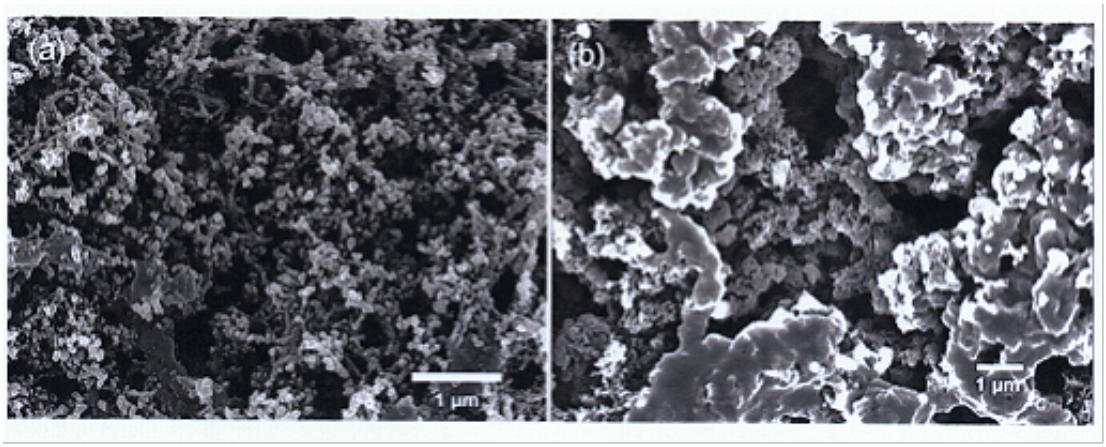

Figure 4.43: FESEM images of (a) V_2O_5 nanofibers, (b) polyaniline nanofibers after cycling for 1000 cycles. Reproduced by permission of ECS - The Electrochemical Society.

Figure 4.43 shows the FESEM images of (a) V_2O_5 nanofibers, (b) polyaniline nanofibers after cycling for 1000 cycles. In comparison to the FESEM images of VNF and PANF depicted in Figure 4.25 and Figure 4.31, respectively, it is clear that the fibrous structures had collapsed after cycling. These observations explain the fading cycling performance previously discussed. A crumbled structure impedes the traffic of ions to and from the electrode materials. Also, less electronic charges can be harvested as more particles are being electrically isolated. All these result in lower active sites utilization and less charge capacity, hence lower capacitance and energy density are observed.

4.2.5 Electrochemical Impedance Studies of Asymmetrical Supercapacitor

To investigate electrochemical performance, such as their frequency dependence and equivalent series resistance (ESR) of the symmetrical and asymmetrical supercapacitors, EIS measurements were carried out in the frequency range 10 kHz to 10 mHz at an alternating current (AC) amplitude of 10 mV. Figure 4.44 illustrates the Nyquist impedance spectra of both VNF and PANF electrodes in symmetrical and asymmetrical configurations in aqueous electrolyte, respectively.

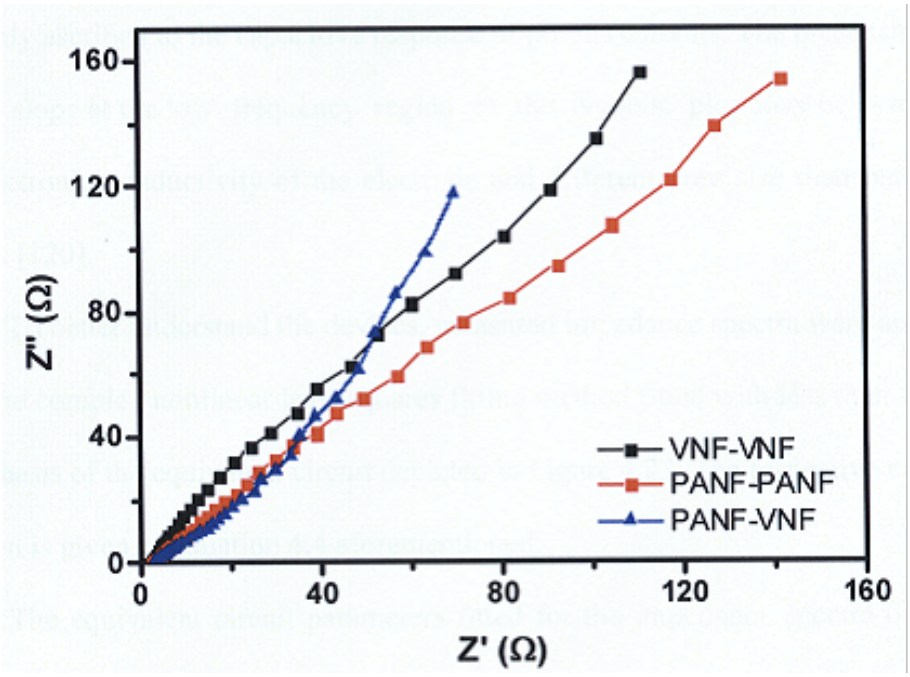

Figure 4.44: Nyquist plot of symmetrical and asymmetrical devices at open circuit conditions. Reproduced by permission of ECS - The Electrochemical Society.

At sufficiently high frequencies, intersection with the real axis (Z') provides the value of the ESR (R_e) and the diameter of semicircle reveals the charge transfer resistance (R_{ct}) of electrode, which arises from diffusion of ions at the PANF-VNF electrode/electrolyte interface. The Nyquist impedance spectra in Figure 4.44 consists of a minor high frequency arc and a low frequency spike showing an inclination at an angle 45° indicating that the both VNF and PANF electrodes has good pseudocapacitive (combined contribution of both electrical double layer capacitance and faradic pseudocapacitance) characteristics [92].

The transformation of the plot to a vertical line takes place at low frequency can be mainly ascribed to the capacitive response of porous carbons. The presence of the non-vertical slope at the low frequency region of the Nyquist plot may be associated with low electronic conductivity of the electrode and different pore size distribution of the carbons [120].

To better understand the devices, measured impedance spectra were analyzed using the complex nonlinear least squares fitting method fitted with less than 10% error on the basis of the equivalent circuit depicted in Figure 4.23 .The respective circuit equation is given in equation 4.4 aforementioned.

The equivalent circuit parameters fitted for the impedance spectra of symmetric device configuration with VNF-VNF and PANF-PANF electrodes and asymmetric device configuration with VNF-PANF electrodes in 3 M KCl are tabulated in Table 4-3. VNF-VNF configuration exhibited a slightly lower ESR (1.82 Ω) compared to PANF-PANF (2.31 Ω) and PANF-VNF (2.65 Ω), probably due to the porous fiberous structure easing the flow of ions.

In the middle to low frequency region, both symmetrical and asymmetrical configurations showed high Warburg impedance values resulting from semi-infinite diffusion resistance of ions in the PANF and VNF electrode. Apparently, PANF-VNF exhibited a larger double layer capacitance (C_{dl}), probably resulting from the synergic effect.

Table 4-3: Components of the equivalent circuit fitted for the Nyquist plots of all symmetrical and asymmetrical device configurations depicted in Figure 4.44.

Configuration	$R_b(\Omega)$	$C_{dl}(mF\ cm^{-2})$	$R_{ct}(\Omega)$	$C_p(mF\ cm^{-2})$	$R_w(\Omega)$
VNF-VNF	1.82	14.65	0.51	7.78	15.21
PANF-PANF	2.31	16.34	19.17	0.06	16.42
VNF-PANF	2.65	21.76	21.37	20.56	23.53

The electrolyte resistance of the electrodes is small, indicating that the electrochemical properties of bulk electrolytes remain relatively stable. Both greater charge transfer resistance R_{ct} and higher pseudocapacitance C_p are obtained for the asymmetrical configuration. This indicates a greater amount of faradic current, a result of more charge transfer reactions taking place, analogous to the results revealed from CV and GCD measurements.

4.1.6 Contributions of Surface and Inner Charge Storage Capacity

To better understand the charge storage mechanism for the different nanofibers electrode in aqueous system, the measured current is segregated into two components. (1) capacitive contribution from fast electrical double layer and (2) diffusional controlled pseudocapacitance from charge transfer redox reaction. Based on the work of Trasatti et al. [151, 152], it is able to use the dependence of current on voltammetric scan rate to quantitatively determine the capacitive contribution. Accordingly, the voltammetric charge (q) of the electrode materials can be categorized into two parts, namely, surface capacitive charge (q_s) and diffusional controlled charge (q_d). Such can be described by the following equation,

$$q_T = q_s + q_d \tag{4.4}$$

Where q_d is the diffusional controlled charge storage component, q_T is the total charge storage capacity, and q_s is the surface charge component.

Surface capacitive charge having a faster kinetics can be correlated with double layer capacitance, while diffusional controlled charge depends mainly on the slower pseudocapacitance. Assuming semi-infinite linear diffusion process and within a reasonable range of scan rates, q_s can be derived from the plot of charge density against the inverse square root of potential scan rate (υ) and extrapolating υ to ∞ as given by the following equation,

$$q = q_s + kv^{-0.5} \tag{4.5}$$

Where q is the charge stored, q_s is the surface charge component, k is an arbitrary constant, υ is the scan rate.

On the other hand, if ions have ample time for diffusion to the inner and less accessible sites, via a very slow scan rate, theoretical maximum total charge storage (q_T) can be derived by using appropriate function of υ. Thus q_T can be extracted from plotting inverse charge storage with square root of scan rate according to

$$\frac{1}{q} = \frac{1}{q_T} + kv^{0.5} \tag{4.6}$$

Where q is the charge stored, q_T is the total charge storage capacity, k is an arbitrary constant, υ is the scan rate.

Figure 4.45 shows the extrapolated curves for FNF, VNF and PANF, respectively. The deviation from linearity of such plot at high scan rate can be ascribed to the polarization effects that are omitted in the above equation [151, 152]. The extrapolated values are extracted and used in subsequent analysis.

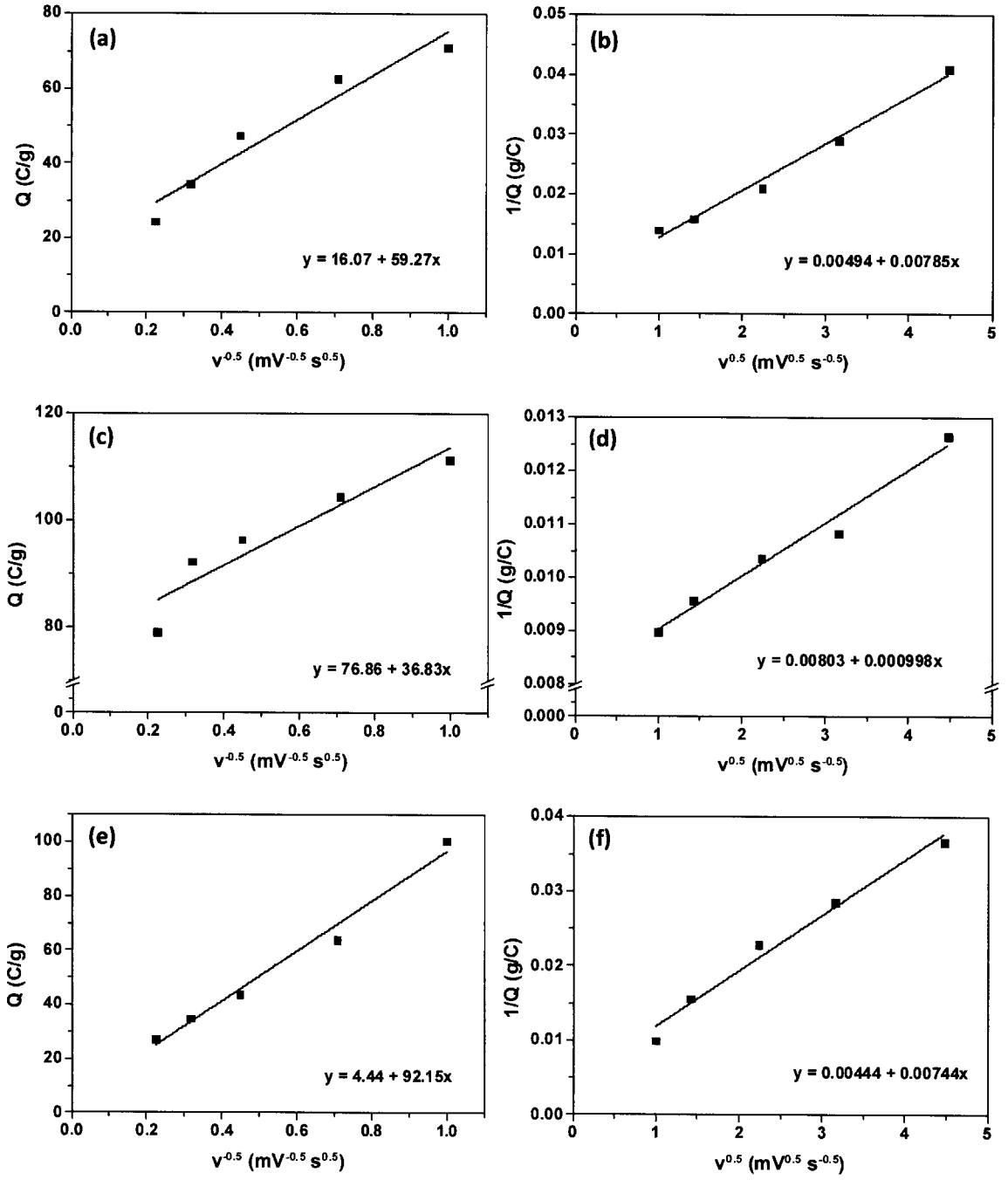

Figure 4.45: Variation of charge density (q) with respect to scan rates (ν) : (a) Extrapolation of ν to ∞ (the y-intercept of the q vs. $\nu^{-0.5}$ plot) giving the outer charge for FNF electrodes. (b) Extrapolation of ν to 0 (the y-intercept of the 1/q vs. $\nu^{0.5}$ plot) giving the maximum volummetric charge for FNF electrodes. Extrapolation as mentioned in (a) for (c) PANF (e) VNF. Extrapolation as mentioned in (b) for (d) PANF (f) VNF.

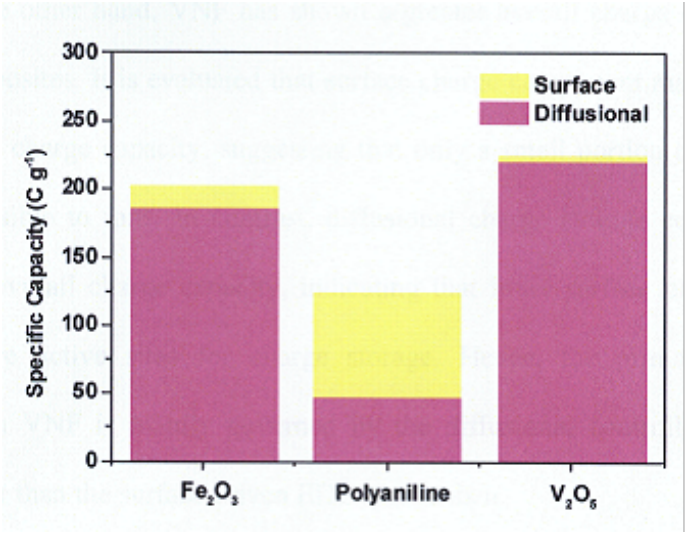

Figure 4.46: Categorization of contribution from surface capacitive and diffusional controlled capacity of various nanofibers.

Figure 4.46 illustrates the derived surface capacitive and diffusional controlled components. It clearly shows that diffusional controlled charge storage play a significant role in the total capacity of the nanocomposite electrode. It is noted that PANF has the largest surface capacitive charge storage contribution while VNF reaped in the lowest value. This is consistent with the observation in FESEM and BET characterization which shows the highest surface area for PANF which facilities the transport of electrolyte ions and enhances the electrochemical utilization of PANF surface sites. FNF has approximately 8% charge contribution coming from the surface charge component, showing better surface charge storage capability than VNF also in agreement with the observation in BET characterization. Additionally, FNF has shown a superior overall charge storage capability than PANF which can be ascribed to the presence of multiple oxidation states presented in iron.

On the other hand, VNF has shown a greater overall charge capacity among all the nanocomposites. It is evaluated that surface charge component make up of about 2% of the overall charge capacity, suggesting that only a small portion of the VNF surface sites is accessible to ions. In contrast, diffusional charge storage component make up most of the overall charge capacity, indicating that inner surface or bulk of the VNF provides more active sites for charge storage. Hence, the primary charge storage mechanism in VNF is mainly governed by the diffusional controlled electrochemical reaction rather than the surface driven EDL mechanism.

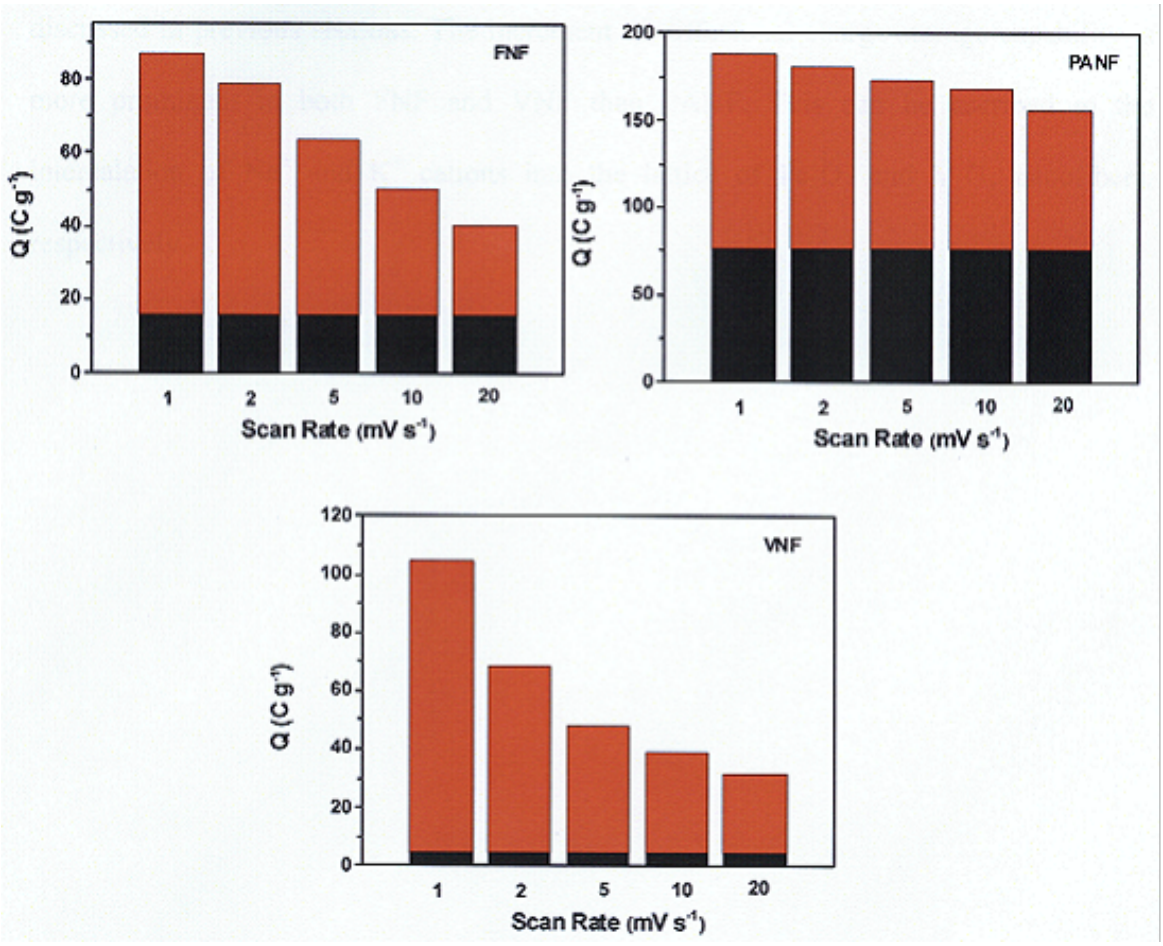

Figure 4.47: Dependence of surface charge and diffusional charge storage on scan rate. Surface charge storage capacity (black), diffusional charge storage capacity (red).

The relationship of charge storage with scan rate is also studied. Figure 4.46 depicts the plot of charge storage of various nanofibers with scan rate. It is clear that surface capacitive process becomes more accountable with higher scan rate. This is because when the nanofibers are subjected to higher scan rate, the electrolytes' ions have less time to diffuse to the active sites which results in fewer uptakes of active sites for pseudocapacitive process. This agrees well with the cyclicvoltammogram results

discussed in previous sections. The increment of diffusional charge storage capability is more prominent in both FNF and VNF than PANF. This can be ascribed to the intercalation of Na^+ and K^+ cations into the lattice of Fe_2O_3 and V_2O_5 nanofibers, respectively.

Chapter 5 Conclusions

This thesis presents a study on the charge storage mechanism and pseudocapacitive behavior of transitional metal oxide nano-composites and application of such nanomaterials in supercapacitor device configuration. Also, an asymmetrical architecture of transition metal oxide and conducting polymer has been successfully employed to increase the working voltage which renders greater energy density storage capability.

Electrochemical behaviors of EDL nanomaterials such as CNT were investigated. Although they show great power density, challenge of enhancement of energy density still remains attributable to the limited accessible surface area. Tin oxides nanospheres were added to the CNT to enhance the capacitance, however, no substantial improvement was observed probably due to the high contact resistance between the SnO_2 and CNT. Another pseudocapacitive material, Fe_2O_3 has been demonstrated to be a promising electrode material for application in supercapacitor. Electrospinning technique was employed to weave interconnected network of nanofibers. The sintering temperature and ramping rate have been optimized to 500 °C and 5 °C /min to obtain α-Fe_2O_3 nanofibers as well as maintaining its fibrous morphology. Such nanostructured fibrous morphology can heighten the specific capacitance by increasing the accessible surface area and facilitates ions transportation. However, the specific capacitance remains mediocre which is attributable to the high resistivity of α-Fe_2O_3. To improve the specific capacitance, carbon black was added as conducting agent to facilitate electronic pathways for current

passage. The specific capacitance was enhanced substantially with the introduction of carbon black. Furthermore, the pseudocapacitive contribution from FNF was significantly increased as more charges can be harvested from the redox-active sites. The observations also revealed that specific capacitance is comprised of (i) non-faradic double layer capacitance and (ii) faradic pseudocapacitance. The former is primarily governed by the accessible conducting surface area whereas the later is greatly influenced by the pseudocapacitive properties of redox materials.

Extending the methodology, other transitional metal oxides such as V_2O_5 nanofibers was also synthesized. It exhibited good pseudocapacitive behavior in aqueous KCl solution and shows promise as a good electrode material for supercapacitor application.

To achieve higher energy density, the working voltage needs to be further extended. As such, the asymmetrical device configuration was conceptualized. To implement such architecture, a common electrolyte which works well with both the positive and anode is required. Polyaniline, an electrode material which also exhibits pseudocapacitive behavior in aqueous KCl solution is roped in. Nanostructured polyaniline was also obtained and found to be a good positive electrode material. On the other hand, V_2O_5 nanofibers demonstrate better performance as as a negative electrode material. Hence, nanofibers of polyaniline and V_2O_5 were coupled and assembled into an asymmetrical supercapacitor device. The product was found capable of having a wider

working voltage of up to 2 V in aqueous solution. As such, a higher energy density is achieved.

Moreover, XPS analysis is performed to provide further insight into the charge storage mechanism of VNF and FNF suggesting the intercalation of K^+ and Na^+ ions into the oxide lattice of Fe_2O_3 and V_2O_5 lattices, respectively. It is therefore clear that intercalation of ions process rather than redox process contributes significantly to the charge storage mechanism of TMO nanofibers. Also, the surface double layer and diffusional controlled bulk storage ratio is also investigated.

In summary, the contributions of this thesis include investigating the application of α-Fe_2O_3 in a two electrode symmetrical device configuration, the effects of conducting agent on the pseudocapacitive performance, and the employment of asymmetrical device configuration to improve the energy density of the supercapacitor device. Performance enhancement of the devices was demonstrated with nanostructured materials. A thorough understanding of the contribution of nanomaterials towards charge storage and mechanism was demonstrated.

Chapter 6 Future Works

Stemming from the works made in this thesis, further studies are needed in several areas to corroborate as well as to extend current work. Some recommendations are as follow,

6.1 Enhancing Electrical Conductivity

While the ASC benefit from good energy, they carry a low power density rating. It may be good to replace electrodes with a composite which has highly accessible surface area of good conductivity and great pseudocapacitive behavior. To achieve such combination, a conducting pseudocapacitive material is needed. Although electrically conducting polymer is having both the qualities, their conductivity is still insufficient. More needs to be done to further enhance their electrical conductivity. Also, polymers often suffers from short cycle life, hence, efforts need to spend on minimizing degradation of polymer on cycling. Similarly, transitional metal oxides also suffer low electrical conductivity although they have exhibited high capacitance and are capable of greater charge storage. Therefore, more work is required to improve the electrical conductivity. Carbon coating is a good avenue to better electrical conductivity. Such coating can be achieved by hydrothermal method using a carbon source precursor like glucose. Co-electrospinning is also a feasible route to acquire carbon coating. By co-spinning metal oxide precursor with carbon source like polyacrylonitrile and later sinter

to obtain carbon-metal oxide interlinked network, a better connected network can be realized.

6.2 Investigation of Charge Transfer Mechanism via in-situ Route

Investigation of redox process in transitional metal oxides is critical to understanding of charge storage process. Most of the research done until now exercises ex-situ characterization such as XPS and XRD. Such routes are unable to better comprehend the transition process of charge storage and utilization. The electrode material may have undergone changes after being exposed to the environment. In-situ XPS, XRD and FTIR characterization could provide a good real time portrayal of the on-going process and changes. This enables a better understanding of the changes in valence states and/or ions intercalation/de-intercalation occurring in the electrode material.

List of Symbols and Abbreviations

EDL	Electrical Double Layer
SC	Supercapacitor
EC	Electrochemical capacitor
EDLC	Electrical Double Layer Capacitor
AC	Activated carbon
CNT	Carbon nanotubes
SWNT	Single-walled nanotubes
MWNT	Multi-walled nanotubes
NW	Nanowires
CB	Carbon black
PANI	Polyaniline
PEDOT	Poly (4-styrenesulfonate)
PSS	Poly (styrenesulfonate)
Ppy	Polypyrrole
PMeT	Poly (3-methylthiophene)

PVP	Polyvinylpyrrolidone
PVdF	poly-vinylidenefluoride
NMP	*N*-methylpyrrolidone
α-Fe_2O_3	Alpha iron (III) oxide or hematite
FNF	Iron (III) oxide nanofibers
VNF	Vanadium (IV) oxide nanofibers
AN	Acetonitrile
EC	Ethylene carbonate
DEC	Diethylene carbonate
DMC	Dimethyl carbonate
CV	Cyclic Voltammetry
GCD	Galvanostatic charge-discharge
EIS	Electrochemical Impedance Spectroscopy
FESEM	Field Emission Scanning Electron Microscopy
TEM	Transmission Electron Microscopy
XRD	X-ray Diffraction

BET	Brunauer, Emmett and Teller
BJH	Barrett, Joyner and Halenda
FTIR	Fourier Transform Infrared spectroscopy
TGA	Thermo gravimetric Analysis
C_T	Total capacitance
C_p or C_+	Capacitance of positive electrode
C_n or C_-	Negative electrode
V	Voltage
R_{ESR}	Equivalent Series Resistance
E	Energy
P	Power
C_D	Specific capacitance of the device
C_{dl}	Double layer capacitance
C_{ps}	Pseudocapacitance
Z	Magnitude of ionic charge
C	Concentration

C_0	Concentration of ions in bulk solution
q	Electronic charge
m_+	Mass of positive electrode
m_-	Mass of negative electrode
e	charge of an electron ($1.60217646 \times 10^{-19}$ C)
ΔE_+	Voltage of positive electrode
ΔE_-	Voltage of negative electrode
t	Time
k	Boltzmann constant ($1.3806503 \times 10^{-23}$ m^2 kg s^{-2} K^{-1})
T	Absolute temperature in Kelvin
φ_m	Potential at the metal surface
ε_0	Permittivity of free space (8.854×10^{-12} J^{-1} m^{-1})
ε_r	Dielectric constant of electrolyte
A	Surface area
d	Distance between parallel plates of charges
C_H	Capacitance contribution from the Helmholtz layer

C_G	Capacitance contribution from the diffuse layer

List of Publications

Journal Articles

1. **Wai Fatt Mak**, Grace Wee, Vanchiappan Aravindan, Nutan Gupta, Subodh G Mhaisalkar and Srinivasan Madhavi, "High-energy density asymmetric supercapacitor based on electrospun vanadium pentoxide and polyaniline nanofibers in aqueous electrolyte", J Electrochem. Soc. *2012 159(9): A1481-A1488.*

2. Grace Wee, **Wai Fatt Mak**, N.Ponthamachai, M.V.Reddy, B.V.R.Chowdari and Madhavi Srinivasan, Subodh Mhaisalkar, "Silver decorated carbon nanotubes based supercapacitors", J Electrochem. Soc *157(2) (2010) A179-A184.*

3. V.Aravindan, Yan Ling Cheah, **Wai Fatt Mak**, Grace Wee, B. V. R. Chowdari, and Srinivasan Madhavi, "Fabrication of High Energy-Density Hybrid Supercapacitors Using electrospun V_2O_5 Nanofibers with Self-Supported Carbon Nanotube Network", ChemPlusChem *(2012), 77, 1 – 6.*

4. Nutan Gupta Tingji Toh, Hong Ting Lee, **Wai Fatt Mak**, Subodh Mhaisalkar, Madhavi Srinivasan, "Paper like free-standing hybrid single-walled carbon nanotubes air electrodes for zinc-air batteries", J solid State Electrochemistry *16 (2012) pp 1585-1593.*

5. Lifei Xi, Phong D Tran, Sing Yang Chiam, Prince Saurabh Bassi, **Wai Fatt Mak**, Hemant Kumar Mulmudi, Sudip K Batabyal, James Barber and Joachim Say Chye Loo, Lydia Helena Wong, "Co_3O_4 -decorated hematite nanorods as an effective photoanode for solar water oxidation", Journal of physical chemistry C 116 (2012), *pp 13884–13889*

6. Lifei Xi , Prince Saurabh Bassi , Sing Yang Chiam , **Wai Fatt Mak** , Phong D. Tran , James Barber , Joachim Say Chye Loo and Lydia Helena Wong "Surface treatment of hematite photoanodes with zinc acetate for water oxidation", Nanoscale 4 (2012), *pp 4430-4433.*

Patents

1. **W.F. Mak**, W. Ting, N. Phonthammachai, M. Srinivasan, S.G. Mhaisalkar, F. Boey, "Electrode Materials for Metal-Air Batteries, Fuel Cells and Supercapacitors," US Provisional Application No.61/095,085 filed 8 September 2008 , PCT Application No. PCT/SG2009/000319 filed 7th September 2009.
2. G. Wee, **W.F. Mak**, Martti Kempgen, M Srinivasan, S.G. Mhaisalkar, F. Boey," Energy Charge Storage Device Using a Printable Polyelectrolyte as Electrolyte Material," PCT International Application No. PCT/SG2009/000236 filed 26th June 2009.
3. G. Wee, **W.F. Mak**, Teddy Salim, M. Srinivasan, S.G. Mhaisalkar, F. Boey "Integrated Electrode Architectures for Energy Generation and Storage," PCT International Application No. PCT/ SG2009/000288 filed on 20th August 2009.

Posters

1. **W.F. Mak**, Y. Sharma, Madhavi Srinivasan, Subodh Mhaisalkar "Electrospun Tenary Transition Metal Oxide for Supercapacitor Application" International Conference on Materials for Advanced Technologies (ICMAT), Singapore, 2011. (Best Poster Award)

References

[1] J. Schindall, The charge of the ultracapacitors, IEEE Spectrum, 44 (2007) 42-46.

[2] H.I. Becker, Low voltage electrolytic capacitor, in, The United States Patent and Trademark Office 1957.

[3] J. Miller, Fundamentals of electrochemical capacitor design and operation, The Electrochemical Society interface, 17 (2008) 31-32.

[4] B.E. Conway, Transition from Supercapacitor to Battery Behavior in Electrochemical Energy-Storage, Journal of the Electrochemical Society, 138 (1991) 1539-1548.

[5] Basic Research Needs for Electrical Energy Storage, in, vol. 2012, U.S. DOE Office of Science (SC), Washington, DC 2007.

[6] F. Béguin, E. Frąckowiak, Carbons for Electrochemical Energy Storage and Conversion Systems, CRC Press, 2010.

[7] J.H. Chen, W.Z. Li, D.Z. Wang, S.X. Yang, J.G. Wen, Z.F. Ren, Electrochemical characterization of carbon nanotubes as electrode in electrochemical double-layer capacitors, Carbon, 40 (2002) 1193-1197.

[8] T. Cottineau, M. Toupin, T. Delahaye, T. Brousse, D. Bélanger, Nanostructured transition metal oxides for aqueous hybrid electrochemical supercapacitors, Applied Physics A: Materials Science & Processing, 82 (2006) 599-606.

[9] J.H. Park, O.O. Park, Hybrid electrochemical capacitors based on polyaniline and activated carbon electrodes, Journal of Power Sources, 111 (2002) 185-190.

[10] A.J. Bard, L.R. Faulkner, Electrochemical methods: fundamentals and applications, Wiley New York, 1980.

[11] J.O.M. Bockris, A.K.N. Reddy, M.E. Gamboa-Aldeco, Modern Electrochemistry 2A: Fundamentals of Electrodics, 2nd Edition ed., Springer, 2000.

[12] B.E. Conway, V. Birss, J. Wojtowicz, The role and utilization of pseudocapacitance for energy storage by supercapacitors, Journal of Power Sources, 66 (1997) 1-14.

[13] B.E. Conway, W.G. Pell, Double-layer and pseudocapacitance types of electrochemical capacitors and their applications to the development of hybrid devices, Journal of Solid State Electrochemistry, 7 (2003) 637-644.

[14] G.A. Snook, P. Kao, A.S. Best, Conducting-polymer-based supercapacitor devices and electrodes, Journal of Power Sources, 196 (2011) 1-12.

[15] M. Mastragostino, C. Arbizzani, F. Soavi, Polymer-based supercapacitors, Journal of Power Sources, 97–98 (2001) 812-815.

[16] K.S. Ryu, Y.-G. Lee, Y.-S. Hong, Y.J. Park, X. Wu, K.M. Kim, M.G. Kang, N.-G. Park, S.H. Chang, Poly(ethylenedioxythiophene) (PEDOT) as polymer electrode in redox supercapacitor, Electrochimica Acta, 50 (2004) 843-847.

[17] Y.M. Vol'fkovich, T.M. Serdyuk, Electrochemical Capacitors, Russian Journal of Electrochemistry, 38 (2002) 935-959.

[18] M. Mastragostino, C. Arbizzani, L. Meneghello, R. Paraventi, Electronically conducting polymers and activated carbon: Electrode materials in supercapacitor technology, Advanced Materials, 8 (1996) 331-334.

[19] S.A. Hashmi, H.M. Upadhyaya, Polypyrrole and poly(3-methyl thiophene)-based solid state redox supercapacitors using ion conducting polymer electrolyte, Solid State Ionics, 152–153 (2002) 883-889.

[20] D. Villers, D. Jobin, C. Soucy, D. Cossement, R. Chahine, L. Breau, D. Belanger, The Influence of the Range of Electroactivity and Capacitance of Conducting Polymers on the Performance of Carbon Conducting Polymer Hybrid Supercapacitor, Journal of The Electrochemical Society, 150 (2003) A747-A752.

[21] K.S. Ryu, K.M. Kim, Y.J. Park, N.-G. Park, M.G. Kang, S.H. Chang, Redox supercapacitor using polyaniline doped with Li salt as electrode, Solid State Ionics, 152–153 (2002) 861-866.

[22] G.A. Snook, G.Z. Chen, The measurement of specific capacitances of conducting polymers using the quartz crystal microbalance, Journal of Electroanalytical Chemistry, 612 (2008) 140-146.

[23] E. Frackowiak, V. Khomenko, K. Jurewicz, K. Lota, F. Béguin, Supercapacitors based on conducting polymers/nanotubes composites, Journal of Power Sources, 153 (2006) 413-418.

[24] E. Frackowiak, F. Beguin, Carbon materials for the electrochemical storage of energy in capacitors, Carbon, 39 (2001) 937-950.

[25] A.G. Pandolfo, A.F. Hollenkamp, Carbon properties and their role in supercapacitors, Journal of Power Sources, 157 (2006) 11-27.

[26] R. Saito, G. Dresselhaus, M.S. Dresselhaus, Electronic structure of double-layer graphene tubules, Journal of Applied Physics, 73 (1993) 494-500.

[27] J.P. Issi, L. Langer, J. Heremans, C.H. Olk, Electronic properties of carbon nanotubes: Experimental results, Carbon, 33 (1995) 941-948.

[28] E. Frackowiak, K. Jurewicz, S. Delpeux, F. Béguin, Nanotubular materials for supercapacitors, Journal of Power Sources, 97–98 (2001) 822-825.

[29] E. Raymundo-Pinero, V. Khomenko, E. Frackowiak, F. Beguin, Performance of manganese oxide/CNTs composites as electrode materials for electrochemical capacitors, Journal of the Electrochemical Society, 152 (2005) A229-A235.

[30] C.M. Niu, E.K. Sichel, R. Hoch, D. Moy, H. Tennent, High power electrochemical capacitors based on carbon nanotube electrodes, Applied Physics Letters, 70 (1997) 1480-1482.

[31] C. Emmenegger, P. Mauron, A. Zuttel, C. Nutzenadel, A. Schneuwly, R. Gallay, L. Schlapbach, Carbon nanotube synthesized on metallic substrates, Applied Surface Science, 162 (2000) 452-456.

[32] V.L. Pushparaj, M.M. Shaijumon, A. Kumar, S. Murugesan, L. Ci, R. Vajtai, R.J. Linhardt, O. Nalamasu, P.M. Ajayan, Flexible energy storage devices based on nanocomposite paper, Proceedings of the National Academy of Sciences of the United States of America, 104 (2007) 13574-13577.

[33] Y. Wang, Z. Shi, Y. Huang, Y. Ma, C. Wang, M. Chen, Y. Chen, Supercapacitor Devices Based on Graphene Materials, The Journal of Physical Chemistry C, 113 (2009) 13103-13107.

[34] S. Stankovich, D.A. Dikin, G.H.B. Dommett, K.M. Kohlhaas, E.J. Zimney, E.A. Stach, R.D. Piner, S.T. Nguyen, R.S. Ruoff, Graphene-based composite materials, Nature, 442 (2006) 282-286.

[35] A.A. Balandin, S. Ghosh, W. Bao, I. Calizo, D. Teweldebrhan, F. Miao, C.N. Lau, Superior Thermal Conductivity of Single-Layer Graphene, Nano Letters, 8 (2008) 902-907.

[36] S. Park, R.S. Ruoff, Chemical methods for the production of graphenes, Nat Nano, 4 (2009) 217-224.

[37] Y.-k. Zhou, B.-l. He, W.-j. Zhou, J. Huang, X.-h. Li, B. Wu, H.-l. Li, Electrochemical capacitance of well-coated single-walled carbon nanotube with polyaniline composites, Electrochimica Acta, 49 (2004) 257-262.

[38] L.-Z. Fan, J. Maier, High-performance polypyrrole electrode materials for redox supercapacitors, Electrochemistry Communications, 8 (2006) 937-940.

[39] B.E. Conway, Electrochemical supercapacitors: scientific fundamentals and technological applications, Springer, 1999.

[40] V. Khomenko, E. Frackowiak, F. Béguin, Determination of the specific capacitance of conducting polymer/nanotubes composite electrodes using different cell configurations, Electrochimica Acta, 50 (2005) 2499-2506.

[41] J. Wang, Y. Xu, X. Chen, X. Du, Electrochemical supercapacitor electrode material based on poly(3,4-ethylenedioxythiophene)/polypyrrole composite, Journal of Power Sources, 163 (2007) 1120-1125.

[42] H. An, Y. Wang, X. Wang, L. Zheng, X. Wang, L. Yi, L. Bai, X. Zhang, Polypyrrole/carbon aerogel composite materials for supercapacitor, Journal of Power Sources, 195 (2010) 6964-6969.

[43] Y. Fang, J. Liu, D.J. Yu, J.P. Wicksted, K. Kalkan, C.O. Topal, B.N. Flanders, J. Wu, J. Li, Self-supported supercapacitor membranes: Polypyrrole-coated carbon nanotube networks enabled by pulsed electrodeposition, Journal of Power Sources, 195 (2010) 674-679.

[44] J. Zang, S.-J. Bao, C.M. Li, H. Bian, X. Cui, Q. Bao, C.Q. Sun, J. Guo, K. Lian, Well-Aligned Cone-Shaped Nanostructure of Polypyrrole/RuO2 and Its Electrochemical Supercapacitor, The Journal of Physical Chemistry C, 112 (2008) 14843-14847.

[45] R.K. Sharma, A.C. Rastogi, S.B. Desu, Manganese oxide embedded polypyrrole nanocomposites for electrochemical supercapacitor, Electrochimica Acta, 53 (2008) 7690-7695.

[46] K. Zhang, L.L. Zhang, X.S. Zhao, J. Wu, Graphene/Polyaniline Nanofiber Composites as Supercapacitor Electrodes, Chemistry of Materials, 22 (2010) 1392-1401.

[47] H. Zhang, G. Cao, Z. Wang, Y. Yang, Z. Shi, Z. Gu, Tube-covering-tube nanostructured polyaniline/carbon nanotube array composite electrode with high capacitance and superior rate performance as well as good cycling stability, Electrochemistry Communications, 10 (2008) 1056-1059.

[48] L.-M. Huang, T.-C. Wen, A. Gopalan, Electrochemical and spectroelectrochemical monitoring of supercapacitance and electrochromic properties of hydrous ruthenium oxide

embedded poly(3,4-ethylenedioxythiophene)–poly(styrene sulfonic acid) composite, Electrochimica Acta, 51 (2006) 3469-3476.

[49] K. Lota, V. Khomenko, E. Frackowiak, Capacitance properties of poly(3,4-ethylenedioxythiophene)/carbon nanotubes composites, Journal of Physics and Chemistry of Solids, 65 (2004) 295-301.

[50] S. Biswas, L.T. Drzal, Multilayered Nanoarchitecture of Graphene Nanosheets and Polypyrrole Nanowires for High Performance Supercapacitor Electrodes, Chemistry of Materials, 22 (2010) 5667-5671.

[51] W.D. Ryden, A.W. Lawson, Electrical Transport Properties of Iro2 and Ruo2, Physical Review B, 1 (1970) 1494-&.

[52] J.P. Zheng, P.J. Cygan, T.R. Jow, Hydrous ruthenium oxide as an electrode material for electrochemical capacitors, Journal of the Electrochemical Society, 142 (1995) 2699-2703.

[53] I.-H. Kim, K.-B. Kim, Electrochemical Characterization of Hydrous Ruthenium Oxide Thin-Film Electrodes for Electrochemical Capacitor Applications, Journal of The Electrochemical Society, 153 (2006) A383-A389.

[54] T.R. Jow, J.P. Zheng, Electrochemical capacitors using hydrous ruthenium oxide and hydrogen inserted ruthenium oxide, Journal of the Electrochemical Society, 145 (1998) 49-52.

[55] Y.-F. Ke, D.-S. Tsai, Y.-S. Huang, Electrochemical capacitors of RuO_2 nanophase grown on $LiNbO_3$(100) and sapphire(0001) substrates, Journal of Materials Chemistry, 15 (2005) 2122-2127.

[56] W. Sugimoto, K. Yokoshima, Y. Murakami, Y. Takasu, Charge storage mechanism of nanostructured anhydrous and hydrous ruthenium-based oxides, Electrochimica Acta, 52 (2006) 1742-1748.

[57] Y. Lin, N. Zhao, W. Nie, X. Ji, Synthesis of Ruthenium Dioxide Nanoparticles by a Two-Phase Route and Their Electrochemical Properties, The Journal of Physical Chemistry C, 112 (2008) 16219-16224.

[58] C.-C. Hu, K.-H. Chang, M.-C. Lin, Y.-T. Wu, Design and Tailoring of the Nanotubular Arrayed Architecture of Hydrous RuO_2 for Next Generation Supercapacitors, Nano Letters, 6 (2006) 2690-2695.

[59] Y.R. Ahn, C.R. Park, S.M. Jo, D.Y. Kim, Enhanced charge-discharge characteristics of RuO_2 supercapacitors on heat-treated TiO_2 nanorods, Applied Physics Letters, 90 (2007) 122106-122103.

[60] J.-i. Hong, I.-H. Yeo, W.-k. Paik, Conducting Polymer with Metal Oxide for Electrochemical Capacitor: Poly(3,4-ethylenedioxythiophene) RuO_x Electrode, Journal of The Electrochemical Society, 148 (2001) A156-A163.

[61] H.Y. Lee, J.B. Goodenough, Supercapacitor Behavior with KCl Electrolyte, Journal of Solid State Chemistry, 144 (1999) 220-223.

[62] B. Messaoudi, S. Joiret, M. Keddam, H. Takenouti, Anodic behaviour of manganese in alkaline medium, Electrochimica Acta, 46 (2001) 2487-2498.

[63] M. Toupin, T. Brousse, D. Bélanger, Charge Storage Mechanism of MnO_2 Electrode Used in Aqueous Electrochemical Capacitor, Chemistry of Materials, 16 (2004) 3184-3190.

[64] M. Toupin, T. Brousse, D. Belanger, Influence of microstucture on the charge storage properties of chemically synthesized manganese dioxide, Chemistry of Materials, 14 (2002) 3946-3952.

[65] A.P. Malloy, S.W. Donne, Characterization of solid electrode materials using chronoamperometry: A study of the alkaline γ-MnO_2 electrode, Journal of Power Sources, 179 (2008) 371-380.

[66] S.C. Pang, M.A. Anderson, T.W. Chapman, Novel electrode materials for thin-film ultracapacitors: comparison of electrochemical properties of sol-gel-derived and electrodeposited manganese dioxide, Journal of The Electrochemical Society, 147 (2000) 444-450.

[67] P. Simon, Y. Gogotsi, Materials for electrochemical capacitors, Nat Mater, 7 (2008) 845-854.

[68] T. Brousse, P.-L. Taberna, O. Crosnier, R. Dugas, P. Guillemet, Y. Scudeller, Y. Zhou, F. Favier, D. Bélanger, P. Simon, Long-term cycling behavior of asymmetric activated carbon/MnO_2 aqueous electrochemical supercapacitor, Journal of Power Sources, 173 (2007) 633-641.

[69] K. Rajendra Prasad, N. Miura, Electrochemical synthesis and characterization of nanostructured tin oxide for electrochemical redox supercapacitors, Electrochemistry Communications, 6 (2004) 849-852.

[70] M. Wu, L. Zhang, D. Wang, C. Xiao, S. Zhang, Cathodic deposition and characterization of tin oxide coatings on graphite for electrochemical supercapacitors, Journal of Power Sources, 175 (2008) 669-674.

[71] H.Y. Lee, J.B. Goodenough, Ideal Supercapacitor Behavior of Amorphous $V_2O_5 \cdot nH_2O$ in Potassium Chloride (KCl) Aqueous Solution, Journal of Solid State Chemistry, 148 (1999) 81-84.

[72] T. Kudo, Y. Ikeda, T. Watanabe, M. Hibino, M. Miyayama, H. Abe, K. Kajita, Amorphous V2O5/carbon composites as electrochemical supercapacitor electrodes, Solid State Ionics, 152–153 (2002) 833-841.

[73] I.H. Kim, J.H. Kim, B.W. Cho, Y.H. Lee, K.B. Kim, Synthesis and electrochemical characterization of vanadium oxide on carbon nanotube film substrate for pseudocapacitor applications, Journal of the Electrochemical Society, 153 (2006) A989-A996.

[74] S. Boukhalfa, K. Evanoff, G. Yushin, Atomic layer deposition of vanadium oxide on carbon nanotubes for high-power supercapacitor electrodes, Energy & Environmental Science, 5 (2012) 6872-6879.

[75] T. Brousse, D. Bélanger, A Hybrid FeO-MnO Capacitor in Mild Aqueous Electrolyte, Electrochemical and solid-state letters, 6 (2003) A244-A248.

[76] N.-L. Wu, S.-Y. Wang, C.-Y. Han, D.-S. Wu, L.-R. Shiue, Electrochemical capacitor of magnetite in aqueous electrolytes, Journal of Power Sources, 113 (2003) 173-178.

[77] J. Chen, K. Huang, S. Liu, Hydrothermal preparation of octadecahedron Fe_3O_4 thin film for use in an electrochemical supercapacitor, Electrochimica Acta, 55 (2009) 1-5.

[78] M.S. Wu, R.H. Lee, J.J. Jow, W.D. Yang, C.Y. Hsieh, B.J. Weng, Nanostructured Iron Oxide Films Prepared by Electrochemical Method for Electrochemical Capacitors, Electrochemical and Solid State Letters, 12 (2009) A1-A4.

[79] S.Y. Wang, K.C. Ho, S.L. Kuo, N.L. Wu, Investigation on Capacitance Mechanisms of FeO Electrochemical Capacitors, Journal of the Electrochemical Society, 153 (2006) A75-A80.

[80] X. Zhao, C. Johnston, P.S. Grant, A novel hybrid supercapacitor with a carbon nanotube cathode and an iron oxide/carbon nanotube composite anode, Journal of Materials Chemistry, 19 (2009) 8755-8760.

[81] B.J. Li, H.Q. Cao, J. Shao, M.Z. Qu, J.H. Warner, Superparamagnetic Fe_3O_4 nanocrystals@graphene composites for energy storage devices, Journal of Materials Chemistry, 21 (2011) 5069-5075.

[82] X. Du, C. Wang, M. Chen, Y. Jiao, J. Wang, Electrochemical Performances of Nanoparticle Fe_3O_4/Activated Carbon Supercapacitor Using KOH Electrolyte Solution, The Journal of Physical Chemistry C, 113 (2009) 2643-2646.

[83] P.M. Kulal, D.P. Dubal, C.D. Lokhande, V.J. Fulari, Chemical synthesis of Fe_2O_3 thin films for supercapacitor application, Journal of Alloys and Compounds, 509 (2011) 2567-2571.

[84] R.K. Selvan, I. Perelshtein, N. Perkas, A. Gedanken, Synthesis of Hexagonal-Shaped SnO_2 Nanocrystals and SnO_2@C Nanocomposites for Electrochemical Redox Supercapacitors, The Journal of Physical Chemistry C, 112 (2008) 1825-1830.

[85] L. Cui, J. Li, X.-G. Zhang, Preparation and properties of Co_3O_4 nanorods as supercapacitor material, Journal of Applied Electrochemistry, 39 (2009) 1871-1876.

[86] B. Ding, M. Wang, J. Yu, G. Sun, Gas Sensors Based on Electrospun Nanofibers, Sensors, 9 (2009) 1609-1624.

[87] R. Chen, S. Yu, R. Sun, Y. Zhao, Nanograins-Grafted Nanorods of MoO_2/Carbon Composite for Supercapacitor Application

THIRD INTERNATIONAL CONFERENCE ON SMART MATERIALS AND NANOTECHNOLOGY IN ENGINEERING, Proceedings of SPIE--the international society for optical engineering, 8409 (2012).

[88] P. Lin, Q. She, B. Hong, X. Liu, Y. Shi, Z. Shi, M. Zheng, Q. Dong, The Nickel Oxide/CNT Composites with High Capacitance for Supercapacitor, Journal of The Electrochemical Society, 157 (2010) A818-A823.

[89] Y.M. Chen, J.H. Cai, Y.S. Huang, K.Y. Lee, D.S. Tsai, Preparation and characterization of iridium dioxide-carbon nanotube nanocomposites for supercapacitors, Nanotechnology, 22 (2011).

[90] A.L.M. Reddy, S. Ramaprabhu, Nanocrystalline metal oxides dispersed multiwalled carbon nanotubes as supercapacitor electrodes, Journal of Physical Chemistry C, 111 (2007) 7727-7734.

[91] V. Khomenko, E. Raymundo-Piñero, F. Béguin, Optimisation of an asymmetric manganese oxide/activated carbon capacitor working at 2V in aqueous medium, Journal of Power Sources, 153 (2006) 183-190.

[92] G. Wee, H.Z. Soh, Y.L. Cheah, S.G. Mhaisalkar, M. Srinivasan, Synthesis and electrochemical properties of electrospun V_2O_5 nanofibers as supercapacitor electrodes, Journal of Materials Chemistry, 20 (2010) 6720-6725.

[93] A. Yuan, Q. Zhang, A novel hybrid manganese dioxide/activated carbon supercapacitor using lithium hydroxide electrolyte, Electrochemistry Communications, 8 (2006) 1173-1178.

[94] T. Brousse, M. Toupin, D. Belanger, A Hybrid Activated Carbon-Manganese Dioxide Capacitor using a Mild Aqueous Electrolyte, Journal of The Electrochemical Society, 151 (2004) A614-A622.

[95] Q. Qu, P. Zhang, B. Wang, Y. Chen, S. Tian, Y. Wu, R. Holze, Electrochemical Performance of MnO_2 Nanorods in Neutral Aqueous Electrolytes as a Cathode for Asymmetric Supercapacitors, The Journal of Physical Chemistry C, 113 (2009) 14020-14027.

[96] M.S. Hong, S.H. Lee, S.W. Kim, Use of KCl Aqueous Electrolyte for 2 V Manganese Oxide/Activated Carbon Hybrid Capacitor, Electrochemical and Solid-State Letters, 5 (2002) A227-A230.

[97] V. Khomenko, E. Raymundo-Piñero, E. Frackowiak, F. Béguin, High-voltage asymmetric supercapacitors operating in aqueous electrolyte, Applied Physics A: Materials Science & Processing, 82 (2006) 567-573.

[98] Z. Chen, Y. Qin, D. Weng, Q. Xiao, Y. Peng, X. Wang, H. Li, F. Wei, Y. Lu, Design and Synthesis of Hierarchical Nanowire Composites for Electrochemical Energy Storage, Advanced Functional Materials, 19 (2009) 3420-3426.

[99] K.C. Ng, S. Zhang, C. Peng, G.Z. Chen, Individual and Bipolarly Stacked Asymmetrical Aqueous Supercapacitors of CNTs/SnO_2 and CNTs/MnO_2] Nanocomposites, Journal of The Electrochemical Society, 156 (2009) A846-A853.

[100] Y.-g. Wang, Y.-y. Xia, Hybrid Aqueous Energy Storage Cells Using Activated Carbon and Lithium-Intercalated Compounds, Journal of The Electrochemical Society, 153 (2006) A450-A454.

[101] Q.T. Qu, Y. Shi, L.L. Li, W.L. Guo, Y.P. Wu, H.P. Zhang, S.Y. Guan, R. Holze, V2O5·0.6H2O nanoribbons as cathode material for asymmetric supercapacitor in K_2SO_4 solution, Electrochemistry Communications, 11 (2009) 1325-1328.

[102] D.-W. Wang, F. Li, H.-M. Cheng, Hierarchical porous nickel oxide and carbon as electrode materials for asymmetric supercapacitor, Journal of Power Sources, 185 (2008) 1563-1568.

[103] Y.-g. Wang, L. Yu, Y.-y. Xia, Electrochemical Capacitance Performance of Hybrid Supercapacitors Based on $Ni(OH)_2$/Carbon Nanotube Composites and Activated Carbon, Journal of The Electrochemical Society, 153 (2006) A743-A748.

[104] Q. Wang, Z.H. Wen, J.H. Li, A Hybrid Supercapacitor Fabricated with a Carbon Nanotube Cathode and a TiO_2–B Nanowire Anode, Advanced Functional Materials, 16 (2006) 2141-2146.

[105] T. Brousse, R. Marchand, P.-L. Taberna, P. Simon, TiO2 (B)/activated carbon non-aqueous hybrid system for energy storage, Journal of Power Sources, 158 (2006) 571-577.

[106] Y.G. Wang, Z.D. Wang, Y.Y. Xia, An asymmetric supercapacitor using RuO_2/TiO_2 nanotube composite and activated carbon electrodes, Electrochimica acta, 50 (2005) 5641-5646.

[107] X.W. Lou, D. Deng, J.Y. Lee, L.A. Archer, Preparation of SnO2/Carbon Composite Hollow Spheres and Their Lithium Storage Properties, Chemistry of Materials, 20 (2008) 6562-6566.

[108] J.X. Huang, R.B. Kaner, Nanofiber formation in the chemical polymerization of aniline: A mechanistic study, Angew Chem Int Edit, 43 (2004) 5817-5821.

[109] Y. Li, H. Liao, Y. Qian, Hydrothermal Synthesis of Ultrafine α-Fe2O3 and Fe3O4 Powders, Materials Research Bulletin, 33 (1998) 841-844.

[110] W. Zheng, Z. Li, H. Zhang, W. Wang, Y. Wang, C. Wang, Electrospinning route for α-Fe2O3 ceramic nanofibers and their gas sensing properties, Materials Research Bulletin, 44 (2009) 1432-1436.

[111] Y. Cheng, B. Zou, C. Wang, Y. Liu, X. Fan, L. Zhu, Y. Wang, H. Ma, X. Cao, Formation mechanism of Fe2O3 hollow fibers by direct annealing of the electrospun composite fibers and their magnetic, electrochemical properties, CrystEngComm, 13 (2011) 2863-2870.

[112] S.K. Apte, S.D. Naik, R.S. Sonawane, B.B. Kale, J.O. Baeg, Synthesis of nanosize-necked structure α- and γ-Fe 2O3 and its photocatalytic activity, Journal of the American Ceramic Society, 90 (2007) 412-414.

[113] J. Lian, X. Duan, J. Ma, P. Peng, T. Kim, W. Zheng, Hematite (α-Fe2O3) with Various Morphologies: Ionic Liquid-Assisted Synthesis, Formation Mechanism, and Properties, ACS Nano, 3 (2009) 3749-3761.

[114] W. Wu, X. Xiao, S. Zhang, J. Zhou, L. Fan, F. Ren, C. Jiang, Large-Scale and Controlled Synthesis of Iron Oxide Magnetic Short Nanotubes: Shape Evolution, Growth Mechanism, and Magnetic Properties, The Journal of Physical Chemistry C, 114 (2010) 16092-16103.

[115] J. Kielland, Individual Activity Coefficients of Ions in Aqueous Solutions, Journal of the American Chemical Society, 59 (1937) 1675-1678.

[116] R. Shannon, Revised effective ionic radii and systematic studies of interatomic distances in halides and chalcogenides, Acta Crystallographica Section A, 32 (1976) 751-767.

[117] D.D. Hawn, B.M. DeKoven, Deconvolution as a correction for photoelectron inelastic energy losses in the core level XPS spectra of iron oxides, Surface and Interface Analysis, 10 (1987) 63-74.

[118] M. Muhler, R. Schlögl, G. Ertl, The nature of the iron oxide-based catalyst for dehydrogenation of ethylbenzene to styrene 2. Surface chemistry of the active phase, Journal of Catalysis, 138 (1992) 413-444.

[119] T. Yamashita, P. Hayes, Analysis of XPS spectra of Fe2+ and Fe3+ ions in oxide materials, Applied Surface Science, 254 (2008) 2441-2449.

[120] C.-T. Hsieh, Y.-W. Chou, W.-Y. Chen, Synthesis and electrochemical characterization of carbon nanotubes decorated with nickel nanoparticles for use as an electrochemical capacitor, Journal of Solid State Electrochemistry, 12 (2008) 663-669.

[121] D. Choi, G.E. Blomgren, P.N. Kumta, Fast and Reversible Surface Redox Reaction in Nanocrystalline Vanadium Nitride Supercapacitors, Advanced Materials, 18 (2006) 1178-1182.

[122] K.S.W. Sing, D.H. Everett, R.A.W. Haul, L. Moscou, R.A. Pierotti, J. Rouquerol, T. Siemieniewska, REPORTING PHYSISORPTION DATA FOR GAS SOLID SYSTEMS WITH SPECIAL REFERENCE TO THE DETERMINATION OF SURFACE-AREA AND POROSITY (RECOMMENDATIONS 1984), Pure and Applied Chemistry, 57 (1985) 603-619.

[123] S. Brunauer, P.H. Emmett, E. Teller, Adsorption of Gases in Multimolecular Layers, Journal of the American Chemical Society, 60 (1938) 309-319.

[124] Q.X. Wu, Yuxi; Yao, Zhiyi; Liu, Anran; Shi, Gaoquan, Supercapacitors Based on Flexible Graphene/Polyaniline Nanofiber Composite Films, ACS nano, 4 (2010) 1963-1970.

[125] E.P. Barrett, L.G. Joyner, P.P. Halenda, The Determination of Pore Volume and Area Distributions in Porous Substances. I. Computations from Nitrogen Isotherms, Journal of the American Chemical Society, 73 (1951) 373-380.

[126] J. Rouquerol, D. Avnir, C.W. Fairbridge, D.H. Everett, J.M. Haynes, N. Pernicone, J.D.F. Ramsay, K.S.W. Sing, K.K. Unger, Recommendations for the characterization of porous solids (Technical Report), Pure and Applied Chemistry, 66 (1994) 19.

[127] G. Silversmit, D. Depla, H. Poelman, G.B. Marin, R. De Gryse, Determination of the V2p XPS binding energies for different vanadium oxidation states (V5+ to V0+), Journal of Electron Spectroscopy and Related Phenomena, 135 (2004) 167-175.

[128] M. Mastragostino, C. Arbizzani, F. Soavi, Polymer-based supercapacitors, J Power Sources, 97-98 (2001) 812-815.

[129] H.R. Ghenaatian, M.F. Mousavi, S.H. Kazemi, M. Shamsipur, Electrochemical investigations of self-doped polyaniline nanofibers as a new electroactive material for high performance redox supercapacitor, Synthetic Met, 159 (2009) 1717-1722.

[130] S. Patra, N. Munichandraiah, Supercapacitor studies of electrochemically deposited PEDOT on stainless steel substrate, Journal of Applied Polymer Science, 106 (2007) 1160-1171.

[131] J. Huang, Syntheses and applications of conducting polymer polyaniline nanofibers, Pure and applied chemistry, 78 (2006) 15-28.

[132] K. Zhang, L.L. Zhang, X.S. Zhao, J.S. Wu, Graphene/Polyaniline Nanoriber Composites as Supercapacitor Electrodes, Chemistry of Materials, 22 (2010) 1392-1401.

[133] H. Li, J. Wang, Q. Chu, Z. Wang, F. Zhang, S. Wang, Theoretical and experimental specific capacitance of polyaniline in sulfuric acid, J Power Sources, 190 (2009) 578-586.

[134] H.Z. Mi, Xiaogang; Ye, Xiangguo; Yang, Sudong, Preparation and enhanced capacitance of core–shell polypyrrole/polyaniline composite electrode for supercapacitors, J Power Sources, 176 (2008) 403-409.

[135] T. Cottineau, M. Toupin, T. Delahaye, T. Brousse, D. Bélanger, Nanostructured transition metal oxides for aqueous hybrid electrochemical supercapacitors, Applied Physics A: Materials Science and Processing, 82 (2006) 599-606.

[136] V. Subramanian, S.C. Hall, P.H. Smith, B. Rambabu, Mesoporous anhydrous RuO2 as a supercapacitor electrode material, Solid State Ionics, 175 (2004) 511-515.

[137] K.-W. Nam, K.-B. Kim, A Study of the Preparation of NiO[sub x] Electrode via Electrochemical Route for Supercapacitor Applications and Their Charge Storage Mechanism, J Electrochem Soc, 149 (2002) A346-A354.

[138] L. Wang, X. Liu, X. Wang, X. Yang, L. Lu, Preparation and electrochemical properties of mesoporous Co3O4 crater-like microspheres as supercapacitor electrode materials, Current Applied Physics, 10 (2010) 1422-1426.

[139] W.-C. Fang, Synthesis and Electrochemical Characterization of Vanadium Oxide/Carbon Nanotube Composites for Supercapacitors, The Journal of Physical Chemistry C, 112 (2008) 11552-11555.

[140] H. Mi, X. Zhang, S. Yang, X. Ye, J. Luo, Polyaniline nanofibers as the electrode material for supercapacitors, Mater Chem Phys, 112 (2008) 127-131.

[141] Z.-S. Wu, W. Ren, D.-W. Wang, F. Li, B. Liu, H.-M. Cheng, High-Energy MnO2 Nanowire/Graphene and Graphene Asymmetric Electrochemical Capacitors, ACS nano, 4 (2010) 5835-5842.

[142] P.-C. Chen, G. Shen, Y. Shi, H. Chen, C. Zhou, Preparation and Characterization of Flexible Asymmetric Supercapacitors Based on Transition-Metal-Oxide Nanowire/Single-Walled Carbon Nanotube Hybrid Thin-Film Electrodes, ACS nano, 4 (2010) 4403-4411.

[143] Q.T. Qu, Y. Shi, S. Tian, Y.H. Chen, Y.P. Wu, R. Holze, A new cheap asymmetric aqueous supercapacitor: Activated carbon//NaMnO2, J Power Sources, 194 (2009) 1222-1225.

[144] C.J. Xu, H.D. Du, B.H. Li, F.Y. Kang, Y.Q. Zeng, Asymmetric Activated Carbon-Manganese Dioxide Capacitors in Mild Aqueous Electrolytes Containing Alkaline-Earth Cations, J Electrochem Soc, 156 (2009) A435-A441.

[145] V. Khomenko, E. Raymundo-Pinero, F. Beguin, Optimisation of an asymmetric manganese oxide/activated carbon capacitor working at 2 V in aqueous medium, J Power Sources, 153 (2006) 183-190.

[146] A. Laforgue, P. Simon, J.F. Fauvarque, M. Mastragostino, F. Soavi, J.F. Sarrau, P. Lailler, M. Conte, E. Rossi, S. Saguatti, Activated carbon/conducting polymer hybrid supercapacitors, J Electrochem Soc, 150 (2003) A645-A651.

[147] H.S. Nalwa, Handbook of Organic Conductive Molecules and Polymers, Volume 2, Conductive Polymers: Synthesis and Electrical Properties, Volume 2 ed., Wiley, 2012.

[148] J. Doshi, D.H. Reneker, Electrospinning process and applications of electrospun fibers, Journal of Electrostatics, 35 (1995) 151-160.

[149] Z.-M. Huang, Y.Z. Zhang, M. Kotaki, S. Ramakrishna, A review on polymer nanofibers by electrospinning and their applications in nanocomposites, Compos. Sci. Technol., 63 (2003) 2223-2253.

[150] J. Stejskal, R.G. Gilbert, Polyaniline. Preparation of a conducting polymer (IUPAC technical report), Pure and Applied Chemistry, 74 (2002) 857-867.

[151] S. Ardizzone, G. Fregonara, S. Trasatti, "Inner" and "outer" active surface of RuO2 electrodes, Electrochimica Acta, 35 (1990) 263-267.

[152] D. Baronetto, N. Krstajić, S. Trasatti, Reply to "note on a method to interrelate inner and outer electrode areas" by H. Vogt, Electrochimica Acta, 39 (1994) 2359-2362.